Confined Excitons and Biexcitonic Optical Gain in Spherical Perovskite Quantum Dots

Anja Barfüßer

Munich, 2025

Confined Excitons and Biexcitonic Optical Gain in Spherical Perovskite Quantum Dots

Dissertation

zur Erlangung des Doktorgrades der Naturwissenschaften (Dr. rer. nat.)

an der Fakultät für Physik

der Ludwig-Maximilians-Universität München

vorgelegt von

Anja Barfüßer

aus Donauwörth

München, 24.04.2025

Erstgutachter:	Prof. Dr. Jochen Feldmann
Zweitgutachter:	Prof. Dr. Andreas Tittl

Tag der mündlichen Prüfung: 18.06.2025

Beschränkte Exzitonen und biexzitonische optische Verstärkung in sphärischen Perowskit-Quantenpunkten

Dissertation

zur Erlangung des Doktorgrades der Naturwissenschaften (Dr. rer. nat.)

an der Fakultät für Physik

der Ludwig-Maximilians-Universität München

vorgelegt von

Anja Barfüßer

aus Donauwörth

München, 24.04.2025

Publications, Conferences, and Awards

Scientific Publications of Results Presented in This Work

- A. Barfüßer, S. Rieger, A. Dey, A. Tosun, Q. A. Akkerman, T. Debnath, J. Feldmann
  Confined Excitons in Spherical-Like Halide Perovskite Quantum Dots
  Nano Letters 22, 22, 8810-8817 (2022)

- A. Barfüßer, J. Feldmann, Q. A. Akkerman
  Biexcitonic Optical Gain in $CsPbBr_3$ *Quantum Dots*
  ACS Photonics 11, 12, 5350-5357 (2024)

Additional Publications

- I. Vinçon, A. Barfüßer, J. Feldmann, Q. A. Akkerman
  Quantum Dot Metal Salt Interactions Unraveled by the Sphere of Action Model
  Journal of the American Chemical Society 145, 26, 14395-14403 (2023)

Contributions to Conferences and Workshops

- *OPTIMA 2022: Workshop on Optical Spectroscopy of New Materials 2022 (Talk)*
  Fall-Lenggries, Germany, July 2022

- *INASCON 2022: 16th International Nanoscience Student Conference (Talk)*
  Munich, Germany, August/September 2022

- *DPG Meeting of the Condensed Matter Section 2022 (Talk)*
  Regensburg, Germany, September 2022

- *OECS 2023: 18th International Conference on Optics of Excitons in Confined Systems (Talk)*
  Lecce, Italy, June 2023

- *MATSUS24: Materials for Sustainable Development Conference (Talk)*
  Barcelona, Spain, March 2024

- *QD2024: 12th International Conference on Quantum Dots (Poster)*
  Munich, Germany, March 2024

- *E-MRS 2024 Fall Meeting (Poster)*
  Warsaw, Poland, September 2024

- *Joint CeNS/e-conversion Workshop Venice* (Poster)
  Venice, Italy, September 2024

Awards

- **Front Cover in Nano Letters**
  Volume 22, Issue 22, published in 2022

- **CeNS Publication Award, Scientific Breakthrough**
  for *“Confined Excitons in Spherical-Like Halide Perovskite Quantum Dots”* in *Nano Letters*
  Munich, Germany, November 2022

- **CeNS Publication Award, Best Junior Scientist Publication**
  for *“Quantum Dot Metal Salt Interactions Unraveled by the Sphere of Action Model”* published in *Journal of the American Chemical Society*
  Munich, Germany, December 2023

Zusammenfassung

Halbleiter-Quantenpunkte (QDs) sind vielversprechend für zahlreiche moderne Technologien, darunter lichtemittierende Bauelemente, Photovoltaik und biologische Marker. Die nanometergroßen Strukturen beschränken Ladungsträger in allen drei Raumrichtungen, wodurch diskrete, größenabhängige Energieniveaus entstehen. Dadurch lassen sich optische Eigenschaften, wie die Emissionswellenlänge, gezielt über die Größe der QDs einstellen. Besonders vielversprechend sind QDs aus Blei-Halogenid-Perowskiten (LHPs), da sie eine exzellente Lichtemission mit geringen Herstellungskosten vereinen. Im Gegensatz zu herkömmlichen Halbleitern wie CdSe, GaAs oder InP zeichnen sich LHPs durch eine hohe Toleranz gegenüber Defekten und eine vereinfachte Bandstruktur aus. Dadurch sind sie für eine effiziente Emission nicht auf Kern-Schale-Systeme angewiesen und die einzelnen Übergänge sind spektral gut voneinander getrennt. Allerdings begrenzt die inhomogene Verbreiterung in QD-Ensembles die Auflösung einzelner Übergänge, die für ein tiefgreifendes Verständnis optischer Prozesse jedoch erforderlich ist. Um etwa die Lichtverstärkung von LHP-QDs zu optimieren, muss der zugrunde liegende Mechanismus der optischen Verstärkung genau verstanden werden, der in LHP-QDs bisher verschiedenen Prozessen zugeschrieben worden ist, darunter Exzitonen, Trionen oder Biexzitonen.

Diese Arbeit präsentiert eine ausführliche Untersuchung der Energieniveaus in LHP-QDs und zeigt anhand zeitaufgelöster optischer Spektroskopie, dass die Lichtverstärkung auf einer biexzitonischen optischen Verstärkung beruht. Die Absorptionsresonanzen neuartiger monodisperser sphärischer LHP-QDs werden mit Modellrechnungen für den Fall schwacher und starker Quantenbeschränkung verglichen. Sie lassen sich dem schwachen Beschränkungsfall zuordnen, bei dem die Schwerpunktsbewegung wasserstoffartiger Exzitonen durch das QD-Potenzial eingeschränkt wird. Der angeregte Zustand wird mithilfe transienter Absorptionsspektroskopie (TA) detailliert untersucht und zeigt als dominante Beiträge induzierte biexzitonische sowie gebleichte exzitonische Übergänge. Das Identifizieren der Energien von LHP-QDs ermöglicht weiterführende Untersuchungen ihrer Lichtverstärkungseigenschaften. Zunächst wird die verstärkte spontane Emission charakterisiert, gefolgt von einer detaillierten Analyse des zugrunde liegenden optischen Verstärkungsmechanismus mittels leistungsabhängiger, spektral- und zeitlich aufgelöster TA-Spektroskopie. Die Messergebnisse weisen auf biexzitonische Verstärkung hin, basierend auf drei zentralen Argumenten: Der Verstärkungsschwellwert entspricht theoretischen Werten für Biexzitonen, seine spektrale Position überlappt mit der des energetisch niedrigsten Biexzitons und die Dauer der Verstärkung wird durch die Lebensdauer der Biexzitonen begrenzt. Diese klare Zuordnung zur biexzitonischen optischen Verstärkung ermöglicht eine gezielte Optimierung der Lichtverstärkung von LHP-QDs und ebnet den Weg für ihre Anwendung in Lasertechnologien.

Abstract

Semiconductor quantum dots (QDs) show great promise for many modern technologies, including light-emitting devices, photovoltaics, and biological labeling. These nanometer-sized structures confine charge carriers in all three dimensions, giving rise to discrete and size-dependent energy levels. Hence, by changing the size of QDs, their optical properties, such as the emission wavelength, can be tuned precisely. Lead halide perovskite (LHP) QDs are especially promising due to their excellent light emission properties combined with low fabrication costs. In contrast to conventional semiconductor materials such as CdSe, GaAs, or InP, LHPs show high defect tolerance and a simplified band structure. Therefore, they do not require core/shell systems to achieve efficient emission, and individual transitions are spectrally well separated. However, inhomogeneous broadening in QD ensembles limits the resolvability of individual transitions, which is necessary to understand optical processes in detail. For example, to optimize the light amplification properties of LHP QDs, the underlying optical gain mechanism must be understood, which so far has been attributed to various processes, including single-exciton, trion, or biexciton gain.

This thesis presents an in-depth study of the energy landscape in LHP QDs and identifies biexcitonic optical gain as the source of light amplification, based on time-resolved optical spectroscopy. The absorption resonances of novel spherical monodisperse LHP QDs are compared with model calculations considering weak and strong confinement. They are assigned to the weak confinement regime, where the center-of-mass motion of hydrogen-like excitons is confined by the QD potential. The excited state is studied in detail using transient absorption (TA) spectroscopy, revealing the dominant contributions from induced biexcitonic and bleached excitonic transitions. Identifying the energy landscape of LHP QDs enables further studies on their light amplification properties. First, amplified spontaneous emission is characterized, followed by a detailed study of the underlying optical gain mechanism through power-dependent, spectrally- and temporally-resolved TA spectroscopy. These measurements indicate biexcitonic gain based on three key arguments: The gain threshold aligns with theoretical values for attractive biexcitons, its spectral position overlaps with the energetically lowest biexciton, and the gain duration is limited by the biexciton lifetime. This clear assignment to biexcitonic optical gain enables the targeted optimization of the light amplification properties of LHP QDs, paving the way for their widespread use toward lasing applications.

Table of Contents

Zusammenfassung **vii**

Abstract **ix**

1 Introduction **1**

2 Quantum Dots and Lead Halide Perovskites **5**

2.1 Conventional Quantum Dots 6

2.1.1 Quantum Confinement Regimes 6

2.1.2 Optical Properties 10

2.1.3 Light Amplification with Quantum Dots 13

2.2 Lead Halide Perovskite Quantum Dots 17

2.2.1 Unique Properties of Lead Halide Perovskites 17

2.2.2 Lead Halide Perovskite Nanocrystals 20

2.2.3 Optical Gain in Lead Halide Perovskite Quantum Dots 21

3 Experimental Background **25**

3.1 Synthesis of Spherical Perovskite Quantum Dots 26

3.2 Steady-State Spectroscopy as First Optical Characterization Tool 27

3.2.1 Steady-State Absorption Spectroscopy 27

3.2.2 Steady-State Photoluminescence Spectroscopy 28

3.3 Transient Absorption Spectroscopy 29

3.3.1 Amplification of Ultra-Short Laser Pulses 30

3.3.2 Tuning the Wavelength of Laser Pulses 31

3.3.3 A Tool to Study the Excited State 33

3.4 Amplified Spontaneous Emission Studies 38

3.4.1 Density-Dependent Emission Detection 38

3.4.2 Variable Stripe Length Method 41

4 Confined Excitons in Lead Halide Perovskite Quantum Dots **43**

4.1 Structural and Steady-State Optical Properties 44

4.2 Assignment to the Weak Confinement Regime 46

4.3 Biexciton Formation in the Excited State 48

4.3.1 Polarization-Selective Properties Reveal Biexciton Formation 49

4.3.2 Modeling Transient Absorption Spectra 51

4.4 Dynamics of Excitonic and Biexcitonic Transitions 56

5 Biexcitonic Optical Gain in $CsPbBr_3$ Quantum Dots 59

5.1 Characterizing Amplified Spontaneous Emission 60

5.1.1 Determining the Threshold 61

5.1.2 Net Optical Gain Coefficient 62

5.2 Three Aspects Supporting Biexcitonic Optical Gain 63

5.2.1 Gain Threshold Indicates Biexcitons 65

5.2.2 Spectral Overlap with Biexciton Signal 66

5.2.3 Gain Duration Limited by Biexciton Lifetime 67

6 Summary, Conclusions, and Outlook 73

References I

Appendix XIX

List of Figures XXII

List of Tables XXIII

List of Abbreviations XXV

Acknowledgments XXVII

1

Introduction

Semiconductor technologies are essential for electronic and optoelectronic devices in everyday life, including solar cells, computers, and smartphones.[1] In particular, semiconductor-based devices have become the standard for light-emitting applications, such as displays and ambient lighting. Advancing these technologies remains a key priority, with high color purity being crucial for light emitting diodes (LEDs).[2,3] Typically, red, green, and blue LEDs are combined to produce arbitrary colors visible to the human eye. To achieve this, each LED must exhibit maximum color purity and saturation. This is also crucial for generating white light of varying qualities, often characterized by different color temperatures, such as cool bluish or more natural whites. For this purpose, narrow emission linewidths and precisely tunable emission wavelengths are essential.[4]

However, tuning bulk semiconductors is limited, as their properties are primarily determined by their crystal structure, composition, and doping.[5] A versatile solution is to use small, nanometer-sized semiconductor units, so-called quantum dots (QDs).[6] These structures confine charge carriers in all three dimensions, giving rise to the quantum size effect, which results in discrete and size-dependent energy levels. Strikingly, by tuning the size of QDs, their emission wavelength can be shifted, covering a broad spectral range.[3,5,7] The first experimental confirmations of this quantum size effect were found in the early 1980s, when size-dependent optical spectra of CuCl and CdS QDs were observed.[8–10] Subsequent advances in the colloidal synthesis of QDs in the early 1990s enabled broad investigation and application of QDs over the last decades.[11,12] For the discovery and synthesis of QDs, the Nobel Prize in Chemistry was awarded in 2023,[13] underlining their importance in advancing modern technologies. In addition to light-emitting devices,[2–4,14,15] other applications of QDs include photovoltaics,[16–18] photocatalysis,[19,20] biological labeling,[21–23] and lasers.[24,25]

A common limiting factor in achieving widespread use of a product is the cost of production. In this context, the novel material class of lead halide perovskites (LHPs) has come into the spotlight over the last decade. Initially studied mainly as thin films for photovoltaic applications,[26–30] LHP nanocrystals (NCs) have been readily available since 2015 in various shapes, sizes, and compositions.[31–33] They exhibit a high tolerance toward intrinsic defects, making their production much cheaper compared to defect-intolerant conventional semiconductors.[34,35] Therefore, LHP QDs have emerged as promising systems for LEDs or displays,[36–38] wearable electronics,[39–43] quantum light generation,[44–47] and lasers.[48–50]

To build inexpensive and efficient devices, it is essential to understand in detail the underlying properties of the materials used and their working principles. In this context, LHPs have an advantage. Their band structure is inverted compared to conventional semiconductors, which leads to a reduction in the complexity of their optical spectra.[51] However, one problem intrinsic to all QDs remains: When studying QD ensembles, even slight variations in their size and shape can lead to an inhomogeneous broadening of optical spectra, limiting the resolvability of individual absorption resonances.[52,53] A recently introduced synthesis method allows one to readily produce monodisperse spherical LHP QDs with distinct absorption resonances.[54]

This thesis presents the first in-depth study of spherical LHP QDs using optical spectroscopy techniques. The underlying quantum confinement is analyzed and a theoretical model is assigned that properly describes the excitonic nature and the energy landscape of the QDs. Furthermore, excited-state properties are studied and found to be dominated by exciton bleaching and biexciton formation. Based on this, the potential of the spherical QDs toward lasing applications is tested. Light amplification in QD films is observed and the underlying optical gain mechanism is studied in detail using time-resolved optical spectroscopy. By identifying the underlying energy landscape of center-of-mass motion-confined excitons and biexcitons, this thesis lays the foundation for further studies on the optical properties of spherical LHP QDs. The identified biexcitonic nature of optical gain adds to the knowledge about light amplification in LHP NCs and provides a basis for the targeted optimization of their light amplification properties toward lasing applications.

The content of this thesis is structured as follows: First, the theoretical background in Chapter 2 provides an overview of the underlying physical concepts that are essential to this thesis and reviews the relevant literature. Next, the experimental background is introduced in Chapter 3, including a concise overview of the QD synthesis and a detailed description of the spectroscopic techniques used throughout this thesis. The presented results are divided into two parts. Chapter 4 highlights the findings on the energy landscape and transitions from the ground and an excited state of spherical LHP QDs. Based on these results, Chapter 5 presents the light amplification properties of $CsPbBr_3$ QDs and the underlying optical gain mechanism. Finally, Chapter 6 summarizes the results presented in this thesis and provides a comprehensive conclusion including an outlook on future directions and opportunities.

2

Quantum Dots and Lead Halide Perovskites

This chapter introduces the theoretical concepts relevant to this thesis, including a concise overview of the literature. It is structured into two parts. Section 2.1 introduces semiconductor QDs in general, with a focus on the weak and strong confinement models. Furthermore, the optical properties of conventional QD materials are discussed, particularly their light amplification. Section 2.2 introduces the material class of lead halide perovskites (LHPs) and compares their unique properties, such as high defect tolerance and inverted band structure, with those of conventional semiconductors. As a result, LHP QDs offer excellent light emission properties without the core/shell engineering necessary for conventional QDs. In addition, their optical properties and amplified spontaneous emission (ASE) characteristics are discussed.

2.1 Conventional Quantum Dots

2.1.1 Quantum Confinement Regimes

Charge carriers in a crystal are influenced by the periodic potential of the atom cores. They can be described as quasi-free particles by applying the effective mass approximation, which assigns charge carriers an effective mass m^* which is given by[55]

$$m^* = \left(\frac{1}{\hbar^2} \frac{\mathrm{d}^2 E}{\mathrm{d}k^2} \right)^{-1} . \tag{2.1}$$

Hence, the effective masses of electrons m_e^* and holes m_h^* depend on the curvature of the respective energy bands in k-space.[55] While a crystal is theoretically considered infinitely large, when its size is reduced, the effective mass approximation can still be applied as long as the crystal size is much larger than the lattice constant.[56] However, a small crystal size imposes significant boundary conditions on the charge carriers, which hence are treated as 'particles-in-a-box'.[53] Figure 2.1a illustrates an electron confined in an infinite square potential well with the resulting discrete energy levels depending on the quantum number n. Semiconductor nanostructures that are quantum confined in all three dimensions are called quantum dots (QDs).[6]

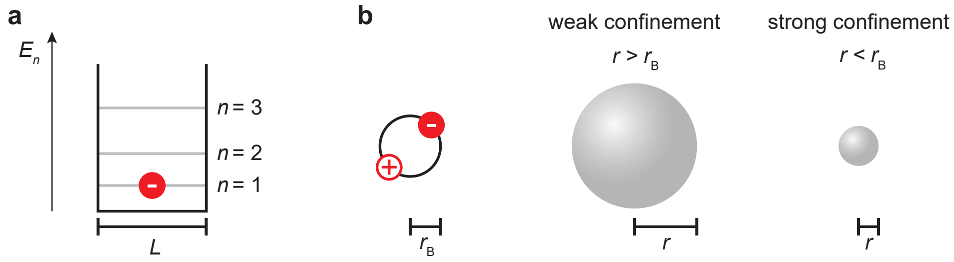

Figure 2.1: Quantum Confinement Regimes. (a) Electron confined in a one-dimensional infinite square potential well of length L, yielding discrete energy levels for the electron characterized by the quantum number n. **(b)** Comparison of the exciton Bohr radius r_B with the QD radius r, describing the weak ($r > r_\mathrm{B}$) and strong ($r < r_\mathrm{B}$) confinement regimes. The QDs are represented by the gray spheres.

Considering a particle with mass m in a three-dimensional infinite spherical potential with radius r, textbook quantum mechanics yields the allowed eigenenergies $E_{n,l}$ which simplify in the case of quantum number $l = 0$ to

$$E_{n,l} = \frac{\hbar^2 \chi_{n,l}^2}{2mr^2} = \frac{\hbar^2 \pi^2 n^2}{2mr^2}, \tag{2.2}$$

with $\chi_{n,l}$ being the root with number n of the spherical Bessel function of order l.[53,57]

In addition to the confinement potential, the Coulomb interaction between negatively charged electrons and positively charged holes must be considered when discussing semiconductors. This can lead to the formation of so-called Wannier-Mott excitons if their binding energy is larger than the thermal energy. Wannier-Mott excitons also form in bulk crystals and are typically described in analogy to the hydrogen atom.[58] In this context, the two-particle (electron and hole) problem can be reduced to a one-particle (exciton) problem by separating the collective center-of-mass motion with the total mass $M = m_\mathrm{e}^* + m_\mathrm{h}^*$ from the relative motion with the reduced mass $\mu = \frac{m_\mathrm{e}^* m_\mathrm{h}^*}{m_\mathrm{e}^* + m_\mathrm{h}^*}$.[53] Such an exciton is illustrated in Figure 2.1b on the left, including its exciton Bohr radius r_B which is defined similarly to the Bohr radius of the hydrogen atom as

$$r_\mathrm{B} = \frac{4\pi\varepsilon\varepsilon_0\hbar^2}{\mu e^2}, \tag{2.3}$$

with the dielectric constant of the considered crystal ε, the vacuum permittivity ε_0, and the elementary charge e. Typical values for r_B are between ~1 nm and several tens of nm.[1,59] Before highlighting the influence of quantum confinement, the dispersion relation of an exciton in a bulk semiconductor is discussed, which is given by

$$E_{n_\mathrm{r}}(\mathbf{K}) = E_\mathrm{gap} - \frac{Ry^*}{n_\mathrm{r}^2} + \frac{\hbar^2\mathbf{K}^2}{2M}, \tag{2.4}$$

with the band gap energy E_gap of the bulk crystal and the internal hydrogen-like exciton states characterized by the exciton Rydberg energy $Ry^* = \frac{\mu e^4}{2\hbar^2(4\pi\varepsilon\varepsilon_0)^2}$ and the quantum number n_r. The last term characterizes the kinetic energy of the exciton with the wave vector $\mathbf{K}$.[53]

To describe the energy levels of an actual QD, both the confinement potential of the QD and the Coulomb interaction between electron and hole must be combined.[60] There are two limiting cases that can be distinguished depending on the ratio between the QD radius r and the exciton Bohr radius r_B: For $r > r_\mathrm{B}$, the weak confinement regime is appropriate, while for $r < r_\mathrm{B}$ the strong confinement regime is applicable. The two confinement regimes are illustrated in Figure 2.1b.

The Weak Confinement Regime

The weak confinement regime considers QDs with $r > r_\mathrm{B}$ which are still quantum confined. CuCl QDs, which were the first to be reported, were assigned to this confinement regime.[8] As CuCl has a relatively small Bohr radius of $r_\mathrm{B} \approx 0.7$ nm,[53] all CuCl QDs reported fulfill $r > r_\mathrm{B}$.[61] This regime is dominated by excitonic properties, so electrons and holes form hydrogen-like Wannier-Mott excitons (see Figure 2.2a) with their center-of-mass motion confined by the QD potential (see Figure 2.2b).

To derive the energy levels in the weak confinement regime, the dispersion relation for bulk excitons in Equation 2.4 is taken as a starting point. However, the kinetic energy term of the free exciton has to be replaced by the discrete energy levels of a particle-in-a-box.[53,62] This

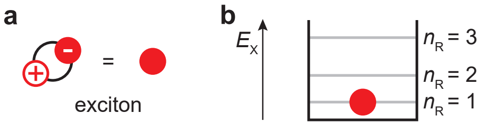

Figure 2.2: Weak Confinement Model. (a) Electron and hole forming a Wannier-Mott exciton. **(b)** Confinement of the exciton in its center-of-mass motion, here illustrated in a one-dimensional infinite square potential well. The discrete energy levels E_X of the center-of-mass motion of the exciton are characterized by the quantum number n_R.

'exciton-in-a-box' can be derived for an infinite spherical potential analogue to Equation 2.2, again using $l = 0$ to consider selection rules for photon absorption in semiconductors. The energy levels for the weak confinement regime are given by[53]

$$E_{n_r,n_R} = E_{gap} - \frac{Ry^*}{n_r^2} + \frac{\hbar^2\pi^2 n_R^2}{2Mr^2}. \tag{2.5}$$

The quantum number n_r describes the energies of the relative motion, while n_R denotes the energies of the confined center-of-mass motion of the exciton. Note that in this confinement regime, electrons and holes move coherently as a hydrogen-like exciton. In relatively large QDs, this collective behavior of electron and hole can lead to interesting effects such as superradiance.[63–66]

The Strong Confinement Regime

Most of the III-V and II-VI QDs studied are in the strong confinement regime with $r < r_B$.[67] In this regime, electron and hole are confined individually by the QD potential, as illustrated in Figure 2.3a.

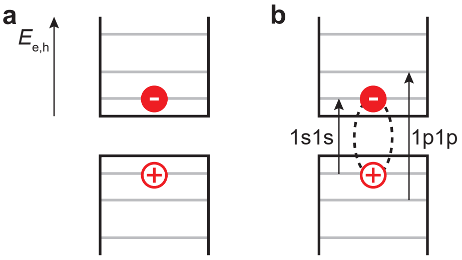

Figure 2.3: Strong Confinement Model. (a) Electron and hole are confined individually by the QD potential, here illustrated as one-dimensional infinite square potential wells. **(b)** The Coulomb interaction between the confined charge carriers is illustrated with the dashed line. 1s1s (1p1p) denotes the transition between the 1s (1p) hole and the 1s (1p) electron levels.

Again using Equation 2.2, the discrete energy levels of an electron and a hole in an infinite spherical potential ($E^e_{n,l}$ and $E^h_{n,l}$, respectively) can be written as[53]

$$\begin{aligned} E^{\mathrm{e}}_{n,l} &= E_{\mathrm{gap}} + \frac{\hbar^2 \chi^2_{n,l}}{2m^*_{\mathrm{e}} r^2}, \\ E^{\mathrm{h}}_{n,l} &= \frac{\hbar^2 \chi^2_{n,l}}{2m^*_{\mathrm{h}} r^2}. \end{aligned} \tag{2.6}$$

This strongly overestimates the energies of the charge carriers as the Coulomb interaction is not included. Due to the small QD size to which the charge carriers are confined, it is essential to also include their Coulomb interaction. Its contribution can actually be even larger in the strong confinement regime than in the weak confinement regime. However, when including the Coulomb interaction, the relative and center-of-mass motion cannot be separated like in the weak confinement model. Instead, the energy levels of the first allowed transitions $E_{1\mathrm{s}1\mathrm{s}}$ and $E_{1\mathrm{p}1\mathrm{p}}$, which are illustrated in Figure 2.3b, can be written as[53,56]

$$\begin{aligned} E_{1\mathrm{s}1\mathrm{s}} &= E_{\mathrm{gap}} + \pi^2 \left(\frac{r_{\mathrm{B}}}{r}\right)^2 Ry^* - 1.786 \frac{r_{\mathrm{B}}}{r} Ry^* - 0.248 Ry^*, \\ E_{1\mathrm{p}1\mathrm{p}} &= E_{\mathrm{gap}} + 4.493^2 \left(\frac{r_{\mathrm{B}}}{r}\right)^2 Ry^* - 1.884 \frac{r_{\mathrm{B}}}{r} Ry^*. \end{aligned} \tag{2.7}$$

Note that such Coulomb-bound electron-hole pairs are not hydrogen-like excitons like in the weak confinement model, as they do not have a correlated motion.[53,66]

Clarification of Terminology

At this point, a common inconsistency in the usage of the term 'exciton' shall be addressed. As discussed above, in the weak confinement model, the considered quasi-particles are Wannier-Mott excitons to which a relative and a center-of-mass motion is assigned in analogy to the hydrogen atom. These excitons are confined in their center-of-mass motion by the QD potential. In the strong confinement model, electron and hole are individually confined by the QD before the Coulomb interaction is taken into account. Although such an electron-hole pair is Coulomb-bound as well, one cannot separate a relative and a center-of-mass motion analogue to the hydrogen atom. However, this is commonly also referred to as exciton. In order to differentiate the different concepts of electron-hole pairs, in the course of this thesis, only hydrogen-like excitons as referred to as excitons, whereas the other are called one-pair states.[56]

The terminology becomes even more complex if more than one electron and one hole are excited in a QD. This is illustrated in Figure 2.4a with simplified two-level systems. On the left, a one-pair state is shown. A negatively (positively) charged one-pair state consists of two electrons (two holes) and one hole (one electron), illustrated in Figure 2.4a in the middle. A Coulomb-bound charged one-pair state is typically called trion.[68] The situation of two electron-hole pairs in a system is shown in Figure 2.4a on the right. Although the term biexciton is typically used, here it is referred to as 'two-pair state' because it does not consist of two hydrogen-like excitons.[69,70] It should be highlighted that binding energies cannot be correctly included in this representation. Binding energies are often neglected in such schemes for simplicity, but for strongly confined QDs, the Coulomb interaction can actually be substantial.[53]

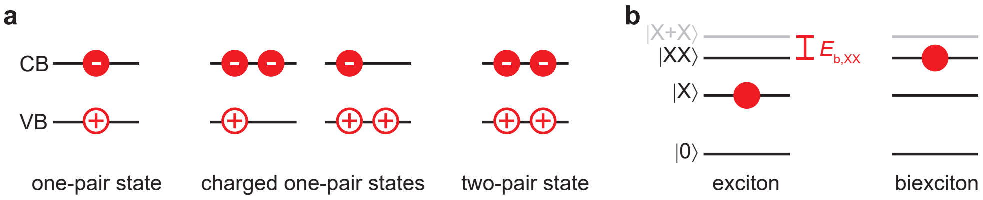

Figure 2.4: Multi-Particle States. (a) Electron-hole picture illustrating a one-pair state (left), negatively and positively charged one-pair states (middle), and a two-pair state (right). **(b)** Level scheme illustrating an exciton and a biexciton including the biexciton binding energy $E_{\mathrm{b,XX}}$.

Figure 2.4b illustrates what is referred to as exciton and biexciton in this thesis. The biexciton actually consists of two Coulomb-bound hydrogen-like excitons, and the biexciton binding energy $E_{\mathrm{b,XX}}$ is displayed properly.

2.1.2 Optical Properties

The influence of quantum confinement on the energy levels of charge carriers, also in connection with the Coulomb interaction, was introduced in Subsection 2.1.1. The size dependence of the energy levels leads to size-dependent optical properties of QDs, which are discussed in the following. While QDs can be produced using different methods, such as colloidal synthesis,[7,10] epitaxial growth,[71,72] or embedded in a glass matrix,[8,61,73,74] their theoretical principles remain the same. A prerequisite for colloidal QDs, which are the focus of this thesis, is their colloidal stability, provided by ligands attached to the surface of the QDs.[12,75]

Core/Shell Quantum Dots

A big problem with the first QDs was their low photoluminescence quantum yield (PLQY) of only a few percent. The defect-rich surface with dangling bonds can effectively trap charge carriers.[13,76] This was resolved by a passivation layer around the QDs (between the QD and the ligands) with a wider band gap material in a type-I alignment, as illustrated in Figure 2.5a, such as ZnS around CdS. This step-wise potential well confines excited charge carriers to the QD core and separates them from the defect-rich surface, strongly increasing the PLQY.[77,78] Another opportunity arises when there is a particularly thick shell around a small core. The thick shell increases the absorption cross-section of the QD, while emission still occurs from the core, to which the charge carriers relax.[25]

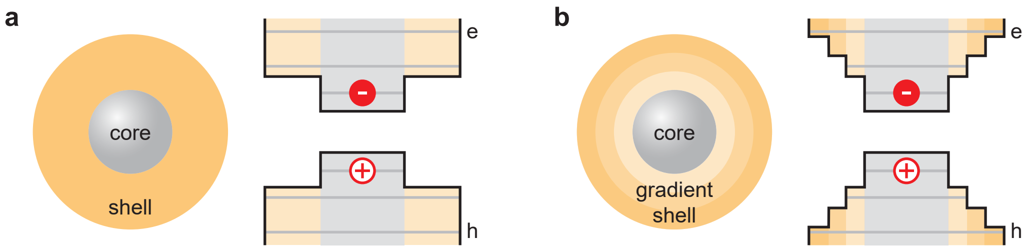

Figure 2.5: Core/Shell Quantum Dots. Illustration and corresponding step-wise potential well of **(a)** a core/shell QD with type-I alignment and **(b)** an almost continuously graded core/shell QD. Both configurations confine an electron-hole pair to the core.

Furthermore, core/shell systems are not restricted to two materials with a sharp interface between them. An alloy layer can create a gradient shell that allows an almost continuous composition tuning in the shell, as illustrated in Figure 2.5b. Examples include CdSe/$CdSe_xS_{1-x}$ QDs and CdSe/$Cd_xZn_{1-x}Se$ QDs, where $x = 1$ at the innermost part of the shell and gradually decreases to $x = 0$ towards the outer region of the QD.[79,80] Thick shells reduce blinking of QDs, improving their single-photon emission properties due to the separation of charge carriers from surface defects which suppresses charging.[81–83] QDs with gradient shells are especially useful in the context of optical gain, which will be discussed in Subsection 2.1.3, as they suppress non-radiative Auger recombination, which is introduced below.

Linewidth Broadening

The linewidth of a QD ensemble has several contributions. The first is the natural linewidth, due to the finite lifetime of an excited state and the uncertainty principle. Identical QDs in an ensemble all have the same natural linewidth; hence, it falls under the category of homogeneous broadening, which yields a Lorentzian lineshape of, e.g., emission spectra.[84] Another example of homogeneous broadening arises from the scattering processes of charge carriers with phonons. This contribution can be minimized by lowering the temperature of the system and hence reducing lattice vibrations, i.e., phonons.[85]

However, precise control over the size and shape of QDs remains challenging. Ensembles of QDs typically exhibit a distribution in QD sizes and shapes, even within one synthesis batch. Furthermore, the local environment and surface structure can vary between individual QDs. These inhomogeneities influence the absorption and emission spectra of QD ensembles, leading to inhomogeneous broadening.[52,53] For a random distribution of the different emission energies, this yields a Gaussian emission profile.[84] Therefore, the discrete energy landscape of QDs might be hidden in ensemble measurements due to inhomogeneous broadening.

Charge Carrier Dynamics

Two-fold degenerate discrete energy levels in QDs can each be populated by two charge carriers, following Pauli's exclusion principle. This applies to both electrons and holes, as they are fermions with half-integer spins.[57] Excitons and biexcitons have integer spins and can thus be considered bosons. However, they are composite bosons made up of coupled fermions. Hence, their bosonic character only holds when interactions between their constituents are negligible, that is, when their spacing is much larger than their associated size, as in dilute gases.[59,86–89] This is not the case for the QDs discussed in this thesis; hence, the fermion character of the exciton and biexciton constituents is relevant.

Optical properties and charge carrier dynamics of QDs have been extensively investigated,[56,61,67,90–93] including the fine structure of neutral and charged excitons,[94,95] many-body Coulomb and spin effects,[96,97] charge carrier multiplication,[98–100] or hot carrier cooling.[70,101,102] A particular case of non-radiative recombination, so-called Auger recombination, is highlighted in the following. It can occur both in bulk and confined systems if more than one electron-hole pair is excited, i.e., under high fluence excitation. It is a three-particle process involving two electrons (two holes) and one hole (one electron).[91,103] One electron-hole pair recombines and transfers its energy to the third charge carrier that is excited to a higher energy level from which it can relax non-radiatively by emitting phonons.[91,104] Such an Auger process is illustrated in Figure 2.6a, on the left for a bulk material in the so-called one-particle picture and on the right for discrete energy levels.

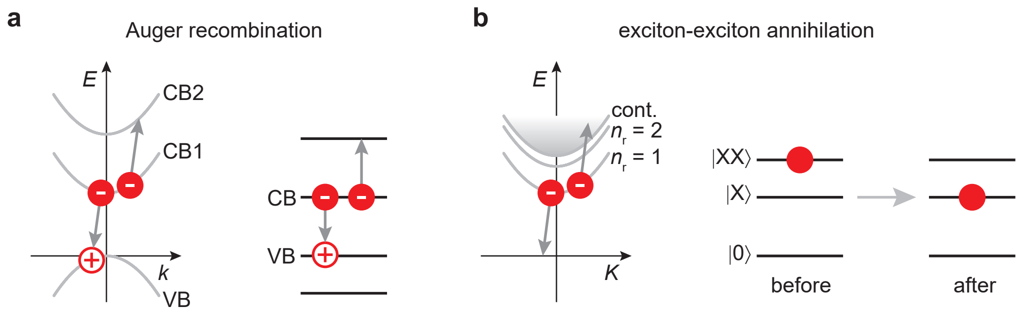

Figure 2.6: Auger Recombination and Exciton-Exciton Annihilation. (a) One-particle picture illustrating Auger recombination in a bulk semiconductor (left) and a simplified system with discrete energy levels (right). **(b)** Two-particle picture illustrating exciton-exciton annihilation in a bulk semiconductor (left) with the two energetically lowest exciton states ($n_r = 1$ and $n_r = 2$) and the continuum shown, and a confined excitonic system (right) for which the energy levels before and after exciton-exciton annihilation are displayed.

In the exciton picture, the corresponding process is called exciton-exciton annihilation,[105] which is illustrated in Figure 2.6b, on the left for a bulk semiconductor in the two-particle picture. In analogy to Auger recombination, the energy of one exciton is transferred to a second exciton which gets excited to a higher energy level from which it relaxes non-radiatively. In Figure 2.6b on the right, the initial biexciton and the final relaxed exciton state are shown in a discrete level system.

Furthermore, Coulomb interactions are enhanced in confined systems compared to bulk because charge carriers are forced into close proximity increasing wave function overlap, while reduced screening leads to stronger dielectric confinement.[12,91,106] Therefore, Auger processes are enhanced in QDs, and a 'universal volume scaling' of Auger lifetimes τ_{Auger} has been found that holds true for a multitude of QD materials: $\tau_{\mathrm{Auger}} = \gamma \cdot V$, with $\gamma \approx 1\,\mathrm{ps/nm^3}$ for II-VI semiconductor QDs. Typical values of τ_{Auger} are between a few and hundreds of ps, which is shorter than the radiative lifetime of biexcitons in QDs, rendering Auger recombination the main decay channel for two-pair states.[25,91,107] In general, the radiative lifetimes of excitons $\tau_{\mathrm{r,X}}$, trions $\tau_{\mathrm{r,X^{\pm}}}$, and biexcitons $\tau_{\mathrm{r,XX}}$ can be considered as $\tau_{\mathrm{r,X}} > \tau_{\mathrm{r,X^{\pm}}} > \tau_{\mathrm{r,XX}}$.[68,79,108,109] The competition between radiative and non-radiative pathways is detrimental to many applications, such as light amplification.[109] The following Subsection 2.1.3 introduces the potential of QDs for light amplification and summarizes advancements achieved so far.

2.1.3 Light Amplification with Quantum Dots

Light amplification plays a crucial role in lasers, with the name itself being an acronym for 'light amplification by stimulated emission of radiation', reflecting their fundamental principle. A laser requires a gain medium, in which the actual light amplification takes place. This material is located inside a cavity that provides enhanced interaction of the amplified light with the gain medium and ensures proper extraction of the light. This can be achieved by, e.g., a high-reflective and a partially reflective mirror. A population inversion is created in the gain medium by excitation with a pump. It can be pumped either optically by another laser or electrically like in diode lasers.[110] When population inversion is achieved, the probability of stimulated emission exceeds that of absorption, resulting in optical gain. A common gain medium, which is also installed in the amplifier system described in Subsection 3.3.1, is a $\mathrm{Ti^{3+}}$-doped $\mathrm{Al_2O_3}$ (Ti:Sapphire) crystal. Optical gain can be realized in three- or four-level systems, with the latter illustrated in Figure 2.7a.

Here, the system is pumped optically by absorbing a photon with the energy corresponding to the energy difference $|0\rangle \longrightarrow |3\rangle$. After rapid non-radiative relaxation to $|2\rangle$, a population inversion between the levels $|2\rangle$ and $|1\rangle$ is created, so that a photon with the energy of the respective energy difference induces stimulated emission $|2\rangle \longrightarrow |1\rangle$ before rapid non-radiative relaxation puts the system back to $|0\rangle$. For light amplification, a population inversion is crucial, which means that the population of $|2\rangle$ is higher than that of $|1\rangle$ so that stimulated emission $|2\rangle \longrightarrow |1\rangle$ has a higher probability than absorption $|1\rangle \longrightarrow |2\rangle$. This is promoted by the mentioned fast non-radiative relaxation processes illustrated in Figure 2.7a.[111]

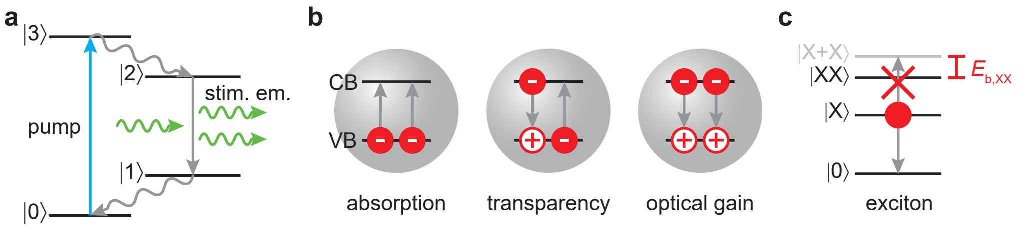

Figure 2.7: Optical Gain in Different Systems. (a) Optical gain in a four-level system which is pumped from $|0\rangle \longrightarrow |3\rangle$. Rapid non-radiative relaxation from $|3\rangle \longrightarrow |2\rangle$ and $|1\rangle \longrightarrow |0\rangle$ (gray wavy arrows) supports a population inversion between the levels $|2\rangle$ and $|1\rangle$ between which stimulated emission occurs. **(b)** Absorption, transparency, and optical gain in QDs without biexciton binding energy. **(c)** Level scheme of an exciton for which absorption to the attractive biexciton with binding energy $E_{\mathrm{b,XX}}$ is at a lower energy compared to stimulated emission to the ground state.

Optical Gain in Quantum Dots

Figure 2.7b shows QDs with energy bands simplified to two-level systems, where each level is two-fold degenerate. One can distinguish between three cases depending on the occupation of the levels: First, both electrons are in the ground state, so a photon with suitable energy can only induce absorption (shown on the left). Second, if one electron-hole pair is already created, a subsequent photon has an equal probability of being absorbed or of inducing stimulated emission from the excited electron-hole pair, effective leading to transparency (shown in the middle). Finally, with two excited electron-hole pairs, population inversion is achieved, and a photon can only induce stimulated emission. This is referred to as optical gain (shown on the right). A single electron-hole pair is therefore not sufficient to achieve optical gain; instead, a two-pair state is necessary.[24] It is apparent that by resonantly pumping such a two-level system, a population inversion cannot be reached but only transparency. Hence, three- or four-level systems are typically employed, as they allow for non-resonant pumping (see also Figure 2.7a).

In the following, a closer look is taken at the threshold population N_{th} at which optical gain is reached in an ensemble of two-fold degenerate two-level systems, i.e. the transition from transparency to optical gain, as illustrated in Figure 2.7b. Assuming the electron-hole pair population is the same in every QD of the ensemble, the threshold is given by $N_{\mathrm{th}} = 1$.[112] However, this value does not consider the Poissonian nature of coherent laser light,[88] which is typically used to excite QDs. The number of electron-hole pairs excited per QD follows Poisson statistics. The probability $P(\langle N\rangle, N)$ of having N electron-hole pairs excited in a selected QD when the average population of the QD ensemble is $\langle N\rangle$, is given by[90]

$$P(\langle N\rangle, N) = \frac{\langle N\rangle^N}{N!} e^{-\langle N\rangle}. \tag{2.8}$$

As stimulated emission and absorption in a one-pair state compensate each other, optical gain relies on two-pair states. By introducing the probabilities of a QD being in the ground, one-, or two-pair state (P_0, P_X, and P_XX, respectively), the optical gain threshold can be written as population inversion between the two-pair state and the ground state:[79,113]

$$P_0 = P_\mathrm{XX}. \tag{2.9}$$

Relating these probabilities to the Poisson statistics from Equation 2.8, $P_0 = P(\langle N \rangle, 0)$, and $P_\mathrm{XX} = 1 - P(\langle N \rangle, 0) - P(\langle N \rangle, 1)$, Equation 2.9 can be expanded as

$$e^{-\langle N \rangle_\mathrm{th,XX}} = 1 - e^{-\langle N \rangle_\mathrm{th,XX}} - e^{-\langle N \rangle_\mathrm{th,XX}} \langle N \rangle_\mathrm{th,XX}. \tag{2.10}$$

This yields the two-pair state optical gain threshold $N_\mathrm{th,XX} \approx 1.15$. Note that this threshold value does not include a binding energy between the two electron-hole pairs. Figure 2.7c illustrates the level scheme for an excitonic system with a binding energy $E_\mathrm{b,XX}$. In this case, the absorption to the attractive biexciton state $|\mathrm{X}\rangle \longrightarrow |\mathrm{XX}\rangle$ is energetically redshifted by $E_\mathrm{b,XX}$ relative to the stimulated emission $|\mathrm{X}\rangle \longrightarrow |0\rangle$ and the reabsorption $|0\rangle \longrightarrow |\mathrm{X}\rangle$ of another QD. The larger $E_\mathrm{b,XX}$ is, the more the competition between these processes is reduced, which lowers the optical gain threshold.[114]

An analogous consideration for the threshold value can be made for charged one-pair states or trions (see also Figure 2.4a), again without including binding energies. In the case of a two-level system with two-fold degeneracy, a charged one-pair state cannot absorb another photon. Instead, a photon with the respective energy can only induce stimulated emission. Therefore, to achieve optical gain, a population inversion has to be reached between the charged one-pair state and the ground state:

$$P_{0^-} = P_{\mathrm{X}^-}, \tag{2.11}$$

with the probabilities of a QD to be in the charged ground or charged one-pair state $P_{0^-} = P(\langle N \rangle, 0)$ or $P_{\mathrm{X}^-} = 1 - P(\langle N \rangle, 0)$. The optical gain threshold $\langle N \rangle_{\mathrm{th,X}^-}$ can therefore be extracted from[113]

$$e^{-\langle N \rangle_{\mathrm{th,X}^-}} = 1 - e^{-\langle N \rangle_{\mathrm{th,X}^-}}, \tag{2.12}$$

yielding $\langle N \rangle_{\mathrm{th,X}^-} \approx 0.69$. Compared to bulk semiconductors with continuous energy bands, population inversion in QDs can be reached at much lower concentrations of excited charge carriers due to their discrete energy levels. Furthermore, oscillator strengths in QDs are enhanced,[115] and thermal depopulation of individual energy levels is suppressed if the spacing between energy levels is larger than the thermal energy.[116] This has made QDs highly attractive for lasing applications.[24,25]

However, the small size of QDs also presents a disadvantage. As mentioned above, an electron-hole pair alone is not sufficient to achieve optical gain, and the population of a two-pair state (or at least a charged one-pair state) is essential. However, as discussed in Subsection 2.1.2, non-radiative Auger recombination and exciton-exciton annihilation scale linearly with the QD volume, meaning that the smaller the QD, the faster these non-radiative processes are. Consequently, non-radiative Auger recombination and exciton-exciton annihilation are the main limitations of optical gain in QDs.[25,112,117]

Advancements through Core/Shell Engineering

Extensive research efforts have been employed by the QD community to optimize the potential of QDs for light amplification, with the goal of using them as an electrically pumped gain medium in highly efficient lasers.[24,25,118] Two key aspects have been addressed in conventional II–VI semiconductor QDs to enhance their performance. One effort is prolonging the gain lifetime by developing ways to slow down non-radiative Auger recombination and exciton-exciton annihilation. The second aspect, which also inherently addresses the first one, is lowering the optical gain threshold. This can be achieved by systems that do not rely on two-pair states for optical gain.

To reduce the probability for Auger recombination, core/shell QDs have been developed with particularly thick and continuously graded shells, as shown in Figure 2.5. Several aspects of this method are beneficial: The thick shell reduces the non-radiative recombination rate according to the volume scaling discussed in Subsection 2.1.2. Furthermore, a QD potential that confines, e.g., the hole to the small core while the electron is delocalized over the whole QD, reduces their wave function overlap and hence Auger recombination.[81,119] An especially important aspect is the actual shape of the confinement potential.[120] Smooth rather than step-like confinement potentials reduce the overlap of spatial frequencies between initial and final states. This reduces the transition probability of the excess charge carrier (see Figure 2.6) and hence the Auger rate.[109,121–123]

It was already shown in Equation 2.10 and Equation 2.12 that the optical gain threshold for charged one-pair states $\langle N\rangle_{\mathrm{th,X^-}} \approx 0.69$ is lower than that for two-pair states $N_{\mathrm{th,XX}} \approx 1.15$. This can be utilized by deliberately charging QDs, enabling a population inversion to arise at a lower, almost zero threshold.[113,124,125] In the context of core/shell engineering, reducing the wave function overlap between electron and hole can also eliminate the need for two-pair states altogether: By confining electrons to the core and holes to the shell of a type-II core/shell QD, as illustrated in Figure 2.8a, the repulsion due to Coulomb interaction between two electrons and between two holes is enhanced.[126,127] If this repulsion is stronger than the attractive Coulomb contribution between electrons and holes, the resulting two-pair state is repulsive. Figure 2.8b illustrates the level scheme of an excitonic system. Here, the absorption to the repulsive biexciton $|\mathrm{X}\rangle \longrightarrow |\mathrm{XX}\rangle$, which has a binding energy $E_{\mathrm{b,XX}}$, is energetically at a higher energy (blueshifted) than stimulated emission to the ground state $|\mathrm{X}\rangle \longrightarrow |0\rangle$. If this shift is larger than the linewidth of the QD ensemble, single-exciton gain is achieved.[126] Note that such single-exciton gain is also possible for an attractive biexciton system if the biexciton binding energy is high enough.[128]

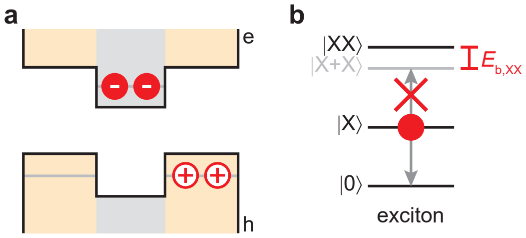

Figure 2.8: Type-II Core/Shell Quantum Dot. (a) Type-II core/shell QD confining electrons to the core and holes to the shell, increasing Coulomb repulsion. **(b)** Level scheme of an exciton for which absorption to the repulsive biexciton with binding energy $E_{\text{b,XX}}$ is blueshifted relative to stimulated emission to the ground state.

Application Fields and Challenges

The size tunability and narrow emission linewidths of QDs, as well as their low optical gain thresholds and solubility in water have made them a promising and widely used material system for a variety of applications,[5,7,129,130] such as light-emitting devices and displays,[2–4,14,15] photovoltaics,[16–18] infrared photodetectors,[131,132] biological labels,[21–23] quantum light sources,[133,134] photocatalysis,[19,20] and lasers.[24,25] However, especially the emission properties of conventional QDs rely on core/shell designs to reduce the influence of surface defects, as discussed in Subsection 2.1.2. Furthermore, the band structures of conventional II-VI and III-V QD materials exhibit a degeneracy close to the band gap, resulting in a limited energetic separation of discrete levels in such QDs. Both of these challenges can be effectively resolved by the relatively novel material class of perovskites, which is introduced and compared to conventional semiconductor materials in the following section.

2.2 Lead Halide Perovskite Quantum Dots

2.2.1 Unique Properties of Lead Halide Perovskites

The material class of lead halide perovskites (LHPs) was first discovered in 1893.[26] However, they became a vital part of active research only much later when their high potential for photovoltaics was discovered in 2009.[26] The typical crystal structure of perovskites, with their characteristic ABX_3 stoichiometry, is illustrated in the unit cell in Figure 2.9a. In LHPs, A^+ are organic or inorganic cations (e.g., formamidinium FA^+, methylammonium MA^+, or Cs^+), which are in the corners of the unit cell. B^{2+} are metal cations (Pb^{2+} or alternatively, e.g., Sn^{2+}) in the center, and X^- are halide anions (e.g., Cl^-, Br^-, I^-) located at the face centers of the unit cell. Corner-sharing $[BX_6]^{4-}$ octahedra form interconnections across the crystal, as highlighted in Figure 2.9b.[135] While a cubic unit cell is illustrated in Figure 2.9, composition and temperature-dependent tilting of the octahedra can alter the crystal phase to, e.g., orthorhombic for $CsPbBr_3$ at room temperature.[34,135]

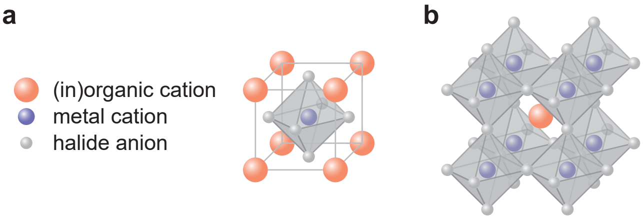

Figure 2.9: Perovskite Unit Cell and Crystal Structure. Illustration of **(a)** a cubic unit cell of LHPs and **(b)** their crystal structure highlighting the corner-sharing octahedra.

The combination of elements forming a perovskite structure is restricted by the so-called Goldschmidt tolerance factor and octahedral factor.[136] They characterize the stability of the structure and the octahedral stability, respectively, depending on the ionic radii of the components. Elemental mixtures for A^+, B^{2+}, and X^- sites are also possible. In contrast to the mostly covalent character of conventional II-VI and III-V semiconductors, LHPs are mainly formed by ionic bonds. Therefore, LHPs have a relatively soft lattice, with some even attributing liquid-like properties to them.[36]

Defect Tolerance

An important property of LHPs is their defect tolerance, which is in contrast to the defect intolerance of conventional semiconductors. This is based on their electronic band formation that is illustrated in Figure 2.10. In II-VI and III-V semiconductors, the conduction band (CB) is typically formed by antibonding states, while the valence band (VB) is formed by bonding states, see Figure 2.10a. Elemental displacements or vacancies create dangling bonds, leading to mid-gap states that act as charge carrier traps (illustrated in blue). Such deep traps are energetically shifted far from the CB and VB so they cannot be depopulated by thermal energy. As trap states promote non-radiative recombination, they drastically reduce the PLQY of the material.[34,35]

On the other hand, both the CB and VB forming the direct band gap of LHPs are composed of antibonding states, see Figure 2.10b. As a result, trap states from dangling bonds at the crystal surface are located in the bands or are energetically close to them as so-called shallow traps. This makes the optical and electronic properties of LHPs largely unaffected by intrinsic defects, such as vacancies, despite their relatively low formation energies.[34,36,137] The tolerance toward intrinsic defects enables high emission efficiencies and excellent charge-transport properties, making LHPs a highly promising material class for efficient light-emitting applications and photovoltaic technologies. Furthermore, LHPs are associated with low-cost fabrication, since intrinsic defects are not detrimental to their performance.[34,135,138] The band

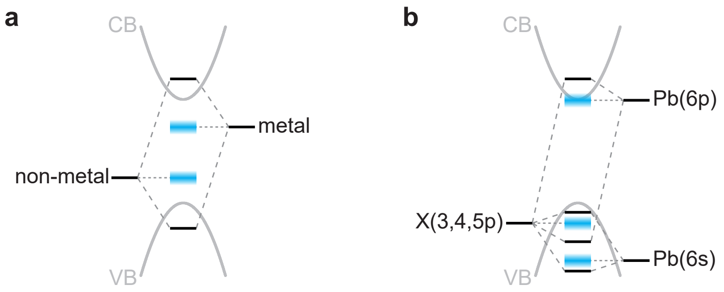

Figure 2.10: Electronic Band Formation. Simplified illustration of the formation of the CB and VB of **(a)** conventional semiconductors, such as CdSe or GaAs, with associated mid-gap trap states in blue, compared to **(b)** LHPs with associated intra-band and shallow trap states in blue.

gap of LHPs is formed by Pb and halide orbitals as shown in Figure 2.10b. Hence, the band gap energy is largely independent of the A-site cation and, notably, can be easily tuned by the halide composition. Moreover, the CB of LHPs is formed by p-type orbitals, while the VB has a strong contribution from s-type orbitals. This has a significant influence on their band structure and is discussed in the following.

Inverted Band Structure

The band structure of LHPs is inverted relative to conventional II-VI and III-V semiconductors, which is illustrated in Figure 2.11. In materials such as GaAs, the band gap is formed by an s-type CB and a p-type VB with orbital angular momentum quantum numbers $l = 0$ and $l = 1$, respectively. Spin-orbit coupling results in a total angular momentum quantum number $j = 3/2$ in the VB. Importantly, this yields heavy hole (hh) and light hole (lh) bands that are degenerate at the VB maximum with magnetic quantum numbers $m_j = \pm 3/2$ and $m_j = \pm 1/2$, respectively. The split-off band with $j = 1/2$ and $m_j = \pm 1/2$ is energetically shifted away from the band gap. The CB minimum is formed by a single band with $j = 1/2$ and $m_j = \pm 1/2$.[51] This band structure is illustrated in Figure 2.11a.

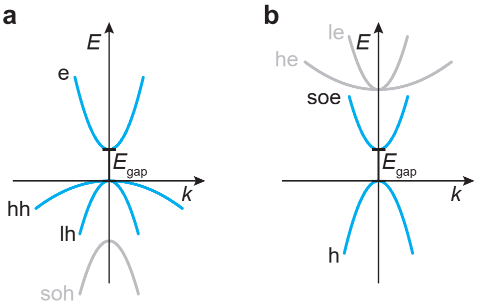

Figure 2.11: Inverted Band Structure of Perovskites. **(a)** Simplified band structure of a conventional II-VI or III-V semiconductor where the band gap is formed by a single CB and degenerate hh/lh VBs. **(b)** In comparison, the band structure of LHPs is inverted, so the band gap is formed by a single VB and a single CB which is the split-off electron band.

Figure 2.11b illustrates the band structure of LHPs. As seen in Figure 2.10b, their CB is p-type ($l = 1$), while the VB is considered s-type ($l = 0$). Once again, spin-orbit coupling requires utilizing the quantum number j. Three aspects shall be highlighted in comparison to the conventional band structure shown in Figure 2.11a: First, there is no degeneracy in the VB, but rather a single band with $j = 1/2$ and $m_j = \pm 1/2$ forming the band gap. Second, the CB minimum is formed by the split-off electron band with $j = 1/2$ and $m_j = \pm 1/2$, while the bands with $j = 3/2$ are at higher energies (with $m_j = \pm 3/2$ corresponding to the heavy electron (he) and $m_j = \pm 1/2$ to the light electron (le)). Therefore, the he/le degeneracy does not influence the transitions close to the band edge. Third, both the single VB and the single CB forming the band gap have relatively low effective masses, as neither hh nor he are involved.[51,139]

The properties discussed so far are related to the intrinsic electronic structure of LHPs. An application field for LHP thin films is photovoltaics, where they are used as sensitizer and absorber layers or in tandem solar cells, using their high charge carrier mobility, tunable band gap, high power conversion efficiency, large-scale and low-cost solution-based fabrication.[26–30,140–143] Another field of applications for LHPs are light-emitting devices, for which rather than thin films, NCs are used, which are introduced in the following.

2.2.2 Lead Halide Perovskite Nanocrystals

A major breakthrough of the perovskite material class was achieved in 2015 with the first synthesis of colloidal LHP nanocrystals (NCs).[31] Since then, mainly nanocubes and nanoplatelets of different sizes and compositions have been studied.[32,144–147] Nanoplatelets are quantum confined only in one dimension, while nanocubes are confined in all three dimensions. Large nanocubes and thick nanoplatelets with sizes much larger than the exciton Bohr diameter of the material (see Subsection 2.1.1), can essentially be considered bulk. The term NC generally refers to a nm-sized particle, whereas QD specifically means a zero-dimensional particle where charge carriers are confined in all three dimensions by the potential of the QD.[53] Note that LHPs have some disadvantages, such as the toxicity of elements and the poor stability of LHP NCs in polar solvents and against moisture. Many research efforts are directed to limit or eliminate these problems, e.g., by studying Pb-free alternatives such as Sn-, Bi-, or Sb-based perovskites, or by investigating alternative ligand chemistry and encapsulation processes.[51,138,148,149]

However, LHP QDs have a significant advantage over conventional QDs. They show excellent emission properties without the need for core/shell systems, which is a result of their high defect tolerance, as discussed in Subsection 2.2.1. Moreover, LHP QDs provide high PLQYs approaching unity, narrow emission linewidths, and excellent tunability of their emission energy.[34,51,138,150] In addition to tuning their emission by the QD size via the quantum size effect (see Subsection 2.1.1), the halide composition serves as an additional tuning parameter.

Gradual anion exchange, e.g., in $CsPbBr_3$ QDs to $CsPbCl_3$ and $CsPbI_3$ QDs, achieves emission across the entire visible spectrum.[33] Even the typically lower PLQY in the blue spectral region of $CsPbBr_3$ nanoplatelets or generally $CsPbCl_3$ NCs, can be strongly enhanced by a simple post-synthetic treatment with $PbBr_2$ or $CdCl_2$, respectively.[146,151] These excellent emission properties of LHP NCs have made them promising for light-emitting applications like LEDs and displays[36–38] or wearable electronics.[39–43]

Additionally, LHP QDs are highly promising for quantum light emission[44–47] and lasing.[48–50] In this context, a unique property of LHPs should be highlighted. As illustrated in Figure 2.11a, conventional II-VI and III-V semiconductors have a hh/lh degeneracy in the VB. Although this degeneracy is lifted by quantum confinement, the resulting energy levels with different effective masses m^*_{hh} and m^*_{lh} lie energetically close. This makes it challenging to selectively excite a specific state due to spectral overlap or thermally induced transitions, and it is difficult to spectrally resolve individual transitions.[152,153] In ensemble measurements, where resolvability is further limited by inhomogeneous broadening, as discussed in Subsection 2.1.2, this is especially problematic. The inverted band structure of LHPs shown in Figure 2.11b avoids these issues, as the band gap is formed by only a single VB and a single CB. Furthermore, both bands have relatively small effective masses, leading to substantial confinement energies in QDs (see Equation 2.2).[51] This results in better resolvability of individual transitions and makes LHP QDs an ideal model system for studying confinement effects.

Most initial studies on LHP NCs have focused on relatively large nanocubes without significant confinement.[154–158] Furthermore, the terminology used in literature is not always consistent. The degree of confinement in QDs is often described as weak or strong without referring to the distinct weak and strong confinement regimes introduced in Subsection 2.1.1. Instead, these terms are often used in relation to the clarity with which distinct absorption resonances are observed. However, this resolvability is limited in QD ensembles by inhomogeneous broadening, as discussed in Subsection 2.1.2. In this thesis, weak and strong confinement always refers to the specific confinement regimes discussed in Subsection 2.1.1.

2.2.3 Optical Gain in Lead Halide Perovskite Quantum Dots

Another active field of research on LHP QDs focuses on light amplification toward lasing applications.[48–50] LHP QDs combine the general advantages of QDs to reach optical gain easier compared to bulk systems (see Subsection 2.1.3) with their unique properties, such as high defect tolerance, flexible tunability of their emission energy via the halide composition, and inverted band structure (see Subsection 2.2.1). Their well-separated energy levels can provide room-temperature stability of optical gain states.[25] However, the lifetime τ_{Auger} associated with non-radiative Auger recombination in LHP QDs is reported to show a volume scaling of $\tau_{\text{Auger}} = \gamma \cdot V$ with $\gamma \approx 0.06\,\text{ps}/\text{nm}^3$. This is much smaller than the $\gamma \approx 1\,\text{ps}/\text{nm}^3$ for II-VI semiconductor QDs (see Subsection 2.1.2). Hence, Auger lifetimes of LHP QDs are expected to be considerably faster than in conventional core-only QDs, which could potentially hinder optical gain.[25,159]

Nevertheless, optical gain with LHP QDs was already reported in 2015,[160,161] and has since been used in combination with various resonators to achieve lasing.[48–50,162] However, the underlying optical gain mechanism in LHP QDs has been attributed to different origins: Although biexcitonic gain might be expected,[114,161,163,164] as is typically observed in conventional core-only QDs (see Subsection 2.1.3), single-exciton gain[160,165,166] and trion gain[167] have also been reported. Knowing the origin of the underlying optical gain is key for the targeted optimization of the light amplification properties of LHP QDs. This is exemplified by the significantly reduced optical gain threshold discussed in Figure 2.8 for conventional QDs, which is achieved by replacing the biexcitonic gain mechanism with single-exciton gain through type-II core/shell engineering. Furthermore, preferably QD ensembles without substantial inhomogeneous broadening should be studied to draw general conclusions.

Amplified Spontaneous Emission

For applications, it is crucial not only to have optical gain but also to achieve usable light amplification. This requires the optical gain to overcome the losses in the system.[112,113] While prolonging gain lifetimes requires limiting the competition with non-radiative processes, additional losses like through scattering in the material have to be overcome as well. A gain g and loss coefficient α_{loss} can be defined that yield the net optical gain coefficient G through[168]

$$G = g - \alpha_{\text{loss}}. \tag{2.13}$$

A common approach to test whether an ensemble of QDs can generate net light amplification ($G > 0$) is to measure amplified spontaneous emission (ASE). Figure 2.12a shows the typical measurement principle of ASE. The QDs are deposited on a substrate and illuminated by a rectangular focus spot. The light emitted along this rectangular stripe is collected and analyzed.

The emission properties varying under different excitation conditions are illustrated in Figure 2.12b. QDs that are not excited remain in their ground state (gray dots). At low excitation fluences, only a few of the illuminated QDs are actually excited (green dots) as shown in (i). The edge-emitted light is spontaneous emission, which is *per se* not directed. As the excitation fluence is increased (ii), more QDs are excited, resulting in a higher intensity of the detected spontaneous emission. For an even higher fluence (above the ASE threshold) shown in (iii), QDs are also excited to an optical gain state. A spontaneously emitted photon can stimulate emission from a QD in the gain state. If enough QDs are excited to this gain

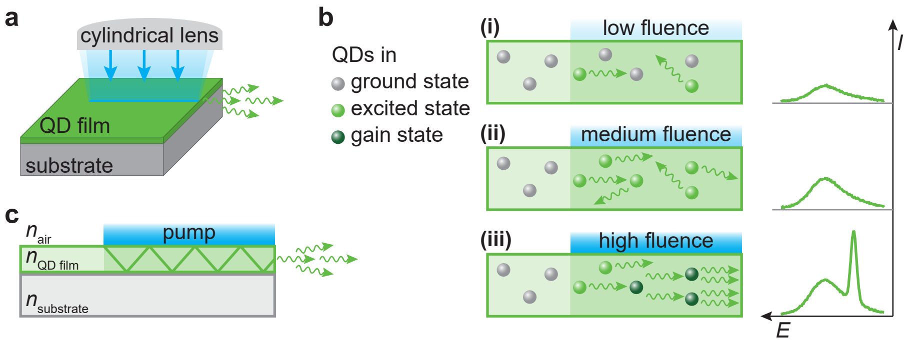

Figure 2.12: Principle of Amplified Spontaneous Emission. **(a)** Illustration of the measurement principle of ASE with the QD film being excited by a rectangular focus spot created by a cylindrical lens, while the edge-emitted light is collected in a 90° angle. **(b)** Schematic illustration of QDs in the film and their emission properties. The amount of spontaneous emission increases with excitation fluence from **(i)** to **(ii)**, and for high fluences above the ASE threshold in **(iii)**, ASE is detected additionally. **(c)** Waveguiding effect in the illuminated QD film that has a higher refractive index ($n_{\text{QD film}}$) than the surrounding air (n_{air}) and substrate ($n_{\text{substrate}}$).

state, stimulated emission can happen over and over again along the illuminated stripe. This cascade of photons is detected at the edge as ASE.

A property of the QD film that strongly supports ASE is its ability to act as a waveguide, illustrated in Figure 2.12c.[112,169] For total internal reflection to occur in the QD film, it must have a higher refractive index ($n_{\text{QD film}}$) than the surrounding media, here air (n_{air}) and the substrate ($n_{\text{substrate}}$), so that $n_{\text{QD film}} > n_{\text{air}}, n_{\text{substrate}}$. This waveguiding effect is more pronounced at smooth interfaces. Although ASE is typically regarded as a first indication whether a material is suitable for lasing, those two processes should not be confused. In contrast to actual lasing, ASE does not involve a cavity and does not produce temporally coherent light.[84,110]

In this thesis, the energy landscape of novel spherical LHP QDs is discussed in Chapter 4, where they are assigned to the weak confinement regime, and a detailed analysis of their intriguing excited-state properties dominated by biexcitons is provided. Furthermore, the potential of spherical $CsPbBr_3$ QDs for light amplification is tested, and the origin of the underlying optical gain is unambiguously attributed to biexcitons in Chapter 5. Before that, the experimental background is presented in Chapter 3, briefly introducing the material synthesis and the spectroscopic methods used to study the LHP QDs in detail.

3

Experimental Background

Monodisperse spherical LHP QDs are investigated in Chapter 4 and Chapter 5. The synthesis that provides these high quality QDs is briefly introduced in Section 3.1, together with electron microscopy, which is used for their structural verification. The main part of this chapter presents the spectroscopic methods used to study their optical properties. First, a concise description of steady-state absorption and photoluminescence (PL) spectroscopy is provided in Section 3.2, which serve as initial characterization tools of the time-integrated optical properties of the QDs. Second, transient absorption (TA) spectroscopy is introduced in Section 3.3, including the working principle of the amplifier system, which provides intense short laser pulses required to investigate the excited-state dynamics of the QDs. Finally, the setup for amplified spontaneous emission (ASE) studies is presented in Section 3.4, including the variable stripe length (VSL) method and the analysis used to extract light amplification parameters, such as the optical gain threshold and the net optical gain coefficient.

3.1 Synthesis of Spherical Perovskite Quantum Dots

The spherical LHP QDs were synthesized by Dr. Quinten Akkerman using his synthesis detailed in Reference 54. In the following, a concise overview of the synthesis is provided, together with high-angle annular dark-field scanning transmission electron microscopy (HAADF-STEM).

$CsPbBr_3$ Quantum Dot Synthesis

The most common synthesis method for colloidal LHP NCs is the hot-injection technique. In this approach, the precursors are individually heated to ~140–200 °C, depending on the desired NC size, before being rapidly mixed. Since the whole reaction is completed within a few seconds,[31] nucleation and growth occur simultaneously, leading to a relatively broad size distribution of the resulting NCs.[54] In contrast, the synthesis method used here is carried out under ambient conditions, with nucleation and growth separated in time. The ligand-controlled growth yields monodisperse spherical QDs with well-defined sizes. The reaction mechanism for such spherical $CsPbBr_3$ QDs can be described as[54]

$$\begin{aligned} 3\,\mathrm{PbBr_2[TOPO]} + 2\,\mathrm{Cs\text{-}DOPA} &\rightleftharpoons 2\,\mathrm{Cs[PbBr_3]} + \mathrm{PbDOPA_2} + \mathrm{TOPO} \\ &\longrightarrow 2\,\mathrm{CsPbBr_3\ QDs}, \end{aligned} \tag{3.1}$$

with the phospho-ligands trioctylphosphineoxide (TOPO) and diisooctylphosphonic acid (DOPA). The synthesis is conducted in the non-polar solvent hexane, to which the $PbBr_2[TOPO]$ precursor is added. To ensure a homogeneous mixture at all times, the solution is stirred continuously. When the Cs-DOPA precursor is added, the reaction starts and $Cs[PbBr_3]$ monomers are formed. At a certain monomer concentration, nucleation begins. To get nucleation started in the whole solution at the same point in time, the entire amount of Cs-DOPA is added quickly under vigorous stirring. Nucleation again lowers the concentration of monomers, starting the growth phase, where the $Cs[PbBr_3]$ intermediate is continuously converted into $CsPbBr_3$ QDs. After a few minutes, when the growth phase is finished, lecithin or didodecyldimethylammonium bromide (DDAB) ligands are added, which bind strongly to the surface of the $CsPbBr_3$ QDs. In the following washing step, an antisolvent (aceton or ethanol) is added, in which the QDs are not soluble, but the excess ligands and precursors are. Centrifuging separates the QDs as the sediment from the supernatant, which is discarded. The QDs are redispersed in hexane or octane and prepared for the intended measurements. A summary of the used chemicals, preparation of the stock solutions, and synthesis details can be found in the Appendix.

The size of the QDs can be tuned by the amount of TOPO. To change the composition, Br^- can be fully or partially exchanged to, e.g. Cl^- by adding $ZnCl_2$-TOPO after the growth and before the washing step.[170] Moreover, the inorganic Cs^+ can be replaced by organic cations, such as formamidinium FA^+.[54]

Structural Verification via Scanning Transmission Electron Microscopy

To check the shape and size of the perovskite QDs after the synthesis, a simple light microscope is not sufficient as the nm-sized QDs are much smaller than the wavelength of visible light. To increase the resolution, instead of photons, electrons are used, which have a de Broglie wavelength λ_{dB} given by

$$\lambda_{\mathrm{dB}} = \frac{h}{mv} = \frac{h}{\sqrt{2meU}}, \tag{3.2}$$

with the electron mass m and the acceleration voltage U.[171] A probe corrected *FEI Titan Themis* scanning transmission electron microscopy (STEM) setup was used in high-angle annular dark-field (HAADF) mode with $U = 300\,\mathrm{kV}$, resulting in $\lambda_{\mathrm{dB}} \approx 2\,\mathrm{pm}$, which is proportional to the resolution.[172] For this measurement, a dilute dispersion of the QDs was dropcasted onto a carbon-coated copper grid. HAADF-STEM utilizes a focused electron beam that is scanned across the sample. The position-dependent intensity of transmitted electrons, which are inelastically scattered at large angles by atom cores, is detected using an annular detector. The resulting contrast variations provide an image of the sample and can also reveal its atomic structure.[173]

3.2 Steady-State Spectroscopy as First Optical Characterization Tool

The easiest way to study the optical properties of QDs is in the steady state. Here, data are acquired in a time-integrated way over a duration of the order of ms or s. The sample can be illuminated continuously; hence, pulsed light sources are not necessary and lamps can be used for excitation. In the following, steady-state absorption and PL spectroscopy is briefly introduced, including the commercially available tabletop devices used.

3.2.1 Steady-State Absorption Spectroscopy

The steady-state absorption was measured with the QDs in a dilute colloidal dispersion in a quartz cuvette. Changes in transmission are attributed solely to absorption, as scattering and reflection are typically neglected for dilute QD dispersions. A *Cary 60 UV-Vis* spectrophotometer equipped with an 80 Hz xenon flash lamp was used together with the provided software *Scan* from *Agilent Technologies.* The white light provides spectral resolution but is not used directly. Instead, it passes through a Czerny-Turner monochromator, where a grating disperses the white light and only a narrow wavelength band exits through a slit. By rotating the grating it can sweep through the different wavelengths in a broad range of 190–1100 nm. The light is focused on the sample to an area of ~1.5 × 1 mm^2 and the transmitted intensity is detected by a silicon diode detector.

The transmittance T represents the relative change in intensity through the sample. It is related to the material-specific absorption coefficient α, the sample thickness, here defined by the path length L of the cuvette, and the absorbance or optical density OD via[58]

$$T = \frac{I}{I_0} = e^{-\alpha \cdot L} = 10^{-OD}. \tag{3.3}$$

Note that the wavelength dependence of T and related parameters is omitted for clarity. I is the intensity transmitted by the sample, while I_0 represents the intensity transmitted by an identical cuvette filled only with the solvent. Therefore, the determined OD reflects only the absorption of the QDs themselves. Both intensities are corrected for fluctuations in the intensity of the lamp. OD can be related to the extinction coefficient ϵ, the sample thickness L, and the sample concentration c in the so-called Beer-Lambert law:[174]

$$OD = -\log_{10}\left(\frac{I}{I_0}\right) = \epsilon \cdot L \cdot c. \tag{3.4}$$

A specific OD of the QD dispersion in a cuvette with fixed path length was achieved by adjusting c accordingly. Typically, an $OD = 0.2$ at 400 nm was chosen for a path length of $L = 2\,\mathrm{mm}$. This value represents a good balance between ensuring a sufficiently high signal intensity for both absorption-based and PL measurements, while minimizing reabsorption and scattering. Moreover, maintaining a consistent OD across all samples ensures comparability between different samples.

The size of the $\mathrm{CsPbBr_3}$ QDs investigated in this thesis can be determined from the absorption spectrum. Due to the quantum size effect (see Subsection 2.1.1), the spectral position of the first absorption peak is correlated to the QD diameter. The sizing curve from Reference 54 is used, which is derived from a dataset of numerous QDs of different sizes, with their diameters determined through STEM analysis. The correlation between the first absorption peak position and the QD diameter is reproduced by a polynomial function, which serves as the sizing curve.[54]

3.2.2 Steady-State Photoluminescence Spectroscopy

Once the absorption of a sample is known, the next step is typically to investigate its luminescence upon photoexcitation. For this thesis, the steady-state PL was acquired with a *Fluorolog-3 FL3-22* spectrofluorometer from *Horiba Jobin Yvon GmbH* with the designated software *FluorEssence*. It is equipped with a 450 W xenon arc lamp from which the desired excitation wavelength is selected with a double-grating monochromator. The light emitted from the sample is collected in a 90° or a 22.5° angle to the excitation path, in the so-called right-angle (RA) or front-face (FF) configuration, respectively. The latter is more suitable for strongly scattering samples or for samples with a large *OD* and strong reabsorption. Here, these effects were minimized because the QDs were measured in a stable colloidal dispersion in a cuvette with 2 mm path length with an $OD \approx 0.2$ at the excitation wavelength at 400 nm. Therefore, there was no difference in PL spectra obtained in the RA or FF configuration. The emitted light passes through another double-grating monochromator, which disperses the light and sweeps through the different wavelengths, which are subsequently detected by a *R928P* photomultiplier tube.

Conversion Between Wavelength and Energy

As described above, the PL intensity is measured as a function of wavelength $I(\lambda)$. When converting it into a function of energy $I(E)$, one has to consider the inverse relation between wavelength and energy via $\lambda = \frac{hc}{E}$. An equal spacing in wavelength does not correspond to an equal spacing in energy. Therefore, it is not correct to simply convert the x-axis of the PL spectrum from λ to E, but the intensity also has to be adjusted. This becomes clear when considering energy conservation:

$$I(\lambda)\,\mathrm{d}\lambda = I(E)\,\mathrm{d}E. \tag{3.5}$$

$I(\lambda)$ is correctly transformed to $I(E)$ via the so-called Jacobian transformation with the factor $\frac{hc}{E^2}$:[175]

$$I(E) = I(\lambda)\frac{\mathrm{d}\lambda}{\mathrm{d}E} = -I(\lambda)\frac{hc}{E^2}. \tag{3.6}$$

The minus sign indicates the different directions of integration in the wavelength and energy domains and is not further relevant. After the PL spectrum $I(\lambda)$ is converted to $I(E)$ accordingly, it can be used for, e.g., determining an energy shift or fitting Gaussian peaks. Note that this procedure is not necessary for absorption measurements as the transmittance T is the ratio of two intensities (see Equation 3.3), hence the Jacobian factor cancels.[176]

3.3 Transient Absorption Spectroscopy

Transient absorption (TA) spectroscopy is a pump-probe technique that monitors changes in the absorption of the ground and an excited state of a sample. Ultra-short laser pulses of ~100 fs are used to obtain information on a sub-ps time scale. In the following, a brief summary on the amplification and wavelength tuning of such laser pulses is provided before the TA technique itself is described in detail.

3.3.1 Amplification of Ultra-Short Laser Pulses

The ultra-short pulse length of laser pulses provides a high temporal resolution for TA measurements. A high laser power is often required to utilize various nonlinear processes, such as changing the laser wavelength (see Subsection 3.3.2) or studying the nonlinear behavior of a sample (see Chapter 5). To generate such ultra-short and intense laser pulses, a *Libra-HE+* Ti:Sapphire amplifier system from *Coherent* was used, that provides 800 nm laser pulses with a pulse length $\tau_{\text{pulse}} \approx 100\,\text{fs}$, an average power $P_{\text{avg}} \approx 5\,\text{W}$, and a repetition rate $f_{\text{rep}} = 1\,\text{kHz}$. The main components are schematically illustrated in Figure 3.1.

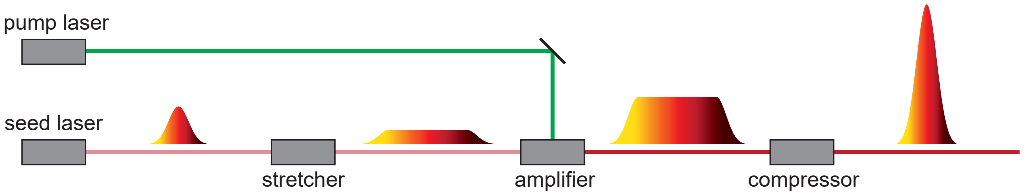

Figure 3.1: Amplifier System. The seed laser pulses (~100 fs, 800 nm) are temporally elongated by a stretcher to ~ps, the intensity is increased by an amplifier, and the laser pulses again narrowed by a compressor to ~100 fs. The Ti:Sapphire crystal as the gain medium in the amplifier cavity is pumped by a pump laser (~120 ns, 527 nm).

The starting point is a *Vitesse* seed laser. This Ti:Sapphire oscillator (pumped by a 532 nm continuous wave *Verdi* diode laser) already produces 800 nm laser pulses of ~100 fs at a repetition rate of 80 MHz but with an average power of only ~300 mW. Directly amplifying these ultra-short laser pulses risks damaging the gain medium due to self-focusing.[177] Instead, chirped-pulse amplification (CPA) is used.[178] First, the ultra-short pulses are temporally elongated in a grating-based so-called stretcher, which introduces a positive chirp resulting in ~ps pulses. This reduces the peak power P_{peak} according to

$$P_{\text{peak}} = \frac{E_{\text{pulse}}}{\tau_{\text{pulse}}}, \tag{3.7}$$

with the pulse energy E_{pulse} that remains constant during the stretching process. The following regenerative amplifier consists of a Ti:Sapphire crystal (see Subsection 2.1.3) positioned in a cavity and pumped by a 527 nm *Evolution* diode laser with a repetition rate of 1 kHz and a pulse length of ~120 ns. In- and out-coupling, as well as the number of round trips of the pulses in the cavity is controlled by electro-optic switches called Pockels cells. The first Pockels cell couples laser pulses in the cavity at a rate of 1 kHz, matching the repetition rate of the pump laser. The pulses get amplified by the gain medium in numerous round-trips and are finally coupled out by the second Pockels cell.[179] The amplified pulses with $f_{\text{rep}} = 1\,\text{kHz}$ are temporally compressed back to ~100 fs by a so-called compressor, which introduces a negative chirp and increases P_{peak}, following the reverse process of the stretcher.

Looking at the initial and final parameters of the laser beam underlines the importance of correctly distinguishing different parameters. Ultimately, P_{avg} increased from ~300 mW to ~5 W by a factor of ~17, while f_{rep} decreased from 80 MHz to 1 kHz by a factor of $8 \cdot 10^4$. A parameter that includes changes of both quantities is the pulse energy

$$E_{\mathrm{pulse}} = \frac{P_{\mathrm{avg}}}{f_{\mathrm{rep}}}. \tag{3.8}$$

The initial $E_{\mathrm{pulse}} \approx 4$ nJ is amplified to ~5 mJ by a factor of ~10^6. P_{peak} is amplified by the same factor from ~40 kW to ~50 GW.

3.3.2 Tuning the Wavelength of Laser Pulses

To achieve a spectral resolution for TA measurements in the visible range, white light is necessary for the probe beam. Furthermore, to excite the LHP QDs under investigation, wavelengths of $\lambda \lesssim 500$ nm are required. In the following, the processes used to create these additional wavelengths from the 800 nm output of the amplifier system (as discussed in Subsection 3.3.1) are briefly described and illustrated in Figure 3.2. They all rely on the interaction of ultra-short and intense laser pulses with nonlinear media. The polarization $P(t)$ of such a medium induced by a strong optical field depends nonlinearly on the electric field $E(t)$ according to

$$P(t) = \varepsilon_0 \chi^{(1)} E(t) + \varepsilon_0 \chi^{(2)} E(t)^2 + \varepsilon_0 \chi^{(3)} E(t)^3 + ..., \tag{3.9}$$

with the vacuum permittivity ε_0 and the linear, second-, and third-order nonlinear optical susceptibilities $\chi^{(1)}$, $\chi^{(2)}$, and $\chi^{(3)}$, respectively. For media with inversion symmetry the even-order nonlinear susceptibilities vanish, resulting in a dominant nonlinear contribution from $\chi^{(3)}$.[177,179]

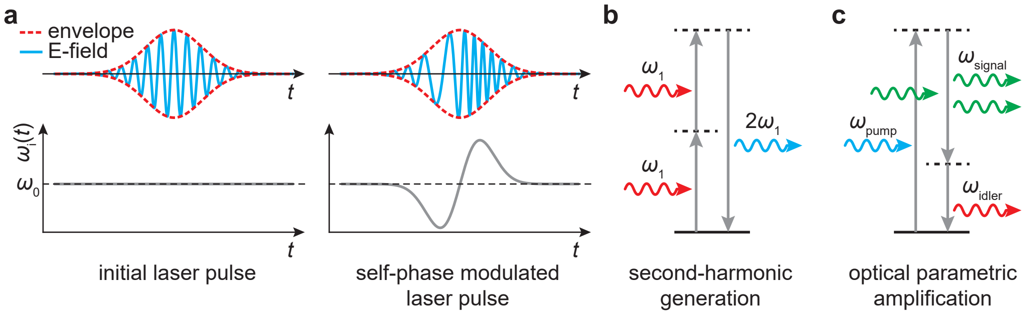

Figure 3.2: Nonlinear Processes. (a) Illustration of self-phase modulation in a Gaussian-shaped laser pulse by a material with $n_2 > 0$ creating additional frequencies to the initial frequency ω_0 represented by the instantaneous frequency $\omega_i(t)$. Level scheme illustrating **(b)** second-harmonic generation and **(c)** optical parametric amplification.

White-Light Generation

An example of a third-order nonlinear process is the optical Kerr effect, which describes the intensity dependence of the refractive index $n(I)$ as

$$n(I) = n_0 + n_2 I, \tag{3.10}$$

with the initial refractive index n_0 and the optical Kerr coefficient n_2. For white-light generation in the used TA setup, a $\mathrm{CaF_2}$ crystal is used, for which the main contribution to white-light generation is self-phase modulation, which is illustrated in Figure 3.2a. Here, an incoming optical pulse experiences the intensity-dependent $n(I)$, resulting in a variation of the phase $\varphi(t) \propto n_2 I(t)$. This influences the instantaneous frequency $\omega_\mathrm{i}(t)$ of the pulse, which is given by

$$\omega_\mathrm{i}(t) = \omega_0 + \frac{\mathrm{d}}{\mathrm{d}t}\varphi(t). \tag{3.11}$$

Due to the varying phase, additional frequencies are introduced around the initial frequency ω_0, creating a chirp in the pulse.[177,180] The resulting optical pulse contains a range of frequencies that, in the case of $\mathrm{CaF_2}$, covers the visible spectral range even extending into the ultraviolet (UV).

Second-Harmonic Generation

Materials without an inversion symmetry have $\chi^{(2)} \neq 0$ (compare with Equation 3.9) and can therefore show second-order nonlinear properties. This is necessary for second-harmonic generation (SHG), where the frequency of a laser pulse is doubled, as illustrated in Figure 3.2b. For this thesis, this process was used to generate 400 nm from the 800 nm provided by the amplifier system, by utilizing a barium borate (BBO) crystal.

An incoming plane wave with angular frequency ω can be written as

$$E(t) = E_0 e^{-i\omega t} + E_0^* e^{i\omega t}, \tag{3.12}$$

with the amplitude E_0 and its complex conjugate E_0^*. The interaction of this incoming electric field with a material with $\chi^{(2)} \neq 0$ can be described by

$$P^{(2)}(t) = \varepsilon_0 \chi^{(2)} E(t)^2 = \varepsilon_0 \chi^{(2)} (E_0^2 e^{-i2\omega t} + E_0^{*2} e^{i2\omega t} + 2E_0 E_0^*). \tag{3.13}$$

While the last term on the right side does not contribute to outgoing radiation, the first two terms have a contribution at the frequency 2ω, which is exactly the desired second-harmonic of the incoming frequency ω.[177]

The Optical Parametric Amplifier

The *OPerA Solo* optical parametric amplifier (OPA) from *Coherent* used for this thesis can generate light in a broad spectral range from ~300 nm up to 12 µm by utilizing several nonlinear processes. As the name suggests, the main process in an OPA is optical parametric amplification, which is illustrated in Figure 3.2c. Two light beams interacting in a $\chi^{(2)} \neq 0$ medium are required: one high-intensity pump beam with ω_pump and another so-called signal beam with ω_signal. While the intensity of the pump beam gets decreased, the intensity of the signal beam is amplified and another, so-called idler beam with ω_idler is created. The three beams follow the relation $\omega_\text{pump} = \omega_\text{signal} + \omega_\text{idler}$. The *OPerA Solo* uses the 800 nm output of the *Libra-HE+* amplifier system as pump beam. A fraction of the pump is used for white-light generation in a sapphire crystal, from which the desired ω_signal is selected.

Several other second-order nonlinear processes are used for further frequency mixing, such as the above mentioned SHG as well as sum-frequency generation (SFG) and difference-frequency generation (DFG). In analogy to SHG described in Equation 3.13, one can consider the case of two incoming plane waves with different angular frequencies ω_1 and ω_2. Then, the resulting outgoing radiation contains, besides the second-harmonic terms with contributions at $2\omega_1$ and $2\omega_2$, additional mixed frequency terms with $\omega_1 + \omega_2$ and $\omega_1 - \omega_2$, which correspond to SFG and DFG, respectively. Note that all the mentioned nonlinear processes require phase matching to be efficient. This means that the wave vector mismatch Δk should ideally be zero, which can be realized in birefringent materials such as BBO crystals. For SFG as an example, the wave vector mismatch is given by $\Delta k = k_1 + k_2 - k_3$, with the wave vectors of the incoming light k_1 and k_2, and the generated wave vector k_3.[177,181]

3.3.3 A Tool to Study the Excited State

After introducing the amplifier system and the nonlinear processes utilized to create the desired wavelengths, TA spectroscopy is discussed next. It is a pump-probe technique and, therefore, relies on two laser beams interacting with the sample. The pump beam excites the sample to a certain state depending on the excitation wavelength, while the white-light probe beam is used to measure the absorption of the sample with (OD_pump) and without prior pumping ($OD_\text{no pump}$), as illustrated in Figure 3.3. The signal of interest is the change in absorption of the ground and the excited state ΔOD, given by

$$\Delta OD = OD_\text{pump} - OD_\text{no pump}. \tag{3.14}$$

Although the spectral and temporal dependence of ΔOD is crucial to studying the excited state of a sample, it is omitted in the equations for clarity.

As discussed in Subsection 3.2.1, absorption is not directly measured, but rather the transmitted intensity. The actual parameters recorded here are the spectrally-resolved intensities

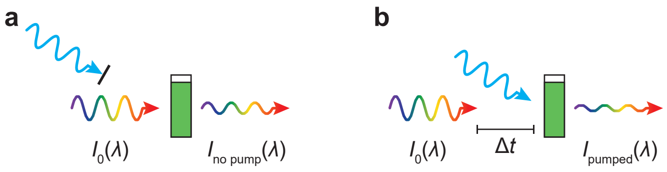

Figure 3.3: Transient Absorption Spectroscopy Principle. Illustration of the TA technique using a white-light probe beam of intensity $I_0(\lambda)$ illuminating the sample. **(a)** Without a prior pump pulse, the transmitted intensity is $I_{\text{no pump}}(\lambda)$. **(b)** A pump pulse (blue) excites the sample and after a delay time Δt, the transmitted white-light intensity is $I_{\text{pump}}(\lambda)$.

of the probe beam after the sample with and without prior pumping I_{pump} and $I_{\text{no pump}}$, respectively. Following the relation between intensity and OD introduced in Equation 3.3, ΔOD can be expressed as

$$\Delta OD = -\log_{10}\left(\frac{I_{\text{pump}}}{I_0}\right) - \left(-\log_{10}\left(\frac{I_{\text{no pump}}}{I_0}\right)\right) = \log_{10}\left(\frac{I_{\text{no pump}}}{I_{\text{pump}}}\right). \tag{3.15}$$

Note that the light intensity I_0 before interacting with the sample cancels out. To obtain information on the temporal dynamics, a temporal delay Δt between pump and probe pulses is introduced and the ΔOD signal is repeatedly measured for different time delays. The temporal resolution is limited by the pulse length.

A TA measurement can contain a variety of information and should first of all be compared to the linear absorption spectrum (see Subsection 3.2.1), which corresponds to $OD_{\text{no pump}}$ in Equation 3.14. A fundamental process when pumping a bulk semiconductor is the change in absorption coefficient $\Delta\alpha$ induced by the density of electrons in the CB f_{e} and of holes in the VB f_{h}. As the sample thickness is constant throughout the measurement, $\Delta\alpha \propto \Delta OD$ (see Equation 3.3). The initial absorption coefficient before pumping is $\alpha_{\text{no pump}}$. Due to so-called phase-space filling,[62] the absorption into the excited state is reduced if either f_{e} or f_{h} is nonzero, i.e., if electrons in the CB or holes in the VB, respectively, 'block' some of the transitions. It is described by $\alpha_{\text{pump}} = \alpha_{\text{no pump}}(1 - f_{\text{e}})(1 - f_{\text{h}})$. Furthermore, stimulated emission characterized by $e = \alpha_{\text{no pump}} f_{\text{e}} f_{\text{h}}$ becomes possible if both f_{e} and f_{h} are nonzero. This illustrates that for an emission process both an electron in an excited state and a hole (a missing electron in the ground state) must be available. $\Delta\alpha$ can be related to $\alpha_{\text{no pump}}$ and $f_{\text{e,h}}$ via

$$\begin{aligned}\Delta\alpha &= (\alpha_{\text{pump}} - e) - \alpha_{\text{no pump}} = \\ &= \alpha_{\text{no pump}}(1 - f_{\text{e}})(1 - f_{\text{h}}) - \alpha_{\text{no pump}} f_{\text{e}} f_{\text{h}} - \alpha_{\text{no pump}} = \\ &= -\alpha_{\text{no pump}}(f_{\text{e}} + f_{\text{h}}).\end{aligned} \tag{3.16}$$

Note that for $f_{\text{e,h}} \neq 0$, both α_{pump} and e contribute to a negative $\Delta\alpha$, i.e., bleaching in the TA signal. All parameters discussed above are wavelength and delay-time dependent, although this is not included to keep Equation 3.16 legible. A variety of processes can be studied using TA spectroscopy, as discussed elsewhere.[91,104,182,183] The temporal resolution of this technique further enhances its versatility, enabling the resolution of temporally varying signals, e.g., induced by coherent phonons.[158,184,185]

The Transient Absorption Setup

A custom-built TA setup from *Newport* was utilized for this thesis. A sketch of the setup is shown in Figure 3.4 illustrating the simplified beam path and the main optical components. The *Libra-HE+* Ti:Sapphire amplifier system from *Coherent*, as detailed in Subsection 3.3.1, was used as the light source for both pump and probe beam. For the pump, the 800 nm wavelength of the ultra-fast laser pulses were adjusted to 400 nm using a BBO crystal via SHG (see Subsection 3.3.2) after which any remaining 800 nm light is blocked by a short-pass excitation filter. Alternatively, to match the first absorption peak of the investigated QDs, a wavelength of ~500 nm was generated via SFG using an OPA (see Subsection 3.3.2).

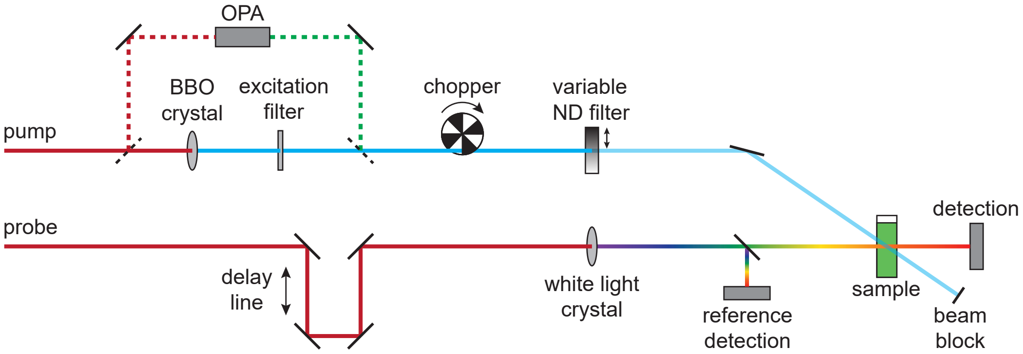

Figure 3.4: Transient Absorption Setup. Sketch of the transient absorption setup showing a simplified beam path of pump and probe beams including the relevant optical components. The dashed lines and mirrors represent an alternative beam path, where the pump is diverted to an optical parametric amplifier (OPA).

To alternately measure the absorption of the ground and excited state of the sample (OD_{pump} and $OD_{\text{no pump}}$, respectively), every second pump beam is blocked by a mechanical chopper, resulting in a halved repetition rate of the pump beam of 0.5 kHz. The pulse energy is adjusted by a variable neutral density (ND) filter and subsequently measured by a *919E-20U-10-20K* photodiode pulse energy detector from *Newport*. After that, the pump beam is guided onto the sample at a slight angle so that any transmitted pump light can be absorbed by a beam block. The size of the pump beam spot at the sample position was determined by a *WincamD-UCD12-1310* beam profiler from *dataRay* to have a diameter of around 650 µm, resulting in an area of around $3.3 \cdot 10^{-3}$ cm^2. To ensure that the entire probed region is indeed pumped, the spot size illuminated by the pump beam is larger than that of the probe beam, the path of which is described in the following.

After the amplifier system, a beam splitter diverts a small portion of the laser light to serve as the probe beam. Next, it passes through a delay line, which varies the path length of the beam to achieve the temporal delay Δt between the pump and probe pulses. To achieve spectral resolution, the 800 nm beam passes through a CaF_2 crystal generating white light (detailed in Subsection 3.3.2) that covers the entire visible spectrum and even reaches into the UV. The probe illuminates the sample and the transmitted light is subsequently detected by a *MS260i* spectrometer from *Newport* and a charge-coupled device (CCD) camera. To account for pulse-to-pulse fluctuations in the probe beam, half of it is diverted by a beam splitter before the sample and is used as a reference beam, detected by the same devices. The white-light probe pulses are slightly chirped due to self-phase modulation and dispersion in the media they pass through, such as the CaF_2 crystal and beam splitter, causing the lower energy components to arrive first. This effect is qualitatively compensated for by fitting a rational function to the signal onset in the two-dimensional TA dataset, ensuring a consistent time zero across all detected wavelengths.

Polarization-Dependent Measurements

The setup shown in Figure 3.4 can be easily modified for polarization-dependent measurements, where the pump and probe beams are circularly polarized, either with the same (co-polarized) or the opposite circular polarization (counter-polarized). The output of the amplifier system and hence the pump beam is already linearly polarized. To ensure the linear polarization of the white-light probe beam, a Glan-Thompson polarizing prism can be used. The linear polarization of the beams is converted to circular polarization by placing $\lambda/4$ wave plates in the respective beam paths right in front of the sample. An *AQWP05M-600* and a superachromatic *SAQWP05M-700* $\lambda/4$ wave plate from *Thorlabs* are used for the pump and probe beams, respectively.

Sample Preparation

For the TA studies in this thesis, the LHP QDs were prepared in two ways: either dispersed in a solution or deposited on a transparent substrate. The former was used whenever possible, as a stable colloidal dispersion naturally ensures sample homogeneity. Upon high-power pumping, the dispersion was stirred to prevent photo-charging of the sample. A quartz cuvette with an optical path length of 2 mm was used and the sample was diluted to achieve an $OD = 0.2$ at the respective pump wavelength (see Subsection 3.2.1).

To study the QDs at low temperature, the sample has to be cooled down by a cryostat. Here, a closed cycle helium cryostat from *Advanced Research Systems* was used that was controlled by a *Model 335* cryogenic temperature controller from *Lake Shore Cryotronics*. For this purpose, the QDs can no longer be in solution but must be deposited on a transparent substrate. Therefore, the colloidal dispersion was dropcasted onto a sapphire substrate. Note that the resulting film of QDs should be homogeneous to minimize scattering and to make different sample spots across the substrate comparable. Selecting a specific OD is challenging, as variations in film thickness directly affect the OD (see Equation 3.4). Additionally, the film has to be thin enough to allow transmission of the probe beam.

Determining the Excitation Density

As described above, the pulse energy E_{pulse} of the pump beam is measured directly in front of the sample. Upon passing through the sample, some pump photons are absorbed, causing the beam intensity to decrease exponentially with the sample thickness following Equation 3.3. Hence, the pulse energy reaching the backside of the sample is lower than that at the front. For the typically used $OD = 0.2$ at the excitation wavelength, this results in a transmission $T = 10^{-OD} \approx 0.63$. This can be accounted for by considering a spatially averaged $E_{\text{pulse,avg}}$ across the sample with a path length L, as shown in Equation 3.17. The deviation between the initial $E_{\text{pulse},0}$ and $E_{\text{pulse,avg}}$ becomes more pronounced for larger OD values of the sample.[186,187] In the case of $OD = 0.2$, this results in a change of 20 %.

$$\begin{aligned} E_{\text{pulse,avg}} &= \frac{1}{L}\int_0^L E_{\text{pulse}}(z)\,\mathrm{d}z = \frac{1}{L}\int_0^L E_{\text{pulse},0}\cdot e^{-OD\cdot\log_e(10)\cdot z/L}\,\mathrm{d}z = \\ &= \frac{E_{\text{pulse},0}}{OD\cdot\log_e(10)}\cdot\left(1-e^{-OD\cdot\log_e(10)}\right) \overset{OD=0.2}{\approx} 0.8\cdot E_{\text{pulse},0} \end{aligned} \tag{3.17}$$

However, the value of the pulse energy is of limited use as it does not indicate how many photons are actually absorbed. The number of photons absorbed per QD in an ensemble of QDs follows Poisson distribution (see Equation 2.8).[90] Therefore, the probability $P(\langle N\rangle, N \neq 0)$ of having no exciton in a QD is given by

$$P(\langle N\rangle, N \neq 0) = 1 - P(\langle N\rangle, 0) = 1 - e^{-\langle N\rangle}. \tag{3.18}$$

$\langle N\rangle$ can be further related to the spatially-averaged number of photons per pulse per area j_{avg} and the absorption cross-section σ_{abs} at the excitation wavelength via[117]

$$\langle N\rangle = j_{\text{avg}}\cdot\sigma_{\text{abs}} = \frac{E_{\text{pulse,avg}}}{A_{\text{spot}}\cdot {}^{hc}/_{\lambda}}\cdot\sigma_{\text{abs}}, \tag{3.19}$$

with the excitation wavelength λ and the illuminated area A_{spot}. Hence, determining σ_{abs} is essential to calculate $\langle N\rangle$. The common method employed here is illustrated in Figure 3.5 using data of the QD ensemble discussed in Chapter 5.[117,147] The ΔOD signals at the main bleach upon excitation with various j_{avg} are time-averaged at relatively long delay times (here 2–3 ns as highlighted in Figure 3.5a) at which no more multi-excitons are left. These values are plotted in Figure 3.5b as a function of j_{avg}, and fitting the function $f(x) = 1 - e^{-x\cdot\sigma_{\text{abs}}}$ determines $\sigma_{\text{abs}} \approx 8.6\cdot 10^{-15}\ \text{cm}^2$. The analog procedure with time-averaging over 1.7–2.1 ns using data of the QD sample studied in Chapter 4 yields $\sigma_{\mathrm{abs}} \approx 1.9 \cdot 10^{-14}\,\mathrm{cm}^2$. Both values are consistent with literature.[188–191]

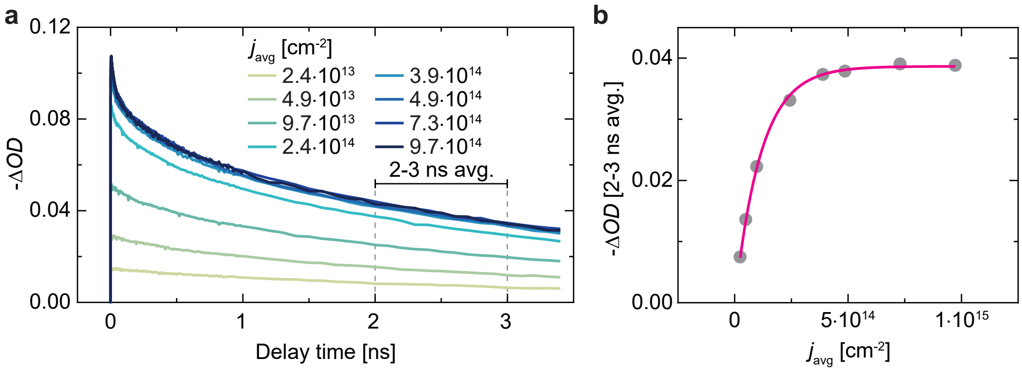

Figure 3.5: Average Quantum Dot Excitation. (a) $-\Delta OD$ signal of the main bleach of the QD ensemble discussed in Chapter 5 with the time average over 2–3 ns indicated. **(b)** Corresponding $-\Delta OD$ values average over 2–3 ns as a function of the spatially-averaged number of photons per pulse per area j_{avg}.

3.4 Amplified Spontaneous Emission Studies

In order to test the potential of a material for light amplification, its ability to generate amplified spontaneous emission (ASE) is typically tested first (see Subsection 2.2.3). A common method for this kind of measurement involves illuminating the sample with a stripe-like spot. ASE can build up along the stripe, and the emitted light is detected in a 90° angle along the stripe.[168] In the following, the experimental setup is introduced, and two critical parameters are discussed: the excitation fluence and the length of the illuminated stripe. By varying these parameters, the ASE threshold and the net optical gain coefficient can be determined, respectively.

3.4.1 Density-Dependent Emission Detection

The same *Libra-HE+* amplifier system as detailed in Subsection 3.3.1 is used as the light source for the ASE studies. The 800 nm output is frequency doubled to 400 nm via SHG in a BBO crystal (see Subsection 3.3.2), as shown in the setup illustration in Figure 3.6. The remaining 800 nm light is blocked by a short-pass excitation filter, and the pulse energy is adjusted with a variable ND filter. The approximately Gaussian-shaped laser beam is focused in one dimension by a *LJ1567L2-A* cylindrical lens from *Thorlabs*, creating a roughly rectangular-shaped beam profile. The stripe-like focus spot, with its longer side parallel to the optical table, is aligned to the sample using a variable slit so that one end of the excitation stripe coincides with the sample edge. The stripe length is adjusted by a movable edge plate. Further details on the sample preparation are given below, while the purpose of the variable stripe length is discussed in Subsection 3.4.2.

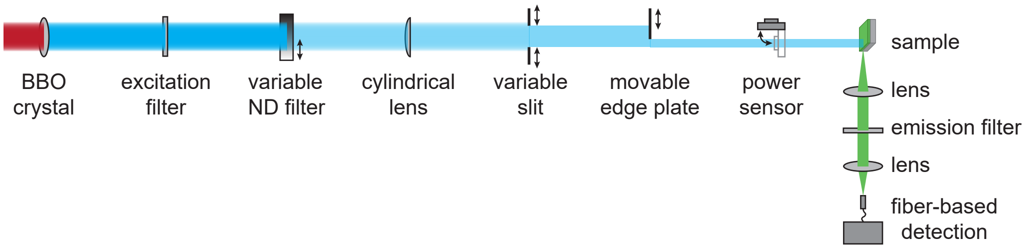

Figure 3.6: Amplified Spontaneous Emission Setup. The frequency-doubled laser beam is focused to a rectangular spot by a cylindrical lens. The spot is aligned to the sample edge by a variable slit and its length adjusted by a movable edge plate. The light emitted by the sample, which is deposited on a substrate, is collected in a 90° angle.

A power meter sensor can be placed between the edge plate and the sample. The light that is emitted from the sample and travels along the stripe towards the aligned edge is collected and again focused by two plano-convex lenses. In between, a long-pass emission filter blocks scattered laser light. The collected light is focused onto an optical fiber connected to a *FLAME-T-XR1* miniature spectrometer from *OceanInsight* that is used to acquire the spectra. Due to the 90° angle between the excitation and emission path, the alignment of the optical components is especially crucial. Therefore, the detection optics were mounted in a cage system to avoid measurement artifacts.

Sample Preparation

As discussed in Subsection 2.2.3, ASE measurements are typically performed on QDs deposited on a substrate. This is necessary to reach a sufficiently high QD density for the stimulated emission to overcome losses.[112,113] The colloidal QD dispersion used in this thesis was dropcasted onto Si substrates. These were chosen over glass, even though glass has a lower refractive index and would, in principle, be more more suitable for waveguiding in the QD film. However, the high transparency of glass in the used wavelength range can lead to reflections of scattered light inside the glass, complicating alignment and potentially introducing measurement artifacts. The drop was distributed across the entire $1 \times 1\,\mathrm{cm}^2$ substrate to ensure that the resulting thin film of QDs extended to the edge of the substrate. To slow down the evaporation of the solvent, the substrate was covered with a small glass bowl. This ensures a homogeneous distribution of QDs, allowing the QD film to be used for multiple measurements under the same conditions by simply moving the substrate perpendicular to the optical table.

Determining the Amplified Spontaneous Emission Threshold

The ASE threshold is the excitation density at which a sufficient number of QDs are in an optical gain state, so that stimulated emission dominates over losses, as detailed in Subsection 2.2.3. It is typically quantified by the excitation fluence F given by

$$F = \frac{E_{\text{pulse}}}{A_{\text{spot}}}, \tag{3.20}$$

with the pulse energy E_{pulse} and the illuminated area A_{spot}. To determine the correct E_{pulse} incident on the sample, the power meter sensor must be placed directly in front of the sample, i.e., after the slit (see Figure 3.6). The measured P_{avg} is converted into E_{pulse} with the repetition rate $f_{\text{rep}} = 1\,\text{kHz}$ using Equation 3.8. E_{pulse} can be tuned by the variable ND filter, as illustrated in Figure 3.6, while A_{spot} is kept constant.

The spot size is measured by replacing the sample with a *WincamD-UCD12-1310* beam profiler from *dataRay*, ensuring that its CCD detector is positioned at the same distance from the cylindrical lens as the sample. Figure 3.7a shows a false color image of the stripe-like beam spot at the sample position.

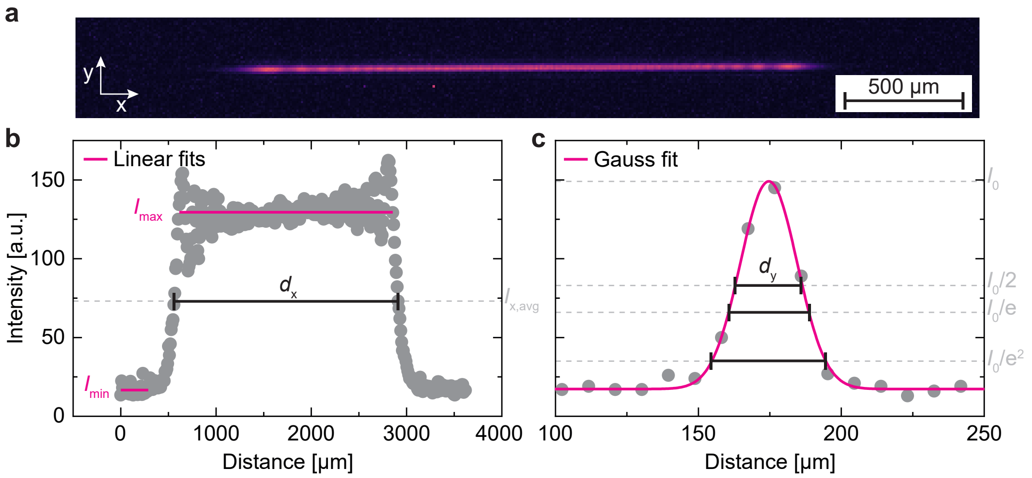

Figure 3.7: Analysis of Laser Spot Profile. **(a)** False color image of the laser beam spot at the sample position. **(b)** Intensity distribution along the longer side of the stripe-like spot with linear fits to parts of the curve. The determined length of the beam profile in the x-dimension d_x is indicated. **(c)** Intensity distribution along the shorter side with a Gaussian fit and various methods of determining its width d_y.

The intensity distribution along the longer side is displayed in Figure 3.7b, revealing an approximately rectangular-shaped profile in the x-dimension with relatively steep edges. The corresponding spot length d_x can be approximated by the width of the profile curve at its mean intensity, similar to the full width at half maximum (FWHM). The minimum intensity I_{min} is defined as the average over a range of 32 data points of the background signal, while the maximum intensity I_{max} is determined by the average over 242 data points at the signal plateau. A value of $d_x = 2350\,\mu\text{m}$ is extracted at the average intensity $I_{\text{x,avg}}$ given by

$$I_{\text{x,avg}} = \frac{I_{\text{min}} + I_{\text{max}}}{2}. \tag{3.21}$$

Along the shorter side, the beam profile can be approximated by a Gaussian peak, as shown in Figure 3.7c. The corresponding width in the y-dimension d_y can be defined in different ways, such as at an intensity drop of $1/2$, $1/e$, or $1/e^2$. In this case, d_y is found to be 23, 28, or 40 µm, depending on the chosen definition. Therefore, to properly compare ASE threshold values, the exact method for determining A_{spot} must be specified, which is, however, often not reported in literature. For this thesis, the full width at an intensity drop of $1/e^2$ was chosen.

Ultimately, for the ASE threshold determination presented in Figure 5.3, emission spectra were acquired at different excitation fluences. The emission intensity was integrated over a spectral range covering the ASE peak and plotted as a function of the excitation fluence, where a sudden change in slope indicates the onset of ASE. Since the data were not corrected for spontaneous emission, the slope before the ASE onset is nonzero. The two distinct regions were individually fitted with linear functions, with the fluence value at their intersection determining the ASE threshold.

3.4.2 Variable Stripe Length Method

In the variable stripe length (VSL) method, the length of the stripe-like spot d_x is varied, while spectra of the light emitted along the excited stripe are acquired.[168] As illustrated in Figure 3.6, the variable slit blocks the tails of the beam with a Gaussian intensity distribution, ensuring an almost rectangular intensity profile with relatively steep edges, as shown in Figure 3.7b. One part of the slit also aligns the beam with the substrate. For the VSL measurements, the excitation stripe length was varied using a movable edge plate controlled by a micrometer screw. A close-up of the setup that highlights the components just discussed is shown in Figure 3.8a.

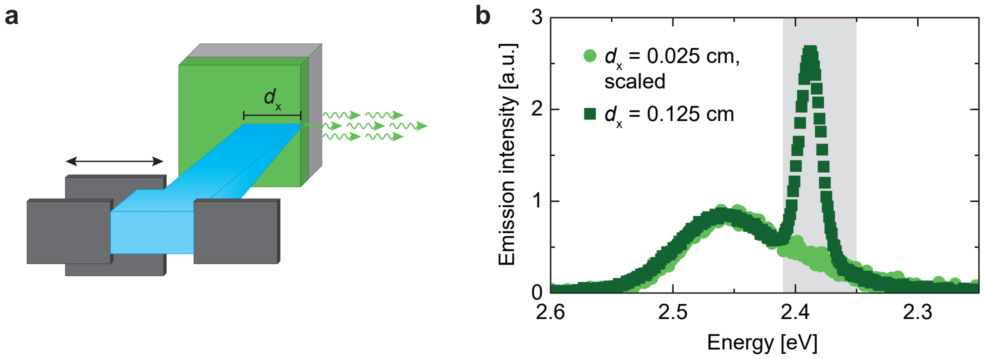

Figure 3.8: Variable Stripe Length Method. (a) The stripe-like focus is cut and aligned to the substrate using a variable slit. The stripe length d_x is varied by a movable edge plate. **(b)** Emission intensity for a stripe length of $d_x = 0.025$ cm (light green circles) scaled to the maximum of the spontaneous emission peak acquired at $d_x = 0.125$ cm (dark green squares). The gray shaded area highlights the spectral range covering the ASE peak in which the intensities were integrated and subtracted, yielding the integrated ASE intensity $I(d_x)$.

Determining the Net Optical Gain Coefficient

An exponential increase in the emission intensity with stripe length indicates net optical gain in the sample, characterized by a positive net optical gain coefficient $G > 0$ (see Equation 2.13). The intensity dependence on the stripe length $I(d_\mathrm{x})$ can be related to G and the spontaneous emission intensity per unit length I_l via

$$I(d_\mathrm{x}) = \frac{I_l}{G} \cdot \left(e^{G \cdot d_\mathrm{x}} - 1\right). \tag{3.22}$$

In this equation, gain saturation is not taken into account; thus, Equation 3.22 only describes the onset of $I(d_\mathrm{x})$, which may appear almost linear when $|G| \cdot d_\mathrm{x} \ll 1$. In this regime, the exponential factor can be approximated by a Taylor expansion $e^{G \cdot d_\mathrm{x}} \approx G \cdot d_\mathrm{x} + 1$, resulting in a linear intensity increase $I(d_\mathrm{x}) = I_l \cdot d_\mathrm{x}$. Hence, for small gain coefficients, the VSL method alone is not sufficient to confirm the presence of ASE.[62]

For the VSL analysis presented in Subsection 5.1.2, background spontaneous emission was subtracted using a reference spectrum measured at small $d_\mathrm{x} = 0.025\,\mathrm{cm}$, where only spontaneous emission is observed. This reference spectrum was scaled to the maximum of each spontaneous emission peak corresponding to different d_x values, as shown in Figure 3.8b for $d_\mathrm{x} = 0.125\,\mathrm{cm}$. The emission intensity in the spectral range covering the ASE peak (marked in gray) was integrated and corrected by subtracting the integrated intensity of the scaled reference in the same spectral range. The resulting values were used as the integrated ASE intensity $I(d_\mathrm{x})$ and fitted using Equation 3.22, revealing G.

4

Confined Excitons in Lead Halide Perovskite Quantum Dots

Most studies on III-V and II-VI QDs are performed on strongly confined QDs, where electrons and holes are described as individually confined before taking Coulomb effects into account (see Subsection 2.1.1).[53,67] Their atomic-like discrete energy levels and resulting optical properties have been widely investigated.[56,70,91–94,96,98,117,153,192] Nevertheless, a fundamental constraint of common semiconductors is their band structure, which has a hh/lh degeneracy around the band gap, leading to close lying energy levels that are difficult to resolve.[152,153] In contrast, this is not the case for lead halide perovskites (LHPs), where the band gap consists of a single VB and a single CB (see Subsection 2.2.1).[51] However, precise control over their size and shape remains challenging; as a result, inhomogeneous broadening in optical spectra often obscures the underlying energy landscape. Most studies on their excitonic properties have been conducted on relatively large NCs with edge lengths ≥10 nm without significant confinement.[154–158] A novel synthesis method for LHP QDs produces monodisperse spherical QDs.[54] Their diameter can be tuned within the range of 4–14 nm, enabling studies on confinement effects and their optical properties with reduced influence from inhomogeneous broadening. Detailed insight into the energy levels and charge-carrier behavior of LHP QDs around the band gap enhances understanding of their optical properties, supporting their advancement in applications such as light-emitting devices and lasers.

This chapter is based on the main results of Reference 193. Spherical LHP QDs are studied with the goal of understanding their confined energy landscape and excited-state behavior. First, fundamental optical properties of spherical $CsPbBr_3$ QDs are introduced in Section 4.1, together with HAADF-STEM images confirming their spherical shape. The monodispersity of the QDs allows to resolve individual energy levels to study their quantum confinement. Comparisons with model calculations in Section 4.2 render the weak confinement model suitable to describe the energy landscape of the QDs as center-of-mass motion confined excitons. This provides the basis to further study excited states of the LHP QDs in Section 4.3. In transient absorption (TA) spectroscopy (introduced in Subsection 3.3.3), a multitude of spectral features is observed. Their spectral shape and polarization-dependent behavior are reproduced by modeling the excited-state absorption and subsequently TA spectra by considering bleached excitonic and induced biexcitonic transitions as main contributions. This assignment is further confirmed by the temporal dynamics presented in Section 4.4.

4.1 Structural and Steady-State Optical Properties

To ensure the spherical size of the QDs synthesized following the method described in Section 3.1, HAADF-STEM images as shown in Figure 4.1 were acquired. The overview image in Figure 4.1a shows the assembly of QDs in a monolayer. They do not arrange in a cubic lattice, as would be expected for cube-shaped QDs, but in a hexagonal lattice indicating a spherical QD shape.[54] The few-nm-sized high-contrast particles observed at the edges of some QDs are attributed to metallic lead clusters formed upon exposure to the electron beam.[194] The gap of a few nm between the QDs is caused by the ligands, here lecithin.

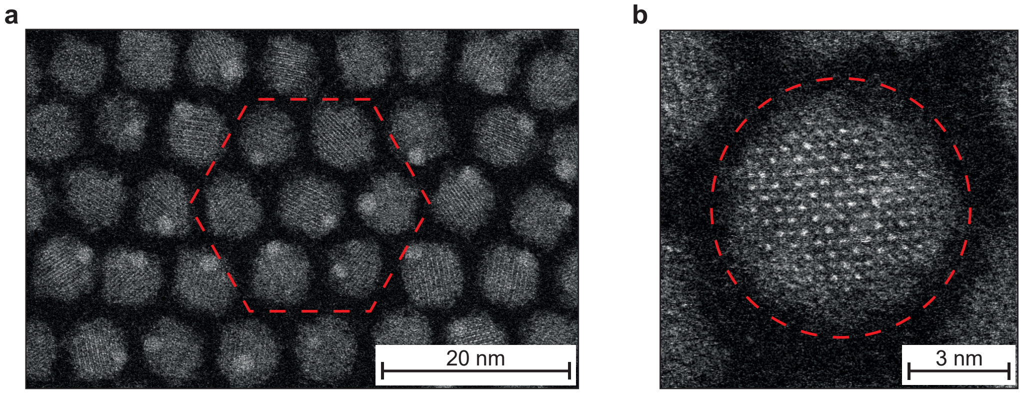

Figure 4.1: HAADF-STEM Images. (a) Overview image of $CsPbBr_3$ QDs indicating their assembly in a hexagon-like pattern. **(b)** Close-up of a single QD showing its spherical shape and high crystallinity. HAADF-STEM measurements were performed in collaboration with Dr. Markus Döblinger from the Department of Chemistry at LMU Munich.

A close-up of a single QD in Figure 4.1b confirms the spherical-like shape and also its high crystallinity. Naturally, the shape of the QDs is not a perfect sphere and has also been described as spheroidal or, more precisely, as rhombicuboctahedral.[54] In the context of this thesis, the shape is described as spherical, as this is a sufficiently good approximation, and to highlight the difference to common cubic or cuboidal LHP NCs.

Figure 4.2a shows a steady-state absorption and PL spectrum of a spherical $CsPbBr_3$ QD ensemble in solution. The QDs are ~7 nm in diameter and have lecithin as ligands. The absorption resonances labeled X1, X2, and X3 are clearly distinct from each other, and the PL spectrum is redshifted from X1 by a Stokes shift $E_{\text{Stokes}} \approx 35\,\text{meV}$. Figure 4.2b shows spectra for different QD sizes, which were determined using the sizing curve reported in Reference 54 that correlates the energetic position of the first absorption peak to the QD size based on STEM measurements (see Subsection 3.2.1). It is apparent that towards larger QDs the absorption redshifts and the energetic distance between the peaks decreases. This is a clear indication of the quantum size effect, as introduced in Subsection 2.1.1. Furthermore, all absorption peaks can be fit by well-separated Gaussian peaks, shown in Figure A.1 in the Appendix. The clear shape of the absorption spectra reflects the inverted band structure of LHPs without a hh/lh degeneracy around the band gap, which is in contrast to conventional semiconductors, as discussed in Subsection 2.2.1.

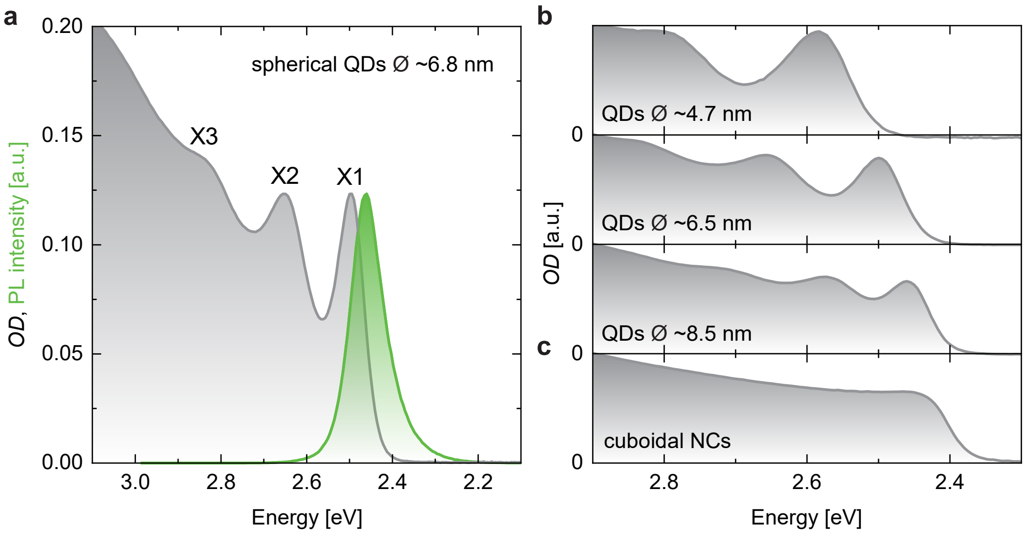

Figure 4.2: Steady-State Optical Properties of $CsPbBr_3$ NCs. (a) Steady-state absorption and PL spectra of spherical QDs with a diameter of ~7 nm and lecithin as ligands dispersed in hexane. X1, X2, and X3 denote the energetically lowest absorption resonances. **(b)** Absorption spectra of spherical QDs of different sizes. **(c)** Absorption spectrum of large cuboidal NCs, which were acquired and synthesized by Dr. Tushar Debnath using a hot-injection method.

Note that the monodispersity of the QDs, evident from the HAADF-STEM image in Figure 4.1a, is crucial for observing discrete energy levels in absorption spectra. For a broad size distribution, inhomogeneous broadening (introduced in Subsection 2.1.2) can lead to indistinguishable peaks. This can be seen in Figure 4.2c in the absorption spectrum of common cuboidal NCs that typically have a broader size distribution. Their smooth absorption spectrum is in contrast to the individual peaks observed for spherical QDs of similar size shown in the panel directly above. The nature of the distinct absorption resonances is studied in detail in the next section.

4.2 Assignment to the Weak Confinement Regime

It was shown in the previous section that the individual absorption peaks of $CsPbBr_3$ QDs exhibit the quantum size effect. Hence, the question arises as to which energy levels they actually represent, i.e., whether it is an excitonic system or not. To resolve this, the radius r of the QDs is compared to the exciton Bohr radius r_B that describes the spatial extent over which the exciton is delocalized. The strong and weak confinement models represent the limiting cases of $r < r_B$ and $r > r_B$, respectively, as detailed in Subsection 2.1.1. In the strong confinement model, excited electrons and created holes are individually confined by the QD potential, with the Coulomb interaction between them considered afterward, as illustrated in Figure 4.3a. In contrast, the weak confinement model reverses this order, treating the Coulomb interaction first, so that the exciton as a whole is confined by the QD potential, as illustrated in Figure 4.3b.

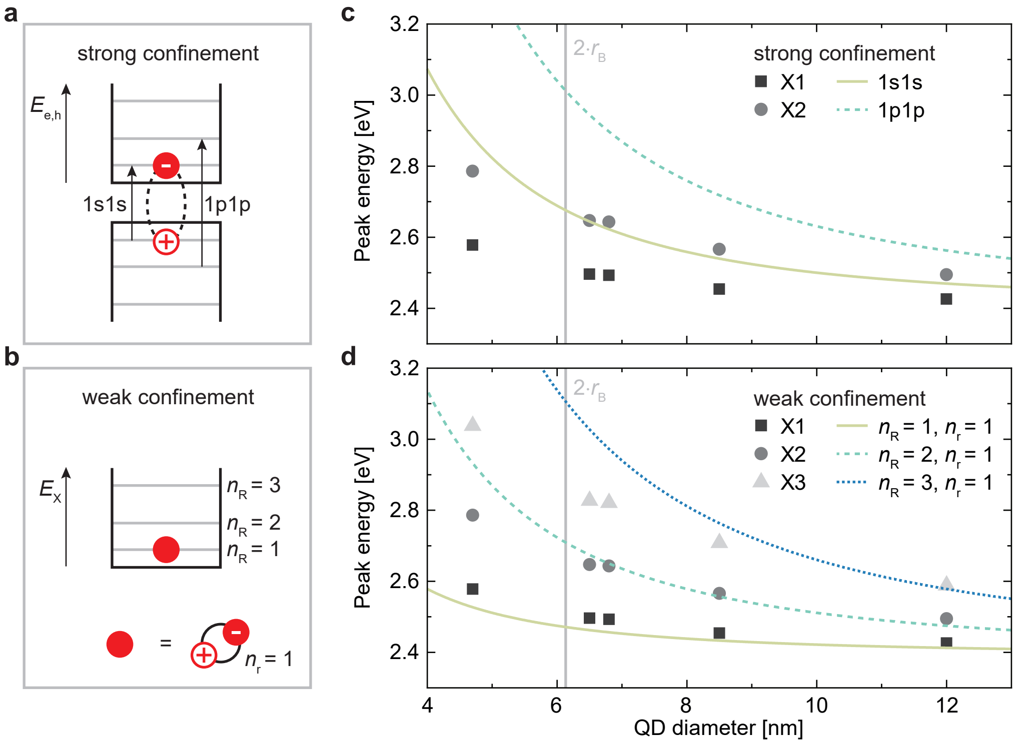

Figure 4.3: Weak and Strong Confinement Models. **(a)** Illustration of the strong confinement model highlighting the individual confinement of electron and hole before their Coulomb interaction is included (represented by the dashed line). The two energetically lowest transitions 1s1s and 1p1p are indicated. **(b)** The weak confinement model describes hydrogen-like excitons with internal states that are characterized by the quantum number n_r. These excitons are confined in their center-of-mass motion, resulting in discrete energy levels characterized by the quantum number n_R. The energy of the first absorption peaks of $CsPbBr_3$ QDs with different sizes are compared to the calculations based on **(c)** the strong and **(d)** the weak confinement model. The exciton Bohr diameter $2r_B$ is indicated.

Using Equation 2.3 and the parameters listed in Table 4.1, a value of $2r_\mathrm{B} = 6.13\,\mathrm{nm}$ is calculated for $\mathrm{CsPbBr_3}$, which is comparable to the diameter of the studied QDs. Therefore, neither the weak nor the strong confinement model is an obvious choice.

m_e^*	m_h^*	ε	E_gap [eV]
0.252	0.252	7.3	2.424

Table 4.1: Material Specific Parameters for $\mathrm{CsPbBr_3}$. Values of the effective electron and hole mass $m_\mathrm{e,h}^*$, the dielectric constant ε, and the band gap energy E_gap of bulk $\mathrm{CsPbBr_3}$[54] used for determining r_B and energy level calculations.

Advanced calculations using a $k{\cdot}p$ model and the Hartree-Fock approximation are reported in literature for spherical LHP QDs,[54] aiming to closely reproduce the observed absorption resonances. However, a more simplistic picture remains desirable to gain an intuitive understanding of the charge carriers created in the QDs upon photoexcitation. The aim of this section is to find a proper description of the quasi-particles excited in $\mathrm{CsPbBr_3}$ QDs that characterize their energy landscape: either individual electrons and holes or hydrogen-like excitons with a collective center-of-mass motion. For this purpose, Equation 2.7 and Equation 2.5 are used, along with the parameters listed in Table 4.1, to calculate the energy levels based on the strong and weak confinement model, respectively. These calculated energy levels are compared (not fit) with the measured absorption resonances of $\mathrm{CsPbBr_3}$ QDs of five different sizes, as shown in Figure 4.3c and Figure 4.3d, respectively.

Note that for the strong confinement model, the Coulomb interaction is already taken into account. However, Figure 4.3c indicates that the strong confinement model highly overestimates the energy of the first and second absorption peak for all QD sizes investigated. In Figure 4.3d, the calculated values of the weak confinement model are shown for the quantum numbers of the center-of-mass motion confinement $n_\mathrm{R} = 1, 2, 3$ and the relative motion $n_\mathrm{r} = 1$, which match well with the measured peak energies, especially for the first and second absorption peaks. For the largest measured QD diameter of ~12 nm, the agreement between measurements and model calculations is almost perfect for all three peak energies. This is expected since the weak confinement model is designed for this size range ($r > r_\mathrm{B}$). However, the intermediate sizes of ~7 nm in diameter are also well reproduced by this model.

Due to the considerable agreement of the measured absorption peak energies with the weak confinement model, and not with the strong confinement model, the weak confinement model seems appropriate to describe the energy levels of the QDs in the studied size range. Therefore, the quasi-particles created upon excitation can be well described as hydrogen-like Wannier-Mott excitons that are confined in their center-of-mass motion. Hence, the first absorption peak corresponds to the lowest-confined exciton level, while the second and third peaks represent the next higher confinement levels. This can be pictured as an exciton-in-a-box as illustrated in Figure 4.3b.

4.3 Biexciton Formation in the Excited State

In the previous section, it was established that excitons confined in their center-of-mass motion describe the energy levels populated via ground-state absorption. In other words, upon photoexcitation, an exciton is created that is delocalized over (almost) the entire QD due to $r \approx r_B$. However, for applications such as lasing[48] or generation of entangled photon pairs[45,46,134] the excitation of more than one electron-hole pair per QD is often necessary. Hence, the question arises as to what happens to the excited spherical $CsPbBr_3$ QDs upon a second excitation. This was studied via transient absorption (TA) spectroscopy, where the absorption of the system in an excited state is compared to the absorption of the ground state, as detailed in Subsection 3.3.3.

First, a typical TA spectrum of large cuboidal $CsPbBr_3$ NCs at a pump-probe delay time of 100 ps, along with their absorption spectrum, is shown in Figure 4.4a. The TA spectrum has a single negative and a positive feature, where the former resembles ground-state bleaching due to phase-space filling (see Subsection 3.3.3).[86,195]

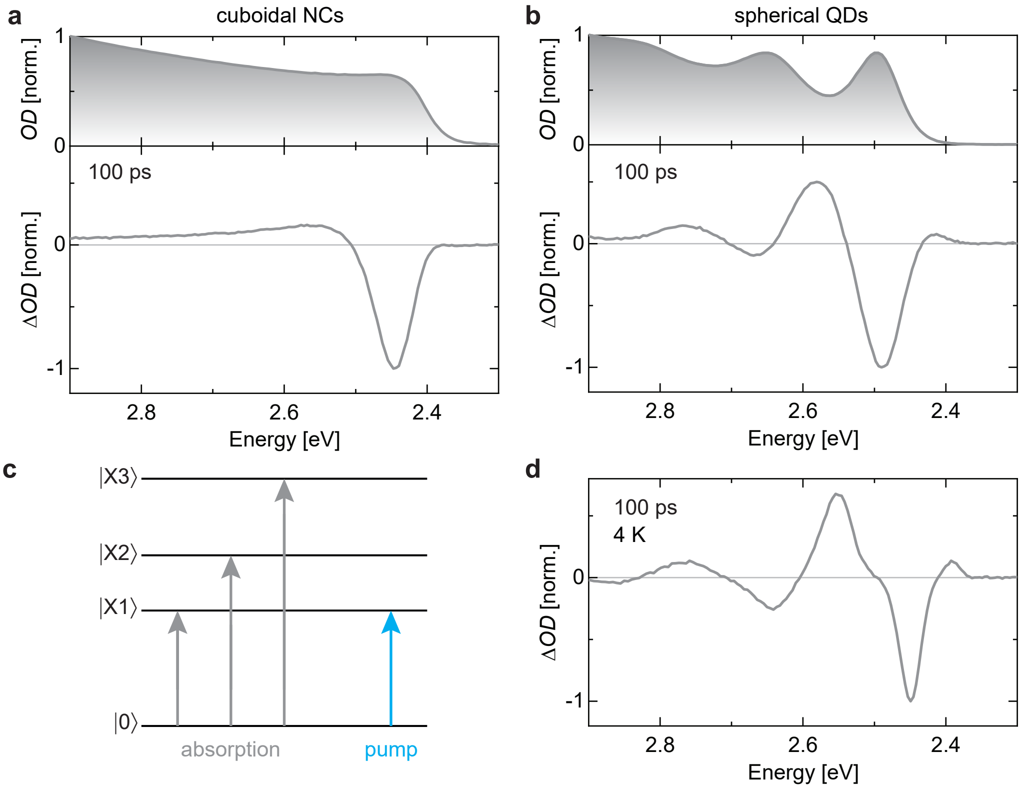

Figure 4.4: Transient Absorption Measurements. Absorption and TA spectra at a time delay of 100 ps at room temperature upon resonant pumping of **(a)** large cuboidal $CsPbBr_3$ NCs (synthesized and measured by Dr. Tushar Debnath) and **(b)** spherical $CsPbBr_3$ QDs with a diameter of ~6.8 nm. **(c)** Level scheme illustrating the ground state absorption transitions and the X1-resonant pumping of the QDs. **(d)** TA spectrum of the same QDs as in (b) at a temperature of 4 K and 100 ps delay time.

In contrast, absorption and TA spectra of spherical $CsPbBr_3$ QDs with a diameter of ~6.8 nm at the same 100 ps time delay are shown in Figure 4.4b. The TA spectrum, which qualitatively resembles the second derivative of the absorption spectrum,[90,153,192] exhibits several positive and negative peaks. The negative peaks coincide with the absorption resonances, while the positive signals appear redshifted relative to them. Notably, the monodispersity and resulting reduced inhomogeneous broadening of the spherical QDs enable the resolution of distinct TA signals and absorption resonances.

In analogy to the negative TA signal in Figure 4.4a, one could assume that the two negative signals in Figure 4.4b are also due to phase-space filling from occupied X1 and X2 states. However, as illustrated in the level scheme in Figure 4.4c, the QD sample is pumped resonantly to the X1 level with an energy of ~2.49 eV, while X2 is at an energy of ~2.64 eV. The energy difference between the two levels of ~150 meV cannot be overcome by the thermal energy at room temperature (~25 meV), and certainly not at 4 K (<1 meV), where, additionally, the overlap between the individual signals is strongly reduced. A TA measurement at a temperature of 4 K is shown in Figure 4.4d, with a qualitatively similar spectral shape to that at room temperature in Figure 4.4b. The main differences are the narrower, less overlapping features, resulting from the strongly reduced homogeneous broadening due to less phonon scattering, and a slight redshift of the spectrum caused by the compressed unit cell and the resulting decreased in the band gap of $CsPbBr_3$ at lower temperatures.[196,197] This leads to the conclusion that the negative TA signal coinciding with the X2 absorption peak does not originate from the occupation of this energy level. In contrast, the X1 level is occupied and, therefore, its bleach is be attributed to phase-space filling. To further investigate the excited-state processes, TA spectra are examined in more detail below.

4.3.1 Polarization-Selective Properties Reveal Biexciton Formation

Positive signals in TA spectra of perovskite NCs have been attributed to various origins: from polarons over activation of forbidden transitions to biexcitons.[190,191,198–200] In the following, the energetically lowest positive TA signal of the spherical QDs is examined for a possible biexcitonic origin. For this purpose, polarization-dependent TA spectroscopy is employed (see experimental details in Subsection 3.3.3). The pump and probe beams either have the same or opposite circular polarization, referred to as co- and counter-circular polarized, respectively. The level scheme in Figure 4.5a shows circular-polarized transitions between the ground state, the energetically lowest exciton X1, and the biexciton X1X1, including their respective total angular momentum projections J_z.[201]

Upon pumping with σ^+ light, an X1 exciton with $J_z = +1$ is excited, referred to as $|+1\rangle_{X1}$. Only subsequent counter-circular polarized σ^- light can excite a X1X1 biexciton with $J_z = 0$, denoted $|0\rangle_{X1X1}$, while an X1X1 biexciton with $J_z = +2$ is forbidden. However, if the second

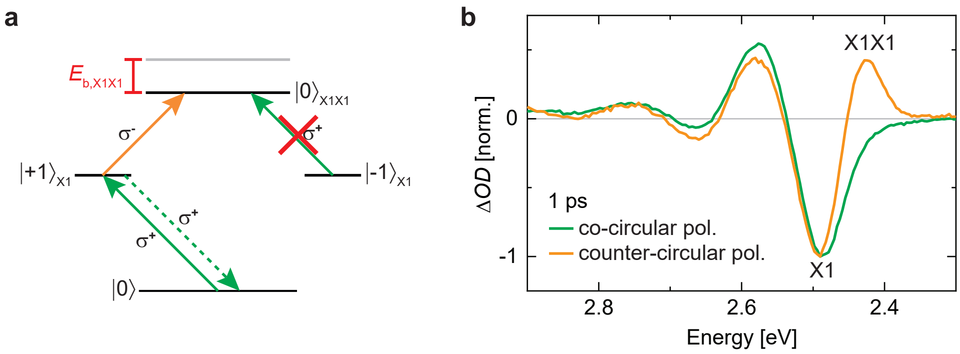

Figure 4.5: Polarization-Selective X1X1 Biexciton Formation. **(a)** Level scheme illustrating circular-polarized TA spectroscopy, where the X1X1 biexciton level can be populated by counter-circular polarized pump and probe beams, while stimulated X1 emission is possible in the co-circular polarized case. The biexciton binding energy $E_{\mathrm{b,X1X1}}$ is indicated. **(b)** Normalized TA spectra at a delay time of 1 ps under co- (green line) and counter-circular polarized conditions (orange line). The X1 bleach is indicated, along with the induced X1X1 absorption signal that is only observed in the counter-circular polarized case.

beam is co-circular polarized with σ^+ light, stimulated emission $|{+1}\rangle_{\mathrm{X1}} \longrightarrow |0\rangle$ is possible.[128,202] The corresponding TA spectra at a delay time of 1 ps are shown in Figure 4.5b for co- and counter-circular polarized pump and probe beams. In the counter-circular polarized case, a strong positive induced absorption peak is observed redshifted to the X1 bleach. It completely vanishes in the co-circular polarized case. This behavior follows the biexciton formation scheme illustrated in Figure 4.5a and suggests that the energetically lowest positive signal is induced absorption to the X1X1 biexciton $|{+1}\rangle_{\mathrm{X1}} \longrightarrow |\mathrm{X1X1}\rangle$. Note that stimulated emission is not apparent in Figure 4.5b because the spectra are normalized to the X1 bleach minimum to highlight the difference in the lower-energy part of the spectrum.

The spectral position of the X1X1 biexciton on the lower-energy side of the X1 bleach indicates that X1X1 is an attractive biexciton. Its biexciton binding energy $E_{\mathrm{b,X1X1}} = 2E_{\mathrm{X1}} - E_{\mathrm{X1X1}}$ can be determined from the spectral shift between the X1 and X1X1 signals, as shown in Figure 4.6. As in the co-circular polarized case, the X1X1 signal is absent, so the X1 bleach only overlaps with one positive signal at higher energies. Gaussian fits to the bleach and the adjacent positive signal indicate the spectral position of the X1 bleach at ~2.48 eV, as shown in Figure 4.6a. This peak position of the X1 bleach is fixed when fitting three Gaussian peaks to the counter-circular polarized spectrum in Figure 4.6b. The position of the X1X1 peak is identified at ~2.44 eV. The resulting X1X1 biexciton binding energy $E_{\mathrm{b,X1X1}} \approx 40$ meV is similar to biexciton binding energies reported in literature for $\mathrm{CsPbBr_3}$ QDs of similar sizes.[128,199] After identifying the origin of the energetically lowest positive TA signal as induced absorption to the X1X1 biexciton, the remaining signals are discussed in the following.

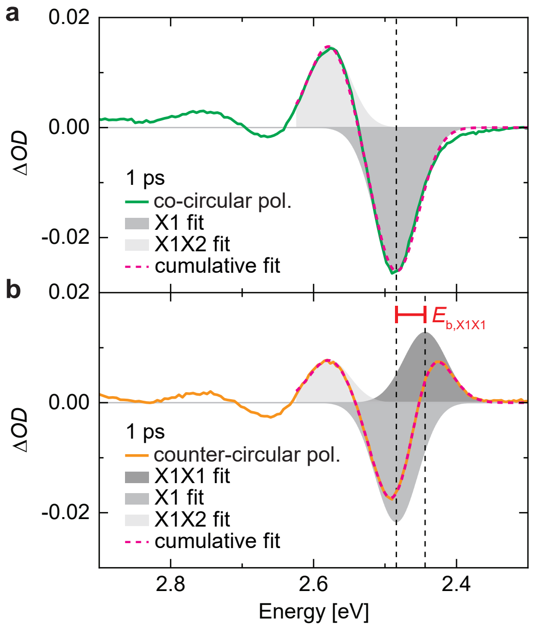

Figure 4.6: Biexciton Binding Energy Determination. TA spectra at a delay time of 1 ps for **(a)** co- and **(b)** counter-circular polarized conditions with Gaussian fits to the main spectral features indicating the biexciton binding energy $E_{b,X1X1}$.

4.3.2 Modeling Transient Absorption Spectra

In the previous section, the energetically lowest positive TA signal was attributed to induced X1X1 absorption, while the origin of the other positive signals remains to be explained. The negative signal coinciding with the X1 absorption resonance is attributed to phase-space filling of this state; however, this process can be excluded for the other negative signal at the X2 energy. In this section, the origin of all positive and negative TA signals observed for spherical $CsPbBr_3$ QDs with a diameter of ~6.8 nm is analyzed. Building upon previous works on CdSe QDs,[192,203–205] the absorption of the excited state, and subsequently the TA spectrum, is modeled based on the ground-state absorption spectrum. For this purpose, Equation 3.14 describing the TA spectrum is written in an expanded form as

$$\begin{aligned}\Delta OD_{\text{model}}(E) &= OD_{\text{pump}}(E) - OD_{\text{no pump}}(E) = \\ &= \left[OD_{\text{pump, not exc.}}(E) + OD_{\text{pump, exc.}}(E)\right] - OD_{\text{no pump}}(E).\end{aligned} \tag{4.1}$$

It highlights that $OD_{\text{pump}}(E)$ contains contributions of unexcited and excited QDs represented by $OD_{\text{pump, not exc.}}(E)$ and $OD_{\text{pump, exc.}}(E)$, respectively. This is necessary because, depending on the pump power, not all of the QDs are actually excited, as the number of excitons created per QD follows Poisson statistics (see Equation 2.8). For the TA measurements shown in this chapter, the average number of excitons created per QD is $\langle N \rangle \approx 0.45$, determined as detailed in Subsection 3.3.3, with the ΔOD values averaged over 1.7–2.1 ns delay time. Thus, 55 % of the QDs are expected to remain unexcited by the pump beam.

The different contributions to $\Delta OD_{\text{model}}(E)$ are modeled by considering the following processes: bleached excitonic transitions, induced biexcitonic transitions including a biexciton binding energy $E_{\text{b,XX}} \approx 40\,\text{meV}$ (see Figure 4.6), stimulated emission considering the Stokes shift $E_{\text{Stokes}} \approx 35\,\text{meV}$ (see Figure 4.2), and $\langle N \rangle \approx 0.45$ as described above. The measured absorption spectrum $OD(E)$ (see Figure 4.2a or the top panel in Figure 4.4b) serves as the starting point for the modeling process.

First, $OD_{\text{no pump}}(E)$ is discussed. Without prior pumping, the probe beam exclusively monitors unexcited QDs, i.e., transitions from the ground state to confined excitons $|0\rangle \longrightarrow |\text{X}i\rangle$ with $i = 1, 2, 3$, as discussed in Section 4.2. The corresponding transitions that are possible in 100 % of the QDs are illustrated in Figure 4.7a on the left. Hence, $OD_{\text{no pump}}(E)$ is simply the measured absorption spectrum given by

$$OD_{\text{no pump}}(E) = OD(E). \tag{4.2}$$

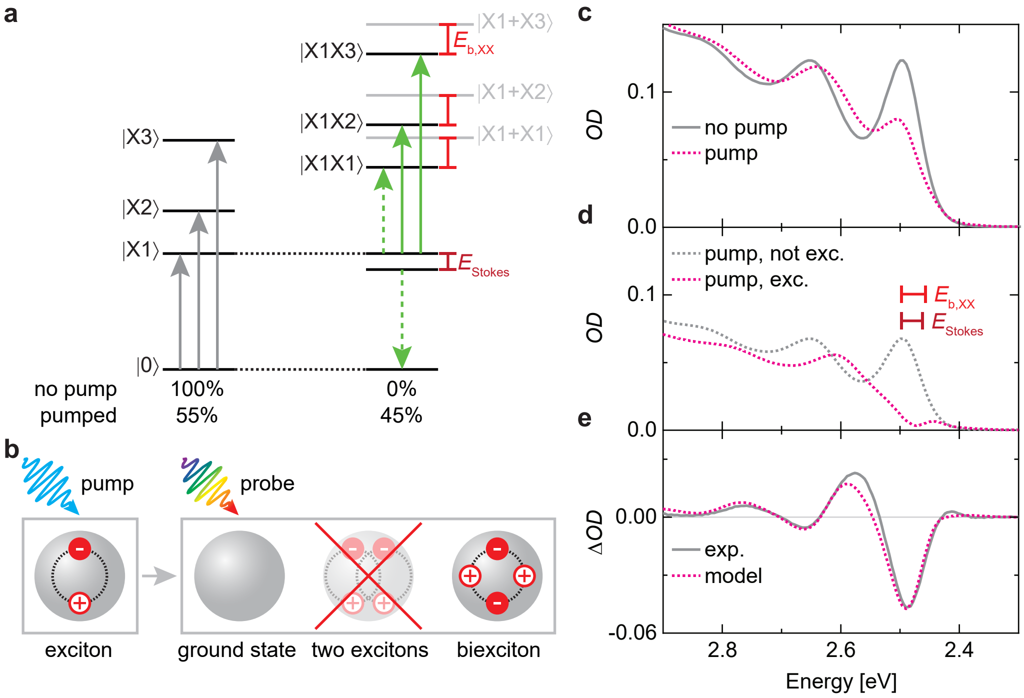

Figure 4.7: Modeling of Excited State Absorption and Transient Absorption Spectra. (a) Level scheme illustrating excitonic and biexcitonic transitions, where the latter are redshifted by the biexciton binding energy $E_{\text{b,XX}}$ (red), along with stimulated emission that is Stokes-shifted by E_{Stokes} (dark red). Dashed arrows indicate polarization-selective transitions. **(b)** Illustration of a QD pumped to the X1 exciton, where the subsequent probe beam can induce stimulated emission to the ground state; also it cannot create the same independent X1 exciton but an attractive biexciton. **(c)** Measured absorption spectrum as $OD_{\text{no pump}}(E)$ (gray line) and the modeled $OD_{\text{pump}}(E)$ (pink dotted line) that is the sum of **(d)** $OD_{\text{pump, not exc.}}(E)$ and $OD_{\text{pump, exc.}}(E)$ (gray and pink dotted line, respectively). **(e)** Measured TA spectrum at a delay time of 100 ps upon X1-resonant linear-polarized pumping (gray line) together with $\Delta OD_{\text{model}}(E)$ (pink dotted line).

The situation changes when the sample is pumped resonantly to the X1 level. For the 55 % of the QDs not excited by the pump, the probe beam still monitors the same excitonic transitions $|0\rangle \longrightarrow |\mathrm{X}i\rangle$. Hence, considering the corresponding fraction of QDs, their absorbance $OD_{\text{pump, not exc.}}(E)$ can be modeled as

$$OD_{\text{pump, not exc.}}(E) = 0.55 \cdot OD(E). \tag{4.3}$$

Finally, for the 45 % of the QDs actually excited by the pump beam, the probe monitors the different transitions that are illustrated in Figure 4.7a on the right. First, with the X1 level populated, stimulated emission $|\mathrm{X1}\rangle \longrightarrow |0\rangle$ occurs, after which the QD is left in the ground state, illustrated in Figure 4.7b. The stimulated emission is expected to be redshifted from the ground state absorption $|0\rangle \longrightarrow |\mathrm{X1}\rangle$ by $E_{\text{Stokes}} \approx 35\,\text{meV}$. Furthermore, because the pumped X1 exciton is delocalized over the entire QD (see Section 4.2), the probe beam can no longer monitor the same excitonic transitions, i.e., it cannot create a second independent exciton. Thus, all excitonic transitions are bleached yielding negative TA signals Xi. Instead, any additional exciton created by the probe has Coulomb interaction with the pumped X1 exciton, forming a biexciton (Figure 4.7b on the right). These biexcitonic transitions $|\mathrm{X1}\rangle \longrightarrow |\mathrm{X1X}i\rangle$ result in positive TA signals, which are redshifted relative to the excitonic transitions by $E_{\text{b,XX}}$ (Figure 4.7a on the right). The biexciton binding energy is approximated to be the same for all biexcitons, so that $E_{\text{b,XX}} = E_{\text{b,X1X1}}$. Note that the stimulated emission $|\mathrm{X1}\rangle \longrightarrow |0\rangle$ and the induced absorption to the energetically lowest biexciton $|\mathrm{X1}\rangle \longrightarrow |\mathrm{X1X1}\rangle$ are both polarization selective, as discussed in Figure 4.5, which is indicated by the dashed arrows in Figure 4.7a. All these processes contribute to $OD_{\text{pump, exc.}}(E)$, which can be written as

$$OD_{\text{pump, exc.}}(E) = 0.45 \cdot \big[OD(E - E_{\text{b,XX}}) - 0.5 \cdot OD_{\text{X1}}(E - E_{\text{b,XX}}) - 0.5 \cdot OD_{\text{X1}}(E - E_{\text{Stokes}})\big]. \tag{4.4}$$

$OD(E - E_{\text{b,XX}})$ represents the bleached excitonic and induced biexcitonic transitions, while $OD_{\text{X1}}(E)$ indicates the absorption associated with the X1 exciton, determined by Gaussian fits to the absorption spectrum, as shown in Figure A.1 in the Appendix. The latter is used to account for the polarization selectivity of the X1X1 formation and stimulated emission, shifted by $E_{\text{b,XX}}$ and E_{Stokes}, respectively, with intensity corrections by a factor of 0.5 that are discussed in more detail below. Ultimately, by combining all contributions from Equation 4.2, Equation 4.3, and Equation 4.4, $\Delta OD_{\text{model}}(E)$ can be described as

$$\begin{aligned}\Delta OD_{\text{model}}(E) = {} & [0.55 \cdot OD(E) + \\ & + 0.45 \cdot \big(OD(E - E_{\text{b,XX}}) - 0.5 \cdot OD_{\text{X1}}(E - E_{\text{b,XX}}) - 0.5 \cdot OD_{\text{X1}}(E - E_{\text{Stokes}})\big)] - \\ & - OD(E).\end{aligned} \tag{4.5}$$

The modeling is illustrated in Figure 4.7c-e. In Figure 4.7c, $OD_{\text{no pump}}(E)$ is shown alongside $OD_{\text{pump}}(E)$. The latter is the sum of $OD_{\text{pump, not exc.}}(E)$ and $OD_{\text{pump, exc.}}(E)$, which are displayed in Figure 4.7d. The resulting $\Delta OD_{\text{model}}(E)$ is compared in Figure 4.7e to the experimentally measured TA spectrum at a delay time of 100 ps at which only excitons remain.[159] Thus, the few multi-excitons created by the pump due to Poisson statistics are neglected in the model.

The shape of the TA spectrum is well reproduced by the model showing all the observed resonances at similar energies. Notably, there is an almost perfect agreement for the X1 bleach, which is especially striking because the measured and modeled data are not normalized. This indicates that the model includes the most relevant processes. Furthermore, it validates the previous assignment of the absorption resonances in Section 4.2 to center-of-mass motion-confined excitons and the subsequent bleaching of excitonic transitions along with induced biexcitonic transitions in TA measurements. The importance of including stimulated emission and the polarization selectivity of the X1X1 biexciton in the model is illustrated below.

The Importance of Stimulated Emission and Polarization Selectivity

In the following, the contributions from stimulated emission and the polarization selectivity of the X1X1 biexciton are subsequently removed from the model to investigate their influence on the modeled signals. As discussed in Figure 4.5a, stimulated emission contributes to bleaching (see Equation 3.16) of the corresponding transition in the co-circular polarized but not in the counter-circular polarized case. The linear-polarized case considered in the model can be treated as a superposition of the two opposite circular-polarized cases,[206] hence the weighting of 50 % in $0.5 \cdot OD_{\text{X1}}(E - E_{\text{Stokes}})$. The appropriate spectral position is determined by the Stokes shift $E_{\text{Stokes}} \approx 35\,\text{meV}$. Its origin in perovskites has been assigned to various processes such as reabsorption,[207] a confined hole state,[208] or polaron formation.[209,210] Regardless of its origin, it implies that stimulated emission occurs from this Stokes-shifted energy level (hence $E - E_{\text{Stokes}}$). The influence of removing this term from Equation 4.4 and Equation 4.5 is illustrated in Figure 4.8a and Figure 4.8b, respectively. It leads to an underestimated and shifted X1 bleach in the modeled TA spectrum, while the contribution to the X1X1 biexciton is overestimated.

The X1X1 biexciton formation is also polarization selective (see Figure 4.5), which is taken into account by the term $0.5 \cdot OD_{\text{X1}}(E - E_{\text{b,XX}})$ contributing to the 45 % of the QDs excited by the pump. Figure 4.8c illustrates an X1-resonant σ^+ pump that populates the $|{+1}\rangle_{\text{X1}}$ level. For simplicity, the analogous case of a σ^- pump populating the $|{-1}\rangle_{\text{X1}}$ level is not explicitly discussed. Thus, only a counter-circular polarized σ^- probe can populate the $|0\rangle_{\text{X1X1}}$ level, as discussed in Figure 4.5a. However, this does not apply to transitions to biexcitons in higher confinement levels X1Xi with $i \neq 1$, as illustrated in Figure 4.8c for the X1X2 biexciton. In this case, both a co- and counter-circular polarized probe can create a biexciton, $|{+2}\rangle_{\text{X1X2}}$ and

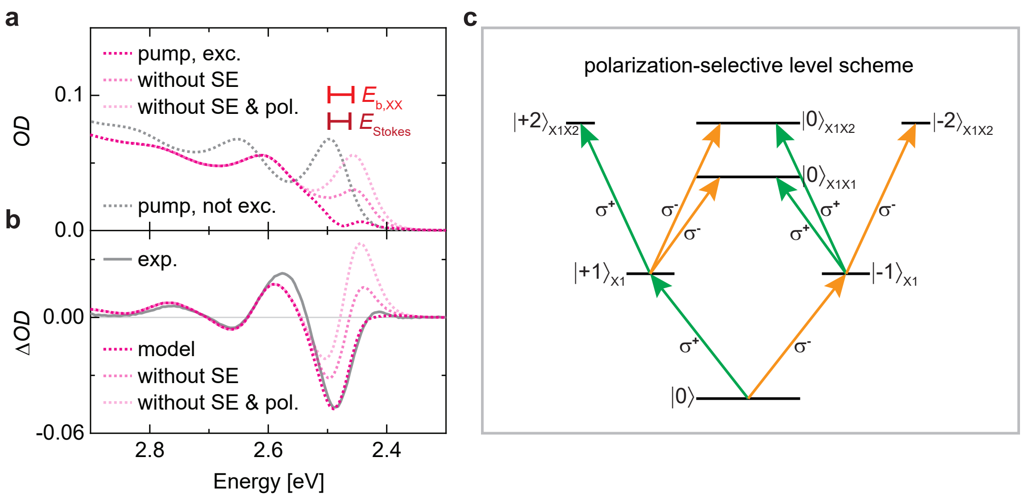

Figure 4.8: Contribution of Polarization and Stimulated Emission to the Modeling. **(a)** $OD_{\text{pump, not exc.}}(E)$ (gray dotted line) and $OD_{\text{pump, exc.}}(E)$ (pink dotted line) compared with $OD_{\text{pump, exc.}}(E)$ without the contribution of stimulated emission (SE, medium pink dotted line) and without both stimulated emission and polarization selectivity of X1X1 (light pink dotted line). **(b)** Measured TA spectrum at a delay time of 100 ps upon X1-resonant linear-polarized pumping (gray line) compared to $\Delta OD_{\text{model}}(E)$ (pink dotted line) and $\Delta OD_{\text{model}}(E)$ without the contribution of stimulated emission (SE, medium pink dotted line) and without both stimulated emission and polarization selectivity of X1X1 (light pink dotted line). **(c)** Level scheme illustrating the polarization-selective formation of the X1X1 and the X1X2 biexciton. For equal population of $|+1\rangle_{X1}$ and $|-1\rangle_{X1}$, X1X1 can be created via two pathways and X1X2 via four.

$|0\rangle_{X1X2}$, respectively.[128,202] For the linear-polarized case of the model, $|+1\rangle_{X1}$ and $|-1\rangle_{X1}$ are populated equally. Thus, there are in total four possible ways to create an X1X2 biexciton, while only two paths lead to $|0\rangle_{X1X1}$. This is taken into account by lowering the contribution of the induced X1X1 absorption by 50 % compared to X1Xi with $i \neq 1$. Removing also this term from Equation 4.4 and Equation 4.1 results in an even stronger underestimation and shift of the X1 bleach and in substantially overestimated induced X1X1 absorption (see Figure 4.8a and Figure 4.8b, respectively). This highlights the importance of including stimulated emission as well as polarization selectivity of this process and of the X1X1 biexciton formation to properly model the TA spectrum.

A Comprehensive Picture of the TA Spectrum

The presented model only considers attractive biexcitons (no unbound or repulsive biexcitons) to be formed upon pump and subsequent probe excitation, all having the same biexciton binding energy $E_{b,XX}$. The same linewidths and transition strengths[205] given by the measured absorption spectrum for $|0\rangle \longrightarrow |Xi\rangle$ are used for the corresponding $|X1\rangle \longrightarrow |X1Xi\rangle$ transitions. Nevertheless, the TA spectrum is modeled remarkably well. More importantly, the model provides an explanation for all signals observed in the visible spectral range, not only the main bleach and adjacent features. Therefore, the model provides a comprehensive description of the main processes involved in the TA pump-probe measurement: Bleached excitonic transitions at the positions of X1 and X2, along with induced transitions to the X1X*i* biexcitons that are redshifted relative to the excitons by $E_{\mathrm{b,XX}}$. The X1X1 signal and stimulated X1 emission are thereby polarization selective, with the latter being energetically redshifted by E_{Stokes}. A TA spectrum with all signals assigned accordingly is shown in Figure 4.9.

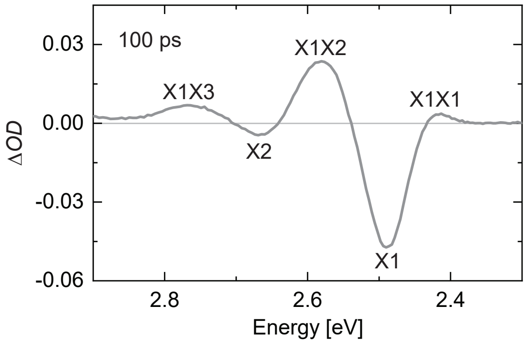

Figure 4.9: Comprehensive Interpretation of Transient Absorption Spectrum. TA spectrum at a delay time of 100 ps upon X1-resonant linear-polarized pumping. The negative signals are attributed to bleached excitonic transitions $|0\rangle \longrightarrow |\mathrm{X1}, \mathrm{X2}\rangle$, while the positive ones are induced biexcitonic transitions $|\mathrm{X1}\rangle \longrightarrow |\mathrm{X1X}i\rangle$ with $i = 1, 2, 3$.

4.4 Dynamics of Excitonic and Biexcitonic Transitions

So far, TA spectra have been analyzed at a delay time of 100 ps or 1 ps for circular-polarized pump and probe beams shown in Figure 4.5 and Figure 4.6. There, the earlier delay time was chosen because the spectral difference in the co- and counter-circular polarized cases only exists for a few ps limited by the decay in spin polarization.[211] In Figure 4.10a, a two-dimensional color plot of a TA measurement in the linear-polarization case is shown for delay times up to 2 ns. It is apparent that all features show almost identical dynamics throughout the measurement with an exponential decay time of ~2.6 ns. Normalized transients at the X1 and X2 bleaches, as well as the transient of the induced X1X2 absorption, are presented in Figure 4.10b. Their identical rise and overall dynamics further confirm that upon X1-resonant pumping, all bleached excitonic transitions $|0\rangle \longrightarrow |\mathrm{X}i\rangle$ and all induced biexcitonic transitions $|\mathrm{X1}\rangle \longrightarrow |\mathrm{X1X}i\rangle$ depend on the population of the X1 level, as illustrated in the level scheme in Figure 4.10c.

Note that the measurement shown in Figure 4.10a exclusively reflects the X1 exciton dynamics. In contrast, biexciton dynamics can only be monitored by the probe beam if they are already excited by the pump, i.e., for higher pump powers. This case is studied in detail in the following Chapter 5. In summary, the dynamics of the various TA signals further support the assignment of negative and positive peaks to bleached excitonic and induced biexcitonic transition, respectively, as all signals reflect the dynamics of the populated X1 exciton.

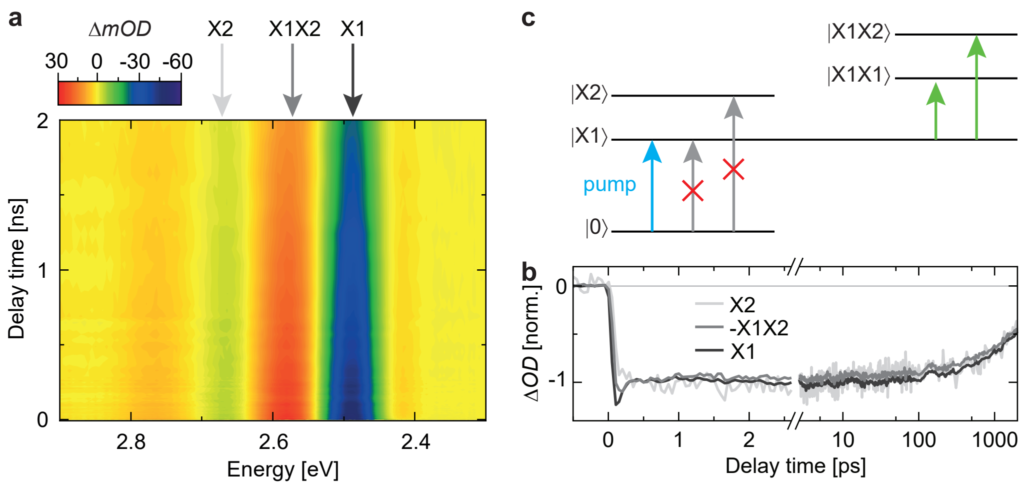

Figure 4.10: Transient Absorption Dynamics. **(a)** Two-dimensional color plot of a TA measurement upon resonant X1-pumping. The signals of the X1 and X2 bleach and the induced X1X2 absorption are labeled and **(b)** the corresponding transients are shown for comparison. **(c)** Level scheme illustrating the bleached excitonic transitions $|0\rangle \longrightarrow |\mathrm{X}i\rangle$ and the induced biexcitonic transitions $|\mathrm{X1}\rangle \longrightarrow |\mathrm{X1X}i\rangle$ upon pumping to the X1 level.

Generalization Across Quantum Dot Sizes and Compositions

In the course of this chapter, the absorption of spherical $CsPbBr_3$ QDs of various sizes has been analyzed. Through comparison with model calculations based on the weak and strong confinement models, the distinct absorption resonances were assigned to center-of-mass motion-confined excitons. TA spectroscopy on such QDs with a diameter of ~6.8 nm shows several negative and positive signals, which are attributed to bleached excitonic and induced biexcitonic transitions, respectively. This assignment is supported by the polarization-selective behavior and the temporal dynamics of the signals.

Figure 4.11 shows absorption and TA spectra of two additional $CsPbBr_3$ QD sizes (with diameter of ~4.7 nm and ~8.5 nm) and of other halide and cation compositions ($CsPbCl_3$ and $FAPbBr_3$). All absorption and TA spectra have qualitatively the same spectral shape as the $CsPbBr_3$ QDs studied above. It suggests that the established interpretation of absorption and TA spectra of $CsPbBr_3$ QDs are transferable to a wide range of spherical LHP QDs of different sizes and compositions. The results presented here build the basis for further studies by providing a comprehensive description of the energy levels and transitions in the ground and excited state, which are crucial for understanding the optical properties of LHP QDs.

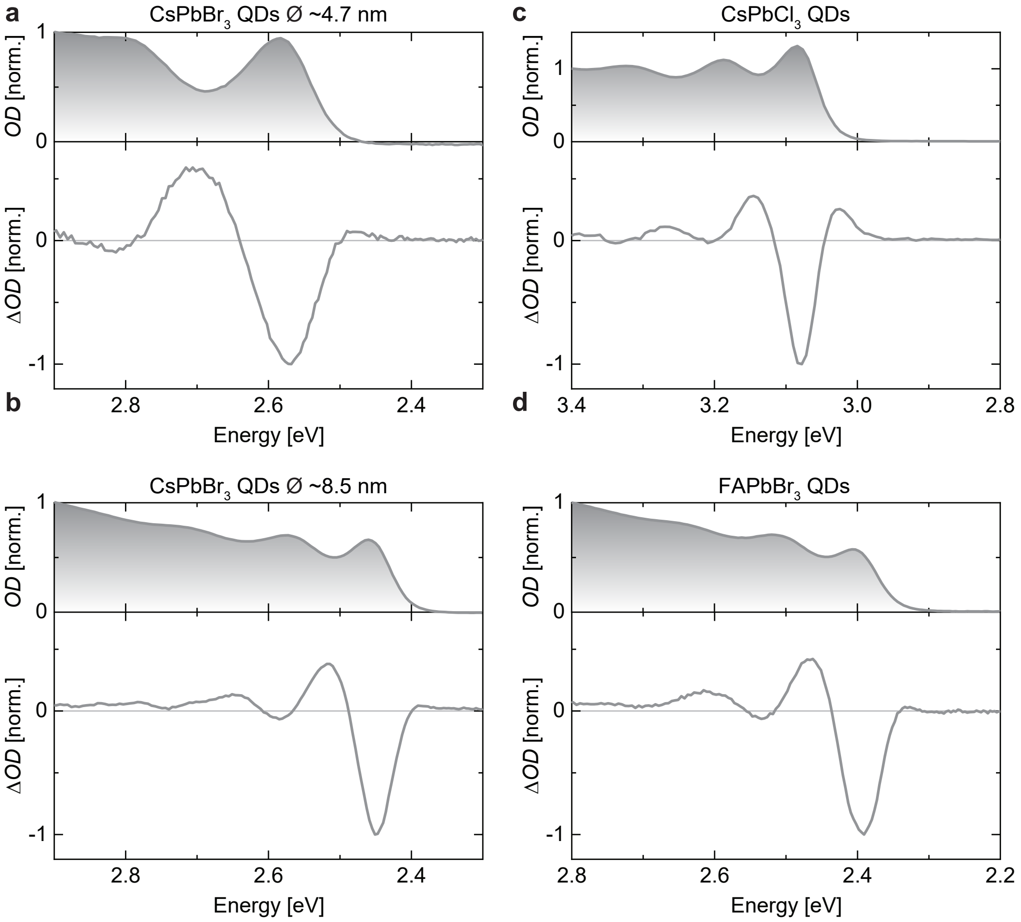

Figure 4.11: Size and Composition Dependent Absorption and Transient Absorption Spectra. Absorption and TA spectra of spherical CsPbBr$_3$ QDs with diameters of **(a)** ~4.7 nm and **(b)** ~8.5 nm, as well as of **(c)** CsPbCl$_3$ and **(d)** FAPbBr$_3$ QDs. The CsPbCl$_3$ data were acquired by Ahmet Tosun, while the synthesis and measurements for FAPbBr$_3$ were performed by Dr. Tushar Debnath.

5

Biexcitonic Optical Gain in $CsPbBr_3$ Quantum Dots

Conventional QDs like CdSe have been studied for decades with one of the goals being the integration of electrically pumped QDs as active material in highly efficient lasers.[24,25,118] However, in quantum confined systems, non-radiative Auger recombination is faster than in bulk, which limits optical gain in QDs, as discussed in Subsection 2.1.3.[25,112,117] This limitation is significantly reduced in conventional QDs, where the biexciton gain lifetime can be prolonged and the gain threshold lowered through core/shell engineering,[80,81,126] charging,[113,124] and doping.[212] The relatively new material class of LHP NCs, with its attractive light emitting properties, such as narrow emission linewidths,[138,150] near unity PLQYs,[51] and tunable emission spectra,[31,33] has also been studied for light amplification (see Subsection 2.2.3). LHP NCs exhibit ASE[160,161] and have been combined with various optical resonators for lasing.[48–50,162] Optimization of their light amplification properties is necessary toward their integration into real-world scalable lasing devices. Therefore, the underlying gain mechanism must be understood to enable targeted optimization. So far, larger NCs with close-lying energy levels and often large size inhomogeneities have mainly been studied, making it difficult to reach general conclusions.[51] The underlying optical gain mechanism is hence still discussed, and has been attributed to single-excitons,[160,165,166] trions,[167] and biexcitons.[114,161,163,164] The spherical $CsPbBr_3$ QDs studied in Chapter 4 provide a reliable platform for gaining comprehensive insights into their optical gain properties. Since these findings are largely unaffected by inhomogeneous broadening and reabsorption, they may be transferable to other $CsPbBr_3$ QDs.

This chapter is based on the main results of Reference 213. In Section 5.1, first, the ASE characteristics of spherical $CsPbBr_3$ QDs are determined with the setup discussed in Subsection 3.4.1. Power-dependent measurements reveal the ASE threshold, and, by employing the so-called variable stripe length (VSL) method (see Subsection 3.4.2), the net optical gain coefficient is determined. Subsequently, the underlying mechanism for optical gain in this material system is studied in Section 5.2 using power-dependent and time-resolved TA spectroscopy, as introduced in Subsection 3.3.3. Three key arguments are presented in support of biexcitonic optical gain: The gain threshold agrees with that expected for biexcitons, its TA signal spectrally overlaps with the energetically lowest biexciton, and the duration of the gain signal is limited by the biexciton lifetime.

5.1 Characterizing Amplified Spontaneous Emission

When testing a material for its light amplification properties and its potential to be used as a gain material, it is typically first checked if the sample exhibits ASE. For this purpose, $CsPbBr_3$ QDs with DDAB as ligands were chosen, as the shorter alkyl chain length of DDAB in comparison to lecithin (which was used in Chapter 4) allows a higher packing density of QDs in films. Steady-state optical properties of such QDs in solution are shown in Figure 5.1 indicating their monodispersity evident from the distinct absorption resonances (compare also with Figure 4.2a). By fitting Gaussian peaks to the absorption spectrum (as shown in Figure A.2 in the Appendix), a FWHM of ~81 meV can be extracted for the X1 absorption resonance. Furthermore, a Stokes shift of ~40 meV is determined, which is similar to literature values.[210,214]

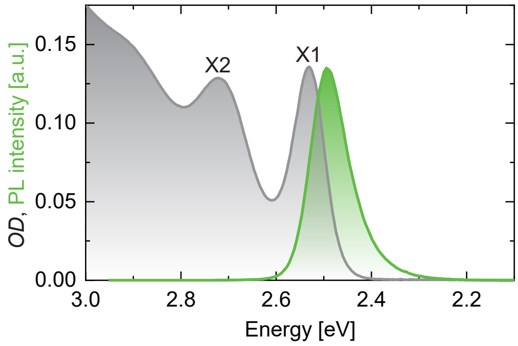

Figure 5.1: Steady-State Optical Spectra. Steady-state absorption and PL spectrum of spherical $CsPbBr_3$ QDs dispersed in octane with a diameter of ~6 nm and DDAB as ligands. The two energetically lowest absorption resonances corresponding to X1 and X2 are indicated.

ASE measurements were carried out on $CsPbBr_3$ QDs dropcasted on a Si substrate using the setup detailed in Subsection 3.4.1. The QD film is excited with 400 nm light that is focused to a rectangular focus spot, and the edge-emitted light is collected in a 90° angle. The excitation fluence is gradually increased from 11–213 $\mu J/cm^2$ at a constant stripe length of ~2.4 mm, yielding the spectra shown in Figure 5.2. For low excitation fluences only the PL originating from spontaneous emission is observed, which increases with fluence. Above a certain threshold fluence, an additional peak arises around 2.39 eV, exhibiting a significantly lower FWHM of ~20 meV compared to the initial PL width of ~100 meV. Furthermore, its intensity increases faster with excitation fluence, and it gradually redshifts by up to 10 meV.[160,163] Due to the narrow linewidth and the rapid increase with excitation fluence, this additional signal is attributed to ASE (see also Subsection 2.2.3).[25]

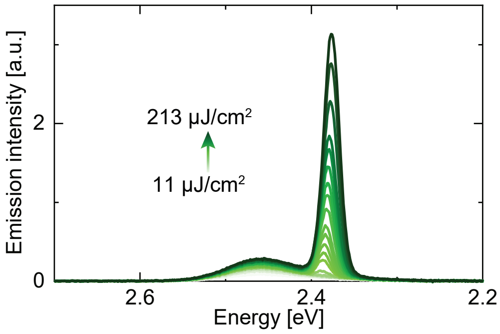

Figure 5.2: Amplified Spontaneous Emission Measurement. Emission spectra for different excitation fluences of 11–213 μJ/cm² that show increasing spontaneous emission and above a certain threshold fluence additionally ASE.

In literature, the origin of ASE in LHP NCs has been attributed to biexciton,[114,161,163,164] trion,[167] or single-exciton gain.[160,165,166] The redshift of the ASE peak compared to the PL of initially ~70 meV is attributed, depending on the appointed gain origin, to the biexciton binding energy, the trion binding energy, or strong reabsorption, respectively. Identifying the origin of the optical gain from ASE spectra alone is not reliable; hence TA spectroscopy was employed, which is discussed in Section 5.2. But first, the ASE data is analyzed in more detail to reveal the potential of the spherical $CsPbBr_3$ QDs for net light amplification.

Two requirements for ASE are highlighted. The excitation fluence must be sufficient to achieve a population inversion in the QDs, thereby putting them into an optical gain state.[25] The specific threshold fluence for the $CsPbBr_3$ QD film investigated here, is determined in the following in Subsection 5.1.1. Furthermore, the illuminated stripe must be long enough to allow for sufficient build up of ASE to overcome losses.[168] This is characterized by the net optical gain coefficient, determined in Subsection 5.1.2 using the VSL method.

5.1.1 Determining the Threshold

The ASE threshold marks the excitation fluence at which ASE is detected in addition to spontaneous emission (see also Subsection 2.2.3). To determine the threshold fluence for the film of spherical $CsPbBr_3$ QDs, the power series shown in Figure 5.2 is further analyzed. The intensity around the ASE peak (2.35–2.41 eV) is spectrally integrated and plotted as a function of the excitation fluence in Figure 5.3. Two regions with distinct slopes are apparent in the data, with their transition marking the onset of ASE. Linear fits to the respective regions intersect at a fluence of ~58 µJ/cm², which defines the ASE threshold.

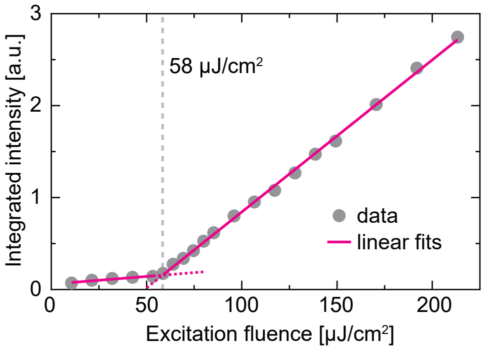

Figure 5.3: Amplified Spontaneous Emission Threshold Determination. Integrated intensity around the ASE peak (see Figure 5.2) as a function of excitation fluence. The ASE threshold is determined by the intersection point of the linear fits (pink lines) to the two distinct slopes. The pink dotted lines are extensions of the linear fits, highlighting the intersection point.

Note that the threshold value strongly depends on the spot size used to calculate the fluence (see also Equation 3.20). Whether defining the length of the rectangular focus spot along the short side via an intensity drop of $1/2$, $1/e$, or $1/e^2$ (as detailed in Figure 3.7), the resulting threshold values vary from 99 over 83 to 58 µJ/cm². In literature, it is typically not described how the spot size was determined, which makes a reliable comparison of threshold values difficult. Details in the analysis, such as the fit function, also influence the determined values.[166] Nevertheless, ASE threshold values of only a few µJ/cm² are reported for $CsPbBr_3$ NCs, in some cases using additional passivation techniques.[160,167,215–217]

5.1.2 Net Optical Gain Coefficient

In the VSL method, the stripe length of the rectangular laser spot illuminating the sample is varied (see Subsection 3.4.2 for details). An exponential increase in the detected intensity as a function of the stripe length indicates ASE. In this regime, stimulated emission becomes the dominant process over optical losses,[168] such as reabsorption or scattering on impurities.[62] The net optical gain coefficient G (see Equation 2.13) characterizes the stripe length at which this transition to net optical gain occurs. Hence, it is a key parameter to evaluate a system's potential for net light amplification.

Figure 5.4 shows the integrated ASE intensity (PL background corrected as detailed in Subsection 3.4.2) as a function of the stripe length. Fitting Equation 3.22 to the onset of the data points exhibits the net optical gain coefficient $G = 93\,\text{cm}^{-1}$. This fit function can be modified for data that are not corrected for background PL and even further extended to include saturation of the optical gain. It is reported that the choice of the fit function can strongly influence the obtained value of G.[166] While for other systems, such as CdSe nanoplatelets (NPLs), a giant value of $6600\ \mathrm{cm}^{-1}$ has been achieved,[218] for $CsPbBr_3$ NCs, values of up to ~$450\ \mathrm{cm}^{-1}$ are typically reported.[25,160] Here, the VSL measurements were performed at an excitation fluence of $107\ \mu\mathrm{J/cm^2}$, corresponding to almost double the threshold fluence. Since G increases with the used laser power,[212,218] it is expected that higher values could also be achieved for the spherical $CsPbBr_3$ QD film. Furthermore, film formation parameters such as the packing density and surface roughness can strongly influence ASE, as the buildup of ASE is supported by the film acting as a waveguide (see also Subsection 2.2.3).[166,219,220]

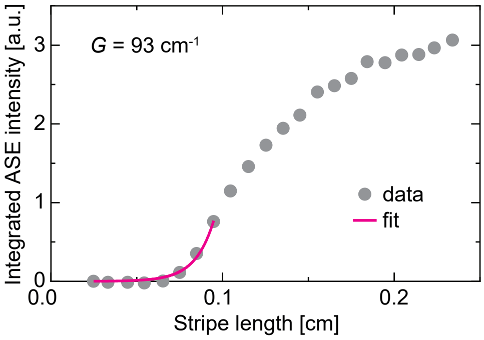

Figure 5.4: Net Optical Gain Coefficient Determination. Integrated ASE intensity as a function of stripe length. The net optical gain coefficient G is determined by fitting the data onset with Equation 3.22 (pink line).

Both the ASE threshold of ~$58\ \mu\mathrm{J/cm^2}$ and the net optical gain coefficient $G = 93\ \mathrm{cm}^{-1}$ deviate by roughly an order or magnitude from record values reported for LHP NCs.[25,160,167,215–217] However, given that no significant optimization was applied to the QD film, these values still demonstrate competitive performance, highlighting the high potential of the spherical $CsPbBr_3$ QD for light amplification.

By analyzing the ASE data alone, the origin of the underlying optical gain cannot be reliably determined. Upon illumination with high fluences, both the energy levels of the X1 exciton and the X1X1 biexciton are excited in the QD ensemble due to Poisson statistics (see Equation 2.8). Stimulated emission can therefore occur from both levels, raising the question of which transition is responsible for the optical gain that leads to the observed ASE signal. In the following, spherical $CsPbBr_3$ QDs are investigated using TA spectroscopy, revealing that their optical gain originates from the population of the X1X1 biexciton level.

5.2 Three Aspects Supporting Biexcitonic Optical Gain

After demonstrating the light amplification potential of spherical $CsPbBr_3$ QD in a film, the underlying optical gain mechanism is investigated using TA spectroscopy. Gain studies on QD films are typically strongly influenced by reabsorption.[165,166] Therefore, the gain properties of the spherical QDs are studied here in a dilute colloidal dispersion to avoid influences from reabsorption and other film formation factors. In literature, optical gain in $CsPbBr_3$ NCs has been attributed to various origins: biexcitons,[114,161,163,164] trions,[167] and single excitons with strong reabsorption.[160,165,166] The distinct absorption and TA resonances of the spherical $CsPbBr_3$ QDs enable an effective investigation of their energy levels, building on the insights gained about their energy landscape in Chapter 4.

Optical gain is evidenced by the appearance of a negative OD signal. The absorption spectrum of $CsPbBr_3$ QDs in the ground state is represented by the gray line in Figure 5.5. The nonlinear absorption of the QDs in the corresponding excited state is obtained by $OD + \Delta OD$ (see Equation 3.14).[203] The colored lines in Figure 5.5 display $OD + \Delta OD$ at a delay time of 8 ps upon pumping with 400 nm light at varying excitation powers, given in units of the average number $\langle N \rangle$ of excitons created per QD (see Subsection 3.3.3). The spectra at lower $\langle N \rangle$ show bleaching of excitonic transitions and induced biexcitonic absorption, according to the model developed in Section 4.3. For increasing $\langle N \rangle$, an additional negative signal appears in the low-energy tail of the spectra. This negative absorption signal indicates optical gain.[112]

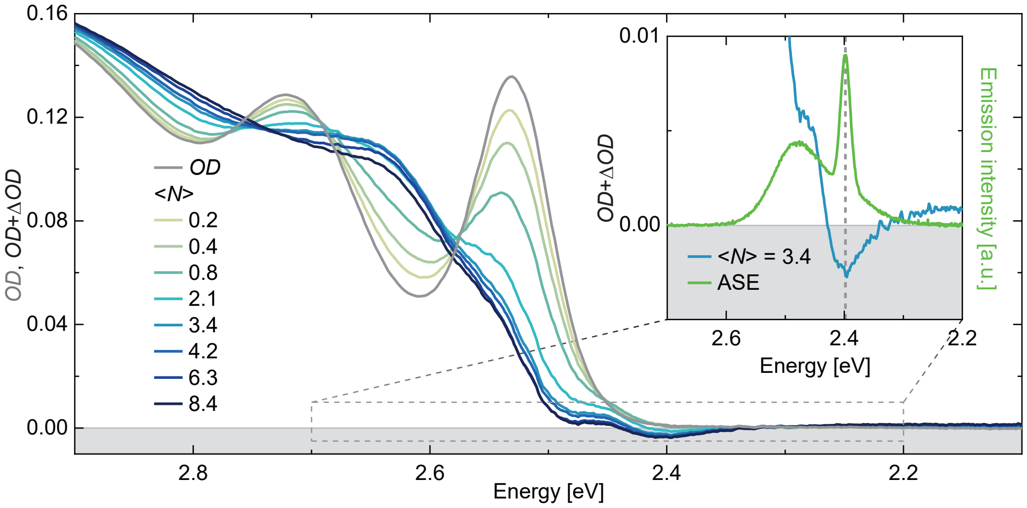

Figure 5.5: Optical Gain in the Excited State. Absorption of the ground state (OD, gray line) and absorption of the excited state ($OD + \Delta OD$, colored lines) upon 400 nm pumping at different $\langle N \rangle$ after a delay time of 8 ps. The inset shows a zoom-in to the marked range comparing $OD + \Delta OD$ at $\langle N \rangle = 3.4$ (blue line) to an emission spectrum of the same batch of QDs showing ASE (green line). The gray shaded area highlights the regime of $OD + \Delta OD < 0$.

As ΔOD is obtained from TA measurements performed on a dilute dispersion of QDs, the sample in this configuration does not exhibit ASE itself. It is essential to verify that the observed gain signature corresponds to the ASE signal by using the exact same QDs. Therefore, QDs of the same synthesis batch are used to compare the spectral position of the ASE and the gain signal, as shown in the inset of Figure 5.5. $OD + \Delta OD$ for $\langle N \rangle = 3.4$ clearly shows the negative signature of optical gain. Its spectral position coincides with the ASE peak at ~2.4 eV, which was measured in the same way as in Section 5.1. This agreement demonstrates that the optical gain signature is indeed responsible for the ASE in the respective measurement.[25] Hence, identifying the mechanism of the observed optical gain signal also reveals the origin of the ASE. In the course of this section, three key arguments are presented that support the assignment to biexcitonic optical gain.

5.2.1 Gain Threshold Indicates Biexcitons

To determine the origin of the optical gain, first, the gain threshold is determined in units of $\langle N \rangle$. For this purpose, the normalized absorption changes $\frac{|\Delta OD|}{OD}$ at the gain feature ~2.4 eV at a delay time of 5 ps are analyzed. In Figure 5.6, the decadic logarithm of $\frac{|\Delta OD|}{OD}$ is plotted as a function of $\langle N \rangle$. In this representation, a heuristic fit of $f(x) = a \cdot \exp(-b \cdot x) + c$ reproduces the data points well, and its intersection point with the zero line indicates the onset of $|\Delta OD| > OD$ (for $\Delta OD < 0$) and thus the emergence of optical gain.[112,126] Here, a threshold value of $\langle N \rangle_{\text{th}} = 0.99$ is determined.

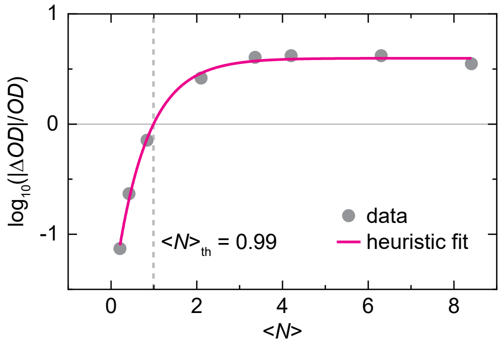

Figure 5.6: Optical Gain Threshold Determination. Decadic logarithm of normalized absorption changes at the gain feature at a delay time of 5 ps as a function of $\langle N \rangle$. The intersection point of the heuristic fit (pink line) with the zero line indicates the optical gain threshold $\langle N \rangle_{\text{th}}$.

Theoretical calculations considering Poisson statistics predict a threshold value of $\langle N \rangle_{\text{th}} = 0.69$ for single-exciton gain and $\langle N \rangle_{\text{th}} = 1.15$ for biexciton gain without a biexciton binding energy, as discussed in Subsection 2.1.3.[113] In the case of biexciton gain with a nonzero biexciton binding energy, these values represent lower and upper bounds for the gain threshold, respectively. Here, an attractive biexciton binding energy of $E_{\text{b,XX}} = 68$ meV is extracted from the TA spectrum shown in Figure 5.7a, which is consistent with literature.[114,128] Accordingly, $\langle N \rangle_{\text{th}} < 1.15$ is expected. $\langle N \rangle_{\text{th}} = 0.69$ corresponds to the limiting case of $E_{\text{b,XX}}$ exceeding the ensemble linewidth, so that stimulated emission $|\text{X1}\rangle \longrightarrow |0\rangle$ does not spectrally overlap with absorption $|\text{X1}\rangle \longrightarrow |\text{X1X1}\rangle$. In this case, single-exciton optical gain is enabled, which otherwise leads to net transparency (see Subsection 2.1.3).[126,128] However, the measured $E_{\text{b,XX}} = 68$ meV is smaller than the FWHM of ~81 meV extracted from Figure 5.1 (as shown in Figure A.2 in the Appendix). Therefore, the interpretation of biexcitonic gain is consistent with the determined $\langle N \rangle_{\text{th}} = 0.99$, which lies between the two theoretical limits.

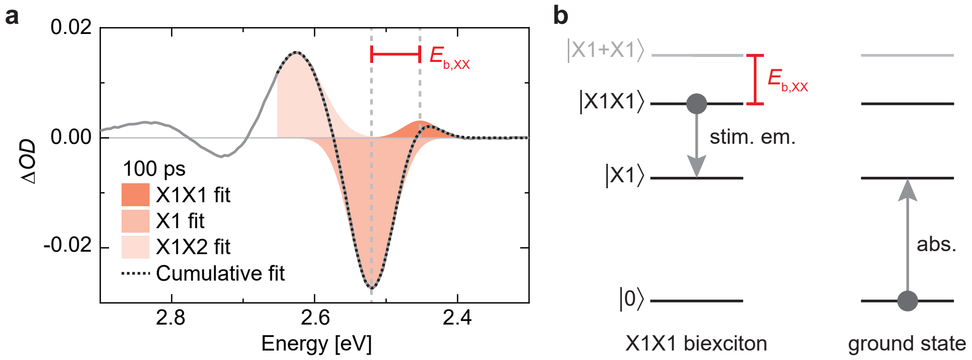

Figure 5.7: Biexciton Binding Energy Promoting Optical Gain. **(a)** Determination of the biexciton binding energy $E_{\mathrm{b,XX}}$ via Gaussian fitting to a TA spectrum at a delay time of 100 ps upon 400 nm pumping with $\langle N \rangle = 0.4$. **(b)** Level scheme illustrating the energetic shift between stimulated biexciton emission $|\mathrm{X1X1}\rangle \longrightarrow |\mathrm{X1}\rangle$ and ground state absorption $|0\rangle \longrightarrow |\mathrm{X1}\rangle$ due to $E_{\mathrm{b,XX}}$.

Figure 5.7b illustrates how the biexciton binding energy reduces the spectral overlap and hence the competition between stimulated biexciton emission $|\mathrm{X1X1}\rangle \longrightarrow |\mathrm{X1}\rangle$ and ground state (re)absorption $|0\rangle \longrightarrow |\mathrm{X1}\rangle$ in QD ensembles.[114] In the following, TA spectra upon excitation with $\langle N \rangle > \langle N \rangle_{\mathrm{th}}$ are studied to get further information about the optical gain.

5.2.2 Spectral Overlap with Biexciton Signal

The spectral position of the optical gain signal can provide further insight into its origin. For this purpose, ΔOD is now directly studied instead of the nonlinear absorption $OD + \Delta OD$. TA spectra are shown in Figure 5.8a at delay times of 6.3 ps and 100 ps upon 400 nm pumping with $\langle N \rangle = 3.4$. The spectral shape is qualitatively the same for the two delay times except for the low-energy part. The similarity indicates that the QDs are stable towards such high exciton densities and that their overall energy landscape is preserved for the considered time scales. At 100 ps time delay, the expected induced X1X1 biexciton absorption is observed (see Section 4.3). This is also visible upon pumping with $\langle N \rangle = 0.2$ for both delay times, as shown in Figure 5.8b. However, this induced X1X1 absorption feature is not visible for $\langle N \rangle = 3.4$ at a delay time of 6.3 ps. Instead, an additional negative signal at 2.4 eV is observed that corresponds to the optical gain (compare also with Figure 5.5).

The spectral position of the induced X1X1 absorption and the gain signal is determined by Gaussian fitting. The former is extracted from the spectrum at 100 ps time delay, where the fits are qualitatively similar to those shown in Figure 5.7. The gain signal is analyzed in Figure 5.8c at 6.3 ps time delay. The resulting fits to the induced X1X1 absorption and the gain signal are shown together in Figure 5.8d. It is apparent that they overlap spectrally, indicating that they are both related to biexcitons. However, the gain signal is redshifted relative to the X1X1 signal by ~56 meV.

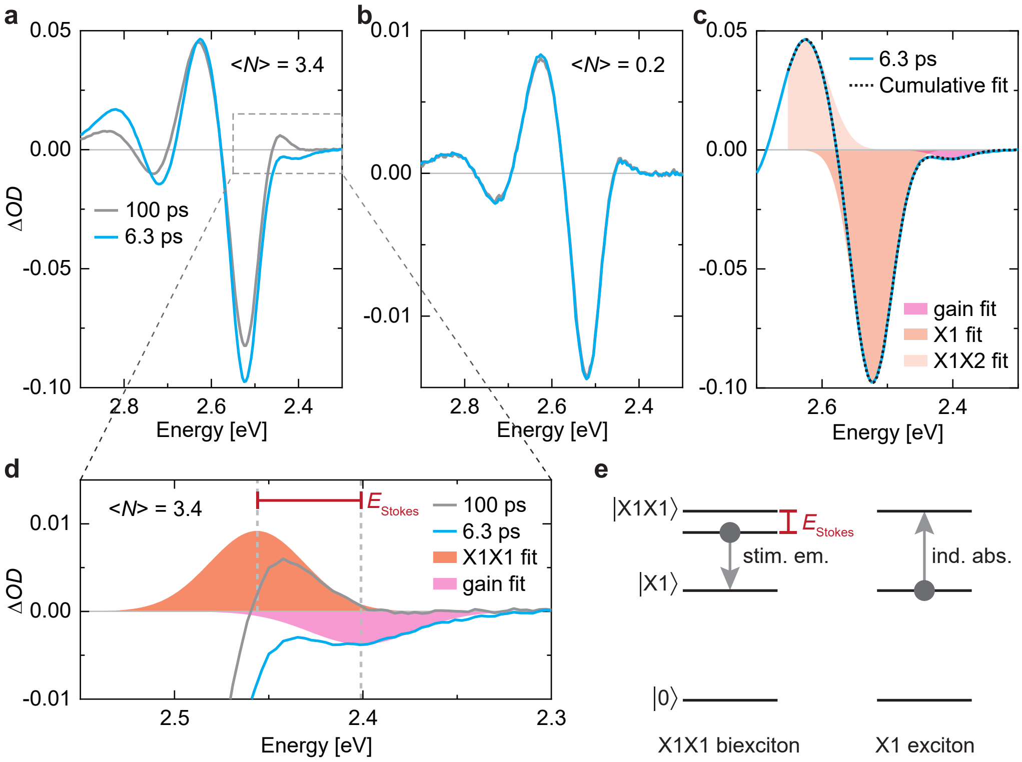

Figure 5.8: Spectral Position of Optical Gain and Stokes Shift. **(a)** TA spectra at delay times of 6.3 ps (blue line) and 100 ps (gray line) upon 400 nm pumping with $\langle N \rangle = 3.4$ and **(b)** with $\langle N \rangle = 0.2$. **(c)** Gaussian fits to the spectrum from **a** at 6.3 ps time delay upon $\langle N \rangle = 3.4$. **(d)** Comparison of the fits to the X1X1 signal (orange shaded area) and the gain signal (pink shaded area). **(e)** Level scheme illustrating the Stokes shift E_{Stokes} between the stimulated emission $|\text{X1X1}\rangle \longrightarrow |\text{X1}\rangle$ and induced absorption $|\text{X1}\rangle \longrightarrow |\text{X1X1}\rangle$.

In general, perovskite NCs exhibit a size-dependent Stokes shift,[221] which has been attributed to various phenomena: from extrinsic processes like reabsorption[207] to intrinsic effects such as a confined hole state[208] or polaron formation.[209,210] The spherical CsPbBr$_3$ QDs studied here also show a Stokes shift of ~40 meV (see Figure 5.1). A comparable Stokes shift can therefore be expected for biexcitons and higher multi-excitons.[222] This is indeed beneficial for optical gain, as it reduces the overlap between competing processes,[128] illustrated in Figure 5.8e, where the stimulated emission $|\text{X1X1}\rangle \longrightarrow |\text{X1}\rangle$ is shifted relative to the induced absorption $|\text{X1}\rangle \longrightarrow |\text{X1X1}\rangle$ by E_{Stokes}. So far, both the gain threshold and its spectral position support the interpretation of biexcitonic optical gain. In the following, the temporal behavior of the gain signal is studied and compared to the biexciton dynamics.

5.2.3 Gain Duration Limited by Biexciton Lifetime

A certain temporal dynamic of the gain signal was already observed in Figure 5.8a, with gain only visible at a delay time of 6.3 ps, but not at 100 ps. A more detailed analysis of the gain duration and its dependence on $\langle N \rangle$ is provided in the following. The nonlinear absorption $OD + \Delta OD$ is investigated for different $\langle N\rangle$, with the corresponding transients at the gain position at 2.4 eV presented in Figure 5.9. The gray shaded area highlights the regime of negative $OD + \Delta OD$, which corresponds to optical gain. It is again apparent that measurements with $\langle N\rangle < \langle N\rangle_{\text{th}}$ do not exhibit gain. For transients with $\langle N\rangle > \langle N\rangle_{\text{th}}$, the delay time at which the signal becomes negative indicates the start of the optical gain, while the delay time at which the signal returns to positive values defines the end of the gain.

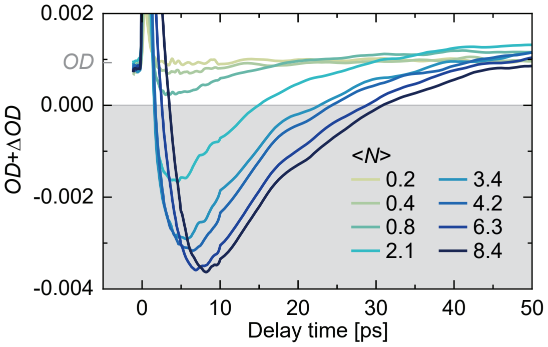

Figure 5.9: Optical Gain Dynamics. Transients of the nonlinear absorption $OD + \Delta OD$ (data smoothed) at the gain signal at 2.4 eV for different $\langle N\rangle$. The gray shaded area highlights the regime of $OD + \Delta OD < 0$, corresponding to optical gain. The constant offset, particularly visible at negative delay time where $\Delta OD \approx 0$, is the constant contribution of $OD \approx 0.001$.

As the gain threshold and its spectral position have already indicated biexcitonic gain, its temporal behavior is now compared to biexcitons. For this purpose, X1 transients at 2.52 eV are analyzed for different $\langle N\rangle$, as shown in Figure 5.10, where transients for $\langle N\rangle = 0.2$ and $\langle N\rangle = 8.4$ are displayed, normalized to a late delay time of 3.4 ns. The inset shows the normalized transients for all measured $\langle N\rangle$ with an additional y-axis offset for clarity. The pink lines are exponential fits with the resulting time constants listed in Table 5.1.

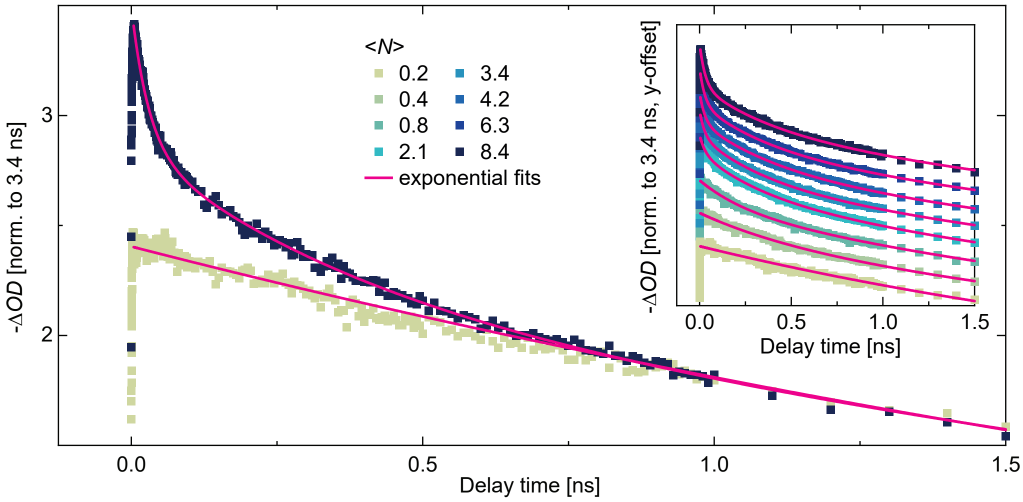

Figure 5.10: Biexciton Dynamics. TA transients at 2.52 eV upon 400 nm pumping with different $\langle N\rangle$, normalized to a delay time of 3.4 ns and, in the inset, with an additional y-offset.

The monoexponential fit to $\langle N\rangle = 0.2$ with a time constant of $\tau_1 \approx 4\,\mathrm{ns}$ is attributed to the lifetime of the X1 exciton (compare also with Figure 4.10).[31,223] A similar τ_1 is observed for all measured $\langle N\rangle$ (see Table 5.1), explaining the similar slope for all transients at long delay times, visible in the inset in Figure 5.10. With increasing $\langle N\rangle$ additional exponential components arise that are signatures of multi-excitons.[117]

$\langle N\rangle$	τ_1[ps]	τ_2[ps]	τ_3[ps]
0.2	3521	-	-
0.4	4204	494	-
0.8	3769	258	-
2.1	3888	339	30
3.4	4084	348	27
4.2	4224	401	29
6.3	4177	365	28
8.4	4137	366	30

Table 5.1: Exponential Fitting Time Constants. Time constants $\tau_{1,2,3}$ resulting from the exponential fits to the TA transients upon excitation with different $\langle N\rangle$, shown in Figure 5.10.

The transient with $\langle N\rangle = 8.4$ in Figure 5.10 clearly shows a fast decay component at early delay times with a determined time constant $\tau_3 = 30\,\mathrm{ps}$. A similar component is observed in all measurements with $\langle N\rangle \geq 2.1$ that is, notably, $\langle N\rangle > \langle N\rangle_{\mathrm{th}}$, thus suggesting a connection to the gain. This decay component can be attributed to biexcitons, as τ_3 is comparable to biexciton lifetimes reported in literature.[114,159,188,214] The biexciton lifetime $\tau_{\mathrm{XX}} = \tau_3$ is plotted as a function of $\langle N\rangle$ in Figure 5.11a. As shown in Table 5.1, τ_{XX} is constant, with an average of $\tau_{\mathrm{XX,avg}} = 28.8\,\mathrm{ps}$ determined by a constant fit. This is compared to the gain duration τ_{gain} extracted from Figure 5.9 as the time difference between the end and the start of the optical gain. The data points are reproduced by a heuristic fit of $f(x) = a + b \cdot \left(1 - \exp\left(\frac{c-x}{d}\right)\right)$, demonstrating that the gain duration saturates at $\tau_{\mathrm{gain,sat}} = 27.7\,\mathrm{ps}$. This value is comparable to $\tau_{\mathrm{XX,avg}} = 28.8\,\mathrm{ps}$, indicating that the gain duration is limited by the biexciton lifetime.

From TA data alone, it is not apparent whether the determined biexciton lifetime is dominated by spontaneous emission or exciton-exciton annihilation. Nevertheless, both decay processes, radiative and non-radiative, respectively, contribute to the depopulation of the biexciton level, thus competing with stimulated emission from this level, limiting the optical gain. This is illustrated in the level scheme in Figure 5.11b. The energetic shifts by $E_{\mathrm{b,XX}}$ and E_{Stokes} reduce the competition of stimulated emission $|\mathrm{X1X1}\rangle \longrightarrow |\mathrm{X1}\rangle$ with other transitions in the QD ensemble, such as ground state absorption $|0\rangle \longrightarrow |\mathrm{X1}\rangle$ and induced absorption $|\mathrm{X1}\rangle \longrightarrow |\mathrm{X1X1}\rangle$, respectively (see Figure 5.7 and Figure 5.8). Although this benefits

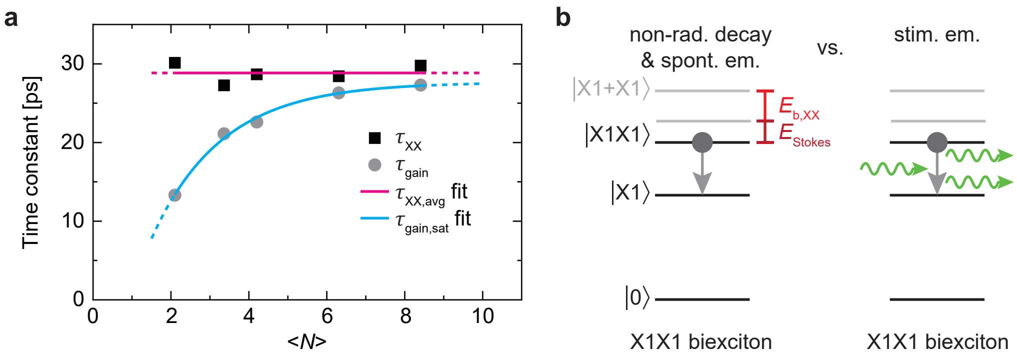

Figure 5.11: Comparison of Gain Duration and Biexciton Lifetime. (a) Time constants for the biexciton lifetime τ_{XX} (black squares) and the gain duration τ_{gain} (gray circles) as a function of $\langle N \rangle$. A constant fit to τ_{XX} (pink line) yields the average biexciton lifetime $\tau_{XX,avg}$, while a heuristic fit to τ_{gain} (blue line) determines the saturated gain duration $\tau_{gain,sat}$. The pink and blue dotted lines are extensions of the respective fits. **(b)** Level scheme, including the energetic shifts from $E_{b,XX}$ and E_{Stokes}, that illustrates the radiative and non-radiative processes depopulating the X1X1 biexciton level and thereby limiting stimulated emission.

the optical gain,[128] the population of the biexciton level remains the limiting factor for the optical gain.

Note that in Figure 5.10, transients with $\langle N \rangle \geq 0.4$ show an additional decay component τ_2 of a few hundred ps. According to literature, τ_2 might be a signature of trions,[224,225] which have also been reported as a source of optical gain.[167] However, this can be excluded for the present case for several reasons: The τ_2 component is already observed for $\langle N \rangle < \langle N \rangle_{th}$. Furthermore, the determined $\langle N \rangle_{th}$ is higher than the threshold expected for trions (see Subsection 2.1.3). Moreover, the trion binding energy in $CsPbBr_3$ NCs is lower than the biexciton binding energy,[226,227] but the gain signal overlaps spectrally with the low-energy side of the X1X1 biexciton signal (see Figure 5.8d). Finally, τ_2 of a few hundred ps is much longer than the gain duration saturating at $\tau_{gain,sat} = 27.7\,\text{ps}$. Trion gain can therefore be excluded, underlining biexcitonic optical gain as the underlying mechanism.

Determined Biexcitonic Gain Provides Strategies for Future Optimization

In this chapter, three key arguments have been presented supporting biexcitons as the origin of the optical gain and the resulting ASE signal of the studied spherical $CsPbBr_3$ QDs. The gain threshold of $\langle N \rangle_{th} = 0.99$ along with $E_{b,XX} = 68\,\text{meV}$ aligns well with the expected value for biexcitons with a nonzero binding energy. The position of the gain signature in TA spectra overlaps with the X1X1 biexciton signal, considering a reasonable Stokes shift of $E_{Stokes} = 56\,\text{meV}$. Furthermore, the duration of the optical gain with $\tau_{gain,sat} = 27.7\,\text{ps}$ is limited by the biexciton lifetime $\tau_{XX,avg} = 28.8\,\text{ps}$, highlighting the required population of the X1X1 biexciton level as prerequisite for the optical gain.

This insight into biexcitonic optical gain in spherical $CsPbBr_3$ QDs not only deepens the understanding of this specific material system, but also likely reflects an intrinsic property of

$CsPbBr_3$ NCs in general. The high quality of the QDs minimizes inhomogeneous broadening, while the use of highly dilute colloidal dispersions instead of relatively thick films reduces reabsorption within the QD ensemble. Understanding the underlying gain mechanism also paves the way for future optimization of their light amplification properties. The ASE threshold can be improved to some extent by optimizing film formation parameters, such as the packing density by the choice of ligands[216] or substrate functionalization.[228] Furthermore, the homogeneity of the film can be improved by incorporating the QDs in SiO_2 spheres[229] or polymers.[219]

However, the fundamental limit for reducing the ASE threshold is related to the threshold of the underlying optical gain. Therefore, in the present case of biexcitonic gain, it can be improved by either prolonging the biexciton lifetime or by utilizing another gain mechanism that has an intrinsically lower threshold. The former can be achieved to a certain degree by using larger NCs, as the non-radiative biexciton decay rate follows a universal volume scaling (see Subsection 2.2.3).[214,230,231] This has been demonstrated for larger cubic $CsPbBr_3$ NCs with edge lengths of ~10 nm, which exhibit ASE threshold fluences an order of magnitude lower than the value determined here.[160,216] However, the application of this method is limited and reduces the degree of confinement in the system, ultimately leading to bulk-like properties.[232] Understanding the underlying gain mechanism in $CsPbBr_3$ QDs allows for targeted optimization of limiting processes. As discussed for conventional QDs in Subsection 2.1.3, several methods can be used to significantly lower the gain threshold, such as core/shell engineering,[80,81,126] charging,[113,124] and doping of QDs.[212]

With the light amplification potential and the underlying optical gain mechanism of the spherical $CsPbBr_3$ QDs being established, future work can now be directed toward building a laser with them. In order to ultimately achieve efficient lasing, in addition to a low optical gain threshold of the gain material, the cavity is also crucial. Resonator geometries previously used for LHP NCs can serve as a starting point, e.g., by using whispering gallery modes[160,161,233,234] or vertical cavity surface-emitting lasers.[235–237]

6

Summary, Conclusions, and Outlook

In this thesis, I have studied lead halide perovskite (LHP) quantum dots (QDs) focusing on their steady-state absorption, excited-state dynamics, and light amplification properties. A unique feature of this material class, compared to conventional II-VI and III-V semiconductors, is that their optical properties are dominated by a single conduction band and valence band around the band gap, without heavy hole/light hole degeneracies.[51] This reduces the complexity of optical spectra around the band gap, allowing a clearer distinction between individual energy levels of QDs. However, precise control over the size of the QDs during synthesis remains challenging, leading to inhomogeneous broadening in QD ensembles. Recently, a new synthesis method was developed that yields monodisperse spherical LHP QDs by separating nucleation from growth.[54] I utilize such spherical LHP QDs with sizes comparable to the exciton Bohr diameter to gain insight into their ground and excited state energy landscape.[193] Furthermore, I investigate their light amplification properties, revealing biexcitonic optical gain as the underlying gain mechanism.[213] These topics have been discussed in detail in the results chapters. In the following, the main findings and their implications for future work are summarized; first, regarding confined excitons and biexcitons in LHP QDs, and second, the biexcitonic optical gain in $CsPbBr_3$ QDs.

Confined Excitons and Biexcitons in Lead Halide Perovskite Quantum Dots

The novel monodisperse spherical LHP QDs exhibit several distinct absorption resonances.[54] I compare their energetic positions with model calculations for weak and strong confinement.[53] The latter is the typical case for most conventional II-VI QDs, where the electron and hole are individually confined before including Coulomb interaction.[67] For spherical $CsPbBr_3$ QDs with diameters ranging from ~5–12 nm, I find good agreement with the **weak confinement model**, where hydrogen-like excitons are confined as a whole by the QD potential. For sizes larger than the exciton Bohr diameter of ~6.1 nm, this result is expected. Notably, the model still closely reproduces the energies of the absorption resonances for QD sizes comparable to the Bohr diameter. Therefore, I assign the energy levels observed in steady-state absorption to **hydrogen-like excitons confined in their center-of-mass motion**. This provides a simplistic and intuitive model to describe the energy landscape that governs the optical properties of the LHP QDs and enables the study of their excited state, which I examine using TA spectroscopy.

In TA measurements of the spherical LHP QDs, I observe a multitude of spectral features. The negative signals coincide spectrally with the steady-state absorption resonances, while the positive signals are redshifted relative to the negative ones. The absorption of the excited state and the resulting TA spectrum can be modeled using the measured ground-state absorption spectrum.[192,203–205] In my model, the following processes are considered: Due to the delocalization of the pumped exciton across the entire QD, which has a size similar to the exciton Bohr diameter, the probe beam cannot create a second independent exciton, resulting in **bleached excitonic transitions**. Instead, when the Coulomb interaction is included, the probe beam monitors **induced transitions to biexcitonic levels**. These biexcitonic transitions are redshifted relative to the excitonic transitions by the biexciton binding energy of ~40 meV for QDs with diameters of ~6.8 nm. Furthermore, stimulated emission from the populated X1 exciton is included, which is polarization dependent and occurs from a ~35 meV Stokes-shifted energy level. Additionally, the polarization-selective excitation of the energetically lowest biexciton X1X1 is considered, which aligns with the expected behavior.[128,202] The TA spectrum modeled with these considerations closely reproduces the measured spectra, suggesting that the most relevant processes are included. The temporal dynamics of the TA signals further confirm my assignment of the dominant processes to bleached excitonic and induced biexcitonic transitions, all of which resemble the dynamics of the X1 exciton.

My interpretation of the absorption and TA spectra has provided a basis for various studies on these spherical LHP QDs. So far, they have been applied to photoluminescence (PL) quenching,[223] manganese doping,[238] and energy transfer studies.[239] This highlights how my results contribute to the active field of light-emitting devices including LEDs and displays,[15,37,38,240–244] as well as lasing devices.[48–50] Having identified the QDs to be in the weak confinement regime makes them potential candidates for another interesting field of research. As recently shown in large cubic $CsPbBr_3$ QDs, the coherent motion of weakly confined excitons extending over many unit cells can lead to a giant oscillator strength and single-photon superradiance.[66] The larger spherical LHP QDs studied here could also be suitable to observe this effect. It further highlights the potential of the system for quantum light generation.[44–47] Based on my interpretation of the energy levels in the ground and excited state of spherical $CsPbBr_3$ QDs, I investigate their light amplification properties in the second part of this thesis.

Biexcitonic Optical Gain in $CsPbBr_3$ Quantum Dots

Although the **origin of optical gain in LHP nanocrystals (NCs) is still discussed in literature**, amplified spontaneous emission (ASE) in relatively large $CsPbBr_3$ NCs has been reported since 2015[160,161] and they have already been integrated into optical resonators.[48–50] Optical gain has been attributed to single excitons,[160,165,166] trions,[167] and biexcitons.[114,161,163,164] I aim to provide clarity on the gain origin by studying the light amplification properties of $CsPbBr_3$ QDs. First, I investigate dense films of spherical $CsPbBr_3$ QDs under excitation with a rectangular laser spot to verify their ability to exhibit ASE. Along this illuminated strip, ASE is observed when the excitation fluence is sufficient to achieve population inversion and the stripe length is long enough to overcome losses.[25,168] I characterize these requirements by determining an ASE threshold fluence of $58\,\mu\mathrm{J/cm^2}$ and a net optical gain coefficient of $93\,\mathrm{cm}^{-1}$ through power-dependent measurements and the variable stripe length method, respectively. Second, I conclusively **attribute the origin of the optical gain to biexcitons** through a comprehensive analysis of power-dependent and time-resolved TA spectroscopy. I performed these measurements on spherical $CsPbBr_3$ QDs with a diameter of ~6 nm. This study builds on the results of the first chapter, in which I identify bleached excitonic and induced biexcitonic transitions as the main processes dominating the TA spectra, along with stimulated emission from the occupied excitonic level, which becomes increasingly relevant with excitation fluence. The assignment to biexcitonic gain is based on three key arguments:

- The **gain threshold** in units of the average number of excitons created per QD is found to be $\langle N \rangle_{\mathrm{th}} = 0.99$. Together with the determined biexciton binding energy of ~68 meV, this value aligns well with the threshold expected for biexcitons with attractive binding energy.

- The **spectral signature** of optical gain in TA spectra overlaps with the TA signal of the energetically lowest biexciton. The redshift of ~56 meV between the two features I attribute to a reasonable Stokes shift, similar to the one observed in steady-state absorption and PL spectra.

- The **gain duration** saturates at ~28 ps, which matches the determined biexciton lifetime of ~29 ps. The gain duration, limited by the presence of biexcitons, highlights their crucial role as prerequisites for optical gain.

My findings on biexcitonic gain can be considered intrinsic to the material class of LHP QDs, as they are not significantly influenced by reabsorption and inhomogeneous broadening.

Understanding the underlying gain mechanism is the basis for addressing the fundamental limitations of QDs in this context, going beyond simple sample optimization strategies. With the fundamental origin of optical gain being attributed to biexcitons, the extensive knowledge from conventional II-VI QDs regarding core/shell engineering,[80,81,126] charging,[113,124] and doping,[212] can now be transferred to LHP QDs. It offers strategies for enhancing their intrinsic light amplification properties by lowering the gain threshold and prolonging the gain lifetime. This establishes a foundation for future work using LHP QDs in lasers. Established resonator geometries, such as whispering gallery modes[160,161,233,234] or vertical cavity surface-emitting lasers,[235–237] can serve as starting points, paving the way for LHP QDs as candidates for efficient and scalable lasing devices.

References

[1] Karl W. Böer and Udo W. Pohl. *Semiconductor Physics.* Cham: Springer International Publishing, 2018. DOI: 10.1007/978-3-319-69150-3 (cited on pages 1, 7).

[2] Yasuhiro Shirasaki, Geoffrey J. Supran, Moungi G. Bawendi, and Vladimir Bulović. "Emergence of colloidal quantum-dot light-emitting technologies." In: *Nature Photonics* 7.1 (2013), pp. 13–23. DOI: 10.1038/nphoton.2012.328 (cited on pages 1, 2, 17).

[3] Abhishek K. Srivastava, Wanlong Zhang, Julian Schneider, Jonathan E. Halpert, and Andrey L. Rogach. "Luminescent Down-Conversion Semiconductor Quantum Dots and Aligned Quantum Rods for Liquid Crystal Displays." In: *Advanced science (Weinheim, Baden-Wurttemberg, Germany)* 6.22 (2019), p. 1901345. DOI: 10.1002/advs.201901345 (cited on pages 1, 2, 17).

[4] Vanessa Wood and Vladimir Bulović. "Colloidal quantum dot light-emitting devices." In: *Nano reviews* 1 (2010). DOI: 10.3402/nano.v1i0.5202 (cited on pages 1, 2, 17).

[5] F. Pelayo García de Arquer, Dmitri V. Talapin, Victor I. Klimov, Yasuhiko Arakawa, Manfred Bayer, and Edward H. Sargent. "Semiconductor quantum dots: Technological progress and future challenges." In: *Science (New York, N.Y.)* 373.6555 (2021). DOI: 10.1126/science.aaz8541 (cited on pages 1, 17).

[6] M. A. Reed, R. T. Bate, K. Bradshaw, W. M. Duncan, W. R. Frensley, J. W. Lee, and H. D. Shih. "Spatial quantization in GaAs-AlGaAs multiple quantum dots." In: *J. Vac. Sci. Technol. B* 4.1 (1986), pp. 358–360 (cited on pages 1, 6).

[7] Cherie R. Kagan, Efrat Lifshitz, Edward H. Sargent, and Dmitri V. Talapin. "Building devices from colloidal quantum dots." In: *Science (New York, N.Y.)* 353.6302 (2016). DOI: 10.1126/science.aac5523 (cited on pages 1, 10, 17).

[8] A. I. Ekimov and A. A. Onushchenko. "Quantum size effect in the optical spectra of semiconductor microcrystals." In: *Sov. Phys. Semicond.* 16.7 (1982), pp. 775–778 (cited on pages 1, 7, 10).

[9] A. I. Ekimov and A. A. Onushchenko. "Quantum Size Effect in Three-Dimensional Microscopic Semiconductor Crystals." In: *JETP Letters* 118.S1 (2023), S15–S17. DOI: 10.1134/S0021364023130040 (cited on page 1).

[10] R. Rossetti, S. Nakahara, and L. E. Brus. "Quantum size effects in the redox potentials, resonance Raman spectra, and electronic spectra of CdS crystallites in aqueous solution." In: *The Journal of chemical physics* 79.2 (1983), pp. 1086–1088. DOI: 10.1063/1.445834 (cited on pages 1, 10).

[11] C. B. Murray, D. J. Norris, and M. G. Bawendi. "Synthesis and characterization of nearly monodisperse CdE (E = sulfur, selenium, tellurium) semiconductor nanocrystallites." In: *Journal of the American Chemical Society* 115.19 (1993), pp. 8706–8715. DOI: 10.1021/ja00072a025 (cited on page 1).

[12] Alexander L. Efros and Louis E. Brus. "Nanocrystal Quantum Dots: From Discovery to Modern Development." In: *ACS nano* 15.4 (2021), pp. 6192–6210. DOI: 10.1021/acsnano.1c01399 (cited on pages 1, 10, 13).

[13] Nobel Committee for Chemistry. *Scientific Background to the Nobel Prize in Chemistry 2023: Quantum Dots - Seeds of Nanoscience.* 2023 (cited on pages 1, 10).

[14] V. L. Colvin, M. C. Schlamp, and A. P. Alivisatos. "Light-emitting diodes made from cadmium selenide nanocrystals and a semiconducting polymer." In: *Nature* 370.6488 (1994), pp. 354–357. DOI: 10.1038/370354a0 (cited on pages 2, 17).

[15] Qinghong Lin, Yangbin Zhu, Yue Wang, Deli Li, Yi Zhao, Yang Liu, Fushan Li, and Wei Huang. "Flexible Quantum Dot Light-Emitting Device for Emerging Multifunctional and Smart Applications." In: *Advanced Materials* 35.32 (2023), e2210385. DOI: 10.1002/adma.202210385 (cited on pages 2, 17, 74).

[16] A.J Nozik. "Quantum dot solar cells." In: *Physica E: Low-dimensional Systems and Nanostructures* 14.1-2 (2002), pp. 115–120. DOI: 10.1016/S1386-9477(02)00374-0 (cited on pages 2, 17).

[17] Octavi E. Semonin, Joseph M. Luther, and Matthew C. Beard. “Quantum dots for next-generation photovoltaics.” In: *Materials Today* 15.11 (2012), pp. 508–515. DOI: 10.1016/S1369-7021(12)70220-1 (cited on pages 2, 17).

[18] Matthew C. Beard, Joseph M. Luther, Octavi E. Semonin, and Arthur J. Nozik. “Third generation photovoltaics based on multiple exciton generation in quantum confined semiconductors.” In: *Accounts of chemical research* 46.6 (2013), pp. 1252–1260. DOI: 10.1021/ar3001958 (cited on pages 2, 17).

[19] Emily A. Weiss. “Designing the Surfaces of Semiconductor Quantum Dots for Colloidal Photocatalysis.” In: *ACS energy letters* 2.5 (2017), pp. 1005–1013. DOI: 10.1021/acsenergylett.7b00061 (cited on pages 2, 17).

[20] Peng Sun, Zipeng Xing, Zhenzi Li, and Wei Zhou. “Recent advances in quantum dots photocatalysts.” In: *Chemical Engineering Journal* 458 (2023), p. 141399. DOI: 10.1016/j.cej.2023.141399 (cited on pages 2, 17).

[21] M. Bruchez, M. Moronne, P. Gin, S. Weiss, and A. P. Alivisatos. “Semiconductor nanocrystals as fluorescent biological labels.” In: *Science (New York, N.Y.)* 281.5385 (1998), pp. 2013–2016. DOI: 10.1126/science.281.5385.2013 (cited on pages 2, 17).

[22] W. C. Chan and S. Nie. “Quantum dot bioconjugates for ultrasensitive nonisotopic detection.” In: *Science (New York, N.Y.)* 281.5385 (1998), pp. 2016–2018. DOI: 10.1126/science.281.5385.2016 (cited on pages 2, 17).

[23] Sonal Mazumder, Rajib Dey, M. K. Mitra, S. Mukherjee, and G. C. Das. “Review: Biofunctionalized Quantum Dots in Biology and Medicine.” In: *Journal of Nanomaterials* 2009.1 (2009). DOI: 10.1155/2009/815734 (cited on pages 2, 17).

[24] Young-Shin Park, Jeongkyun Roh, Benjamin T. Diroll, Richard D. Schaller, and Victor I. Klimov. “Colloidal quantum dot lasers.” In: *Nature Reviews Materials* 6.5 (2021), pp. 382–401. DOI: 10.1038/s41578-020-00274-9 (cited on pages 2, 14–17, 59).

[25] Namyoung Ahn, Clément Livache, Valerio Pinchetti, and Victor I. Klimov. “Colloidal Semiconductor Nanocrystal Lasers and Laser Diodes.” In: *Chemical reviews* 123.13 (2023), pp. 8251–8296. DOI: 10.1021/acs.chemrev.2c00865 (cited on pages 2, 10, 13, 15–17, 21, 22, 59, 61, 63, 65, 75).

[26] Akihiro Kojima, Kenjiro Teshima, Yasuo Shirai, and Tsutomu Miyasaka. “Organometal halide perovskites as visible-light sensitizers for photovoltaic cells.” In: *Journal of the American Chemical Society* 131.17 (2009), pp. 6050–6051. DOI: 10.1021/ja809598r (cited on pages 2, 17, 20).

[27] Wanyi Nie, Hsinhan Tsai, Reza Asadpour, Jean-Christophe Blancon, Amanda J. Neukirch, Gautam Gupta, Jared J. Crochet, Manish Chhowalla, Sergei Tretiak, Muhammad A. Alam, Hsing-Lin Wang, and Aditya D. Mohite. “Solar cells. High-efficiency solution-processed perovskite solar cells with millimeter-scale grains.” In: *Science (New York, N.Y.)* 347.6221 (2015), pp. 522–525. DOI: 10.1126/science.aaa0472 (cited on pages 2, 20).

[28] M. I. Asghar, J. Zhang, H. Wang, and P. D. Lund. “Device stability of perovskite solar cells – A review.” In: *Renewable and Sustainable Energy Reviews* 77 (2017), pp. 131–146. DOI: 10.1016/j.rser.2017.04.003 (cited on pages 2, 20).

[29] Michiel L. Petrus, Johannes Schlipf, Cheng Li, Tanaji P. Gujar, Nadja Giesbrecht, Peter Müller-Buschbaum, Mukundan Thelakkat, Thomas Bein, Sven Hüttner, and Pablo Docampo. “Capturing the Sun: A Review of the Challenges and Perspectives of Perovskite Solar Cells.” In: *Advanced Energy Materials* 7.16 (2017), p. 1700264. DOI: 10.1002/aenm.201700264 (cited on pages 2, 20).

[30] Mohammed Istafaul Haque Ansari, Ahsanulhaq Qurashi, and Mohammad Khaja Nazeeruddin. “Frontiers, opportunities, and challenges in perovskite solar cells: A critical review.” In: *Journal of Photochemistry and Photobiology C: Photochemistry Reviews* 35 (2018), pp. 1–24. DOI: 10.1016/j.jphotochemrev.2017.11.002 (cited on pages 2, 20).

[31] Loredana Protesescu, Sergii Yakunin, Maryna I. Bodnarchuk, Franziska Krieg, Riccarda Caputo, Christopher H. Hendon, Ruo Xi Yang, Aron Walsh, and Maksym V. Kovalenko. “Nanocrystals of Cesium Lead Halide Perovskites ($CsPbX_3$, X = Cl, Br, and I): Novel Optoelectronic Materials Showing Bright Emission with Wide Color Gamut.” In: *Nano letters* 15.6 (2015), pp. 3692–3696. DOI: 10.1021/nl5048779 (cited on pages 2, 20, 26, 59, 69).

[32] Jasmina A. Sichert, Yu Tong, Niklas Mutz, Mathias Vollmer, Stefan Fischer, Karolina Z. Milowska, Ramon García Cortadella, Bert Nickel, Carlos Cardenas-Daw, Jacek K. Stolarczyk, Alexander S. Urban, and Jochen Feldmann. “Quantum Size Effect in Organometal Halide Perovskite Nanoplatelets.” In: *Nano letters* 15.10 (2015), pp. 6521–6527. DOI: 10.1021/acs.nanolett.5b02985 (cited on pages 2, 20).

[33] Quinten A. Akkerman, Valerio D’Innocenzo, Sara Accornero, Alice Scarpellini, Annamaria Petrozza, Mirko Prato, and Liberato Manna. “Tuning the Optical Properties of Cesium Lead Halide Perovskite Nanocrystals by Anion Exchange Reactions.” In: *Journal of the American Chemical Society* 137.32 (2015), pp. 10276–10281. DOI: 10.1021/jacs.5b05602 (cited on pages 2, 21, 59).

[34] Maksym V. Kovalenko, Loredana Protesescu, and Maryna I. Bodnarchuk. “Properties and potential optoelectronic applications of lead halide perovskite nanocrystals.” In: *Science (New York, N.Y.)* 358.6364 (2017), pp. 745–750. DOI: 10.1126/science.aam7093 (cited on pages 2, 18, 20).

[35] Handong Jin, Elke Debroye, Masoumeh Keshavarz, Ivan G. Scheblykin, Maarten B. J. Roeffaers, Johan Hofkens, and Julian A. Steele. “It’s a trap! On the nature of localised states and charge trapping in lead halide perovskites.” In: *Materials Horizons* 7.2 (2020), pp. 397–410. DOI: 10.1039/c9mh00500e (cited on pages 2, 18).

[36] Quinten A. Akkerman, Gabriele Rainò, Maksym V. Kovalenko, and Liberato Manna. “Genesis, challenges and opportunities for colloidal lead halide perovskite nanocrystals.” In: *Nature materials* 17.5 (2018), pp. 394–405. DOI: 10.1038/s41563-018-0018-4 (cited on pages 2, 18, 21).

[37] Baiquan Liu, Lin Wang, Haoshuang Gu, Handong Sun, and Hilmi Volkan Demir. “Highly Efficient Green Light–Emitting Diodes from All–Inorganic Perovskite Nanocrystals Enabled by a New Electron Transport Layer.” In: *Advanced Optical Materials* 6.11 (2018). DOI: 10.1002/adom.201800220 (cited on pages 2, 21, 74).

[38] Yuanzhi Jiang, Changjiu Sun, Jian Xu, Saisai Li, Minghuan Cui, Xinliang Fu, Yuan Liu, Yaqi Liu, Haoyue Wan, Keyu Wei, Tong Zhou, Wei Zhang, Yingguo Yang, Jien Yang, Chaochao Qin, Shuyan Gao, Jun Pan, Yufang Liu, Sjoerd Hoogland, Edward H. Sargent, Jun Chen, and Mingjian Yuan. “Synthesis-on-substrate of quantum dot solids.” In: *Nature* 612.7941 (2022), pp. 679–684. DOI: 10.1038/s41586-022-05486-3 (cited on pages 2, 21, 74).

[39] Yun-Fei Li, Shu-Yu Chou, Peng Huang, Changtao Xiao, Xiaofeng Liu, Yu Xie, Fangchao Zhao, Yilong Huang, Jing Feng, Haizheng Zhong, Hong-Bo Sun, and Qibing Pei. “Stretchable Organometal-Halide-Perovskite Quantum-Dot Light-Emitting Diodes.” In: *Advanced Materials* 31.22 (2019), e1807516. DOI: 10.1002/adma.201807516 (cited on pages 2, 21).

[40] Huanyu Zhou, Jinwoo Park, Yeongjun Lee, Jae-Man Park, Jin-Hoon Kim, Joo Sung Kim, Hyeon-Dong Lee, Seung Hyeon Jo, Xue Cai, Lizhu Li, Xing Sheng, Hyung Joong Yun, Jin-Woo Park, Jeong-Yun Sun, and Tae-Woo Lee. “Water Passivation of Perovskite Nanocrystals Enables Air-Stable Intrinsically Stretchable Color-Conversion Layers for Stretchable Displays.” In: *Advanced Materials* 32.37 (2020), e2001989. DOI: 10.1002/adma.202001989 (cited on pages 2, 21).

[41] Jong Ik Kwon, Gyuri Park, Gwang Heon Lee, Jae Hong Jang, Nak Jun Sung, Seo Young Kim, Jisu Yoo, Kyunghoon Lee, Hyeonjong Ma, Minji Karl, Tae Joo Shin, Myoung Hoon Song, Jiwoong Yang, and Moon Kee Choi. “Ultrahigh-resolution full-color perovskite nanocrystal patterning for ultrathin skin-attachable displays.” In: *Science advances* 8.43 (2022), eadd0697. DOI: 10.1126/sciadv.add0697 (cited on pages 2, 21).

[42] Tian Tian, Meifang Yang, Yuxuan Fang, Shuo Zhang, Yuxin Chen, Lianzhou Wang, and Wu-Qiang Wu. “Large-area waterproof and durable perovskite luminescent textiles.” In: *Nature Communications* 14.1 (2023), p. 234. DOI: 10.1038/s41467-023-35830-8 (cited on pages 2, 21).

[43] Fengjun Chun, Binbin Zhang, Yuyu Gao, Xiaohe Wei, Qiang Zhang, Weilin Zheng, Jingkun Zhou, Yang Guo, Xin Zhang, Zhifeng Xing, Xinge Yu, and Feng Wang. “Multicolour stretchable perovskite electroluminescent devices for user-interactive displays.” In: *Nature Photonics* 18 (2024), pp. 856–863. DOI: 10.1038/s41566-024-01455-6 (cited on pages 2, 21).

[44] Young-Shin Park, Shaojun Guo, Nikolay S. Makarov, and Victor I. Klimov. “Room Temperature Single-Photon Emission from Individual Perovskite Quantum Dots.” In: *ACS nano* 9.10 (2015), pp. 10386–10393. DOI: 10.1021/acsnano.5b04584 (cited on pages 2, 21, 74).

[45] Hendrik Utzat, Weiwei Sun, Alexander E. K. Kaplan, Franziska Krieg, Matthias Ginterseder, Boris Spokoyny, Nathan D. Klein, Katherine E. Shulenberger, Collin F. Perkinson, Maksym V. Kovalenko, and Moungi G. Bawendi. “Coherent single-photon emission from colloidal lead halide perovskite quantum dots.” In: *Science (New York, N.Y.)* 363.6431 (2019), pp. 1068–1072. DOI: 10.1126/science.aau7392 (cited on pages 2, 21, 48, 74).

[46] Stefania Castelletto, Filippo de Angelis, and Alberto Boretti. “Prospects and challenges of quantum emitters in perovskites nanocrystals.” In: *Applied Materials Today* 26 (2022), p. 101401. DOI: 10.1016/j.apmt.2022.101401 (cited on pages 2, 21, 48, 74).

[47] Chenglian Zhu, Malwina Marczak, Leon Feld, Simon C. Boehme, Caterina Bernasconi, Anastasiia Moskalenko, Ihor Cherniukh, Dmitry Dirin, Maryna I. Bodnarchuk, Maksym V. Kovalenko, and Gabriele Rainò. “Room-Temperature, Highly Pure Single-Photon Sources from All-Inorganic Lead Halide Perovskite Quantum Dots.” In: *Nano letters* 22.9 (2022), pp. 3751–3760. DOI: 10.1021/acs.nanolett.2c00756 (cited on pages 2, 21, 74).

[48] Jie Chen, Wenna Du, Jianwei Shi, Meili Li, Yue Wang, Qing Zhang, and Xinfeng Liu. “Perovskite quantum dot lasers.” In: *InfoMat* 2.1 (2020), pp. 170–183. DOI: 10.1002/inf2.12051 (cited on pages 2, 21, 22, 48, 59, 74, 75).

[49] Qing Zhang, Qiuyu Shang, Rui Su, T. Thu Ha Do, and Qihua Xiong. “Halide Perovskite Semiconductor Lasers: Materials, Cavity Design, and Low Threshold.” In: *Nano letters* 21.5 (2021), pp. 1903–1914. DOI: 10.1021/acs.nanolett.0c03593 (cited on pages 2, 21, 22, 59, 74, 75).

[50] Lei Lei, Qi Dong, Kenan Gundogdu, and Franky So. “Metal Halide Perovskites for Laser Applications.” In: *Advanced Functional Materials* 31.16 (2021). DOI: 10.1002/adfm.202010144 (cited on pages 2, 21, 22, 59, 74, 75).

[51] Amrita Dey, Junzhi Ye, Apurba De, Elke Debroye, Seung Kyun Ha, Eva Bladt, Anuraj S. Kshirsagar, Ziyu Wang, Jun Yin, Yue Wang, Li Na Quan, Fei Yan, Mengyu Gao, Xiaoming Li, Javad Shamsi, Tushar Debnath, Muhan Cao, Manuel A. Scheel, Sudhir Kumar, Julian A. Steele, Marina Gerhard, Lata Chouhan, Ke Xu, Xian-Gang Wu, Yanxiu Li, Yangning Zhang, Anirban Dutta, Chuang Han, Ilka Vincon, Andrey L. Rogach, Angshuman Nag, Anunay Samanta, Brian A. Korgel, Chih-Jen Shih, Daniel R. Gamelin, Dong Hee Son, Haibo Zeng, Haizheng Zhong, Handong Sun, Hilmi Volkan Demir, Ivan G. Scheblykin, Iván Mora-Seró, Jacek K. Stolarczyk, Jin Z. Zhang, Jochen Feldmann, Johan Hofkens, Joseph M. Luther, Julia Pérez-Prieto, Liang Li, Liberato Manna, Maryna I. Bodnarchuk, Maksym V. Kovalenko, Maarten B. J. Roeffaers, Narayan Pradhan, Omar F. Mohammed, Osman M. Bakr, Peidong Yang, Peter Müller-Buschbaum, Prashant V. Kamat, Qiaoliang Bao, Qiao Zhang, Roman Krahne, Raquel E. Galian, Samuel D. Stranks, Sara Bals, Vasudevanpillai Biju, William A. Tisdale, Yong Yan, Robert L. Z. Hoye, and Lakshminarayana Polavarapu. “State of the Art and Prospects for Halide Perovskite Nanocrystals.” In: *ACS nano* 15.7 (2021), pp. 10775–10981. DOI: 10.1021/acsnano.0c08903 (cited on pages 2, 19–21, 43, 59, 73).

[52] A. P. Alivisatos, A. L. Harris, N. J. Levinos, M. L. Steigerwald, and L. E. Brus. “Electronic states of semiconductor clusters: Homogeneous and inhomogeneous broadening of the optical spectrum.” In: *The Journal of chemical physics* 89.7 (1988), pp. 4001–4011. DOI: 10.1063/1.454833 (cited on pages 2, 11).

[53] Sergey V. Gaponenko. *Optical properties of semiconductor nanocrystals.* Vol. 23. Cambridge studies in modern optics. Cambridge: Cambridge University Press, 1998. DOI: 10.1017/CBO9780511524141 (cited on pages 2, 6–11, 20, 43, 73).

[54] Quinten A. Akkerman, Tan P. T. Nguyen, Simon C. Boehme, Federico Montanarella, Dmitry N. Dirin, Philipp Wechsler, Finn Beiglböck, Gabriele Rainò, Rolf Erni, Claudine Katan, Jacky Even, and Maksym V. Kovalenko. “Controlling the nucleation and growth kinetics of lead halide perovskite quantum dots.” In: *Science (New York, N.Y.)* 377.6613 (2022), pp. 1406–1412. DOI: 10.1126/science.abq3616 (cited on pages 2, 26–28, 43–45, 47, 73, XIX).

[55] Charles Kittel. *Introduction to solid state physics.* 8., internat. ed. Hoboken, NJ: Wiley, 2005 (cited on page 6).

[56] U. Woggon and S. V. Gaponenko. “Excitons in Quantum Dots.” In: *physica status solidi (b)* 189.2 (1995), pp. 285–343. DOI: 10.1002/pssb.2221890202 (cited on pages 6, 9, 12, 43).

[57] David J. Griffiths. *Introduction to quantum mechanics.* Englewood Cliffs, NJ: Prentice Hall, 1995 (cited on pages 6, 12).

[58] Mark Fox. *Optical properties of solids.* Second edition. Vol. 3. Oxford master series in physics Condensed matter physics. Oxford and New York: Oxford University Press, 2010 (cited on pages 7, 28).

[59] Claus F. Klingshirn. *Semiconductor Optics.* Berlin, Heidelberg: Springer Berlin Heidelberg, 2012. DOI: 10.1007/978-3-642-28362-8 (cited on pages 7, 12).

[60] Al. L. Efros and A. L. Efros. "Interband absorption of light in a semiconductor sphere." In: *Sov. Phys. Semicond.* 16.7 (1982), pp. 772–775 (cited on page 7).

[61] A. I. Ekimov. "Optical Properties of Semiconductor Quantum Dots in Glass Matrix." In: *Physica Scripta* T39 (1991), pp. 217–222. DOI: 10.1088/0031-8949/1991/T39/033 (cited on pages 7, 10, 12).

[62] Ivan Pelant and Jan Valenta. *Luminescence spectroscopy of semiconductors.* Oxford: Oxford Univ. Press, 2012 (cited on pages 7, 34, 42, 62).

[63] R. H. Dicke. "Coherence in Spontaneous Radiation Processes." In: *Physical Review* 93.1 (1954), pp. 99–110. DOI: 10.1103/PhysRev.93.99 (cited on page 8).

[64] J. Feldmann, G. Peter, E. O. Göbel, P. Dawson, K. Moore, C. Foxon, and R. J. Elliott. "Linewidth dependence of radiative exciton lifetimes in quantum wells." In: *Physical Review Letters* 59.20 (1987), pp. 2337–2340. DOI: 10.1103/PhysRevLett.59.2337 (cited on page 8).

[65] Petru Tighineanu, Raphaël S. Daveau, Tau B. Lehmann, Harvey E. Beere, David A. Ritchie, Peter Lodahl, and Søren Stobbe. "Single-Photon Superradiance from a Quantum Dot." In: *Physical Review Letters* 116.16 (2016), p. 163604. DOI: 10.1103/PhysRevLett.116.163604 (cited on page 8).

[66] Chenglian Zhu, Simon C. Boehme, Leon G. Feld, Anastasiia Moskalenko, Dmitry N. Dirin, Rainer F. Mahrt, Thilo Stöferle, Maryna I. Bodnarchuk, Alexander L. Efros, Peter C. Sercel, Maksym V. Kovalenko, and Gabriele Rainò. "Single-photon superradiance in individual caesium lead halide quantum dots." In: *Nature* 626.7999 (2024), pp. 535–541. DOI: 10.1038/s41586-023-07001-8 (cited on pages 8, 9, 74).

[67] Al. L. Efros and M. Rosen. "The Electronic Structure of Semiconductor Nanocrystals." In: *Annual Review of Materials Science* 30.1 (2000), pp. 475–521. DOI: 10.1146/annurev.matsci.30.1.475 (cited on pages 8, 12, 43, 73).

[68] Praket P. Jha and Philippe Guyot-Sionnest. "Trion decay in colloidal quantum dots." In: *ACS nano* 3.4 (2009), pp. 1011–1015. DOI: 10.1021/nn9001177 (cited on pages 9, 13).

[69] Y. Z. Hu, S. W. Koch, M. Lindberg, N. Peyghambarian, E. L. Pollock, and F. F. Abraham. "Biexcitons in semiconductor quantum dots." In: *Physical Review Letters* 64.15 (1990), pp. 1805–1807. DOI: 10.1103/PhysRevLett.64.1805 (cited on page 10).

[70] U. Woggon, H. Giessen, F. Gindele, O. Wind, B. Fluegel, and N. Peyghambarian. "Ultrafast energy relaxation in quantum dots." In: *Physical review. B, Condensed matter* 54.24 (1996), pp. 17681–17690. DOI: 10.1103/PhysRevB.54.17681 (cited on pages 10, 12, 43).

[71] Pierre M. Petroff, Axel Lorke, and Atac Imamoglu. "Epitaxially Self-Assembled Quantum Dots." In: *Physics Today* 54.5 (2001), pp. 46–52. DOI: 10.1063/1.1381102 (cited on page 10).

[72] Xiaoyan Zhou, Liang Zhai, and Jin Liu. "Epitaxial quantum dots: a semiconductor launchpad for photonic quantum technologies." In: *Photonics Insights* 1.2 (2022), R07. DOI: 10.3788/PI.2022.R07 (cited on page 10).

[73] U. Woggon, S. Gaponenko, W. Langbein, A. Uhrig, and C. Klingshirn. "Homogeneous linewidth of confined electron-hole-pair states in II-VI quantum dots." In: *Physical review. B, Condensed matter* 47.7 (1993), pp. 3684–3689. DOI: 10.1103/PhysRevB.47.3684 (cited on page 10).

[74] Mengling Xia, Jiajun Luo, Chao Chen, Huan Liu, and Jiang Tang. "Semiconductor Quantum Dots–Embedded Inorganic Glasses: Fabrication, Luminescent Properties, and Potential Applications." In: *Advanced Optical Materials* 7.21 (2019). DOI: 10.1002/adom.201900851 (cited on page 10).

[75] Amelie Heuer-Jungemann, Neus Feliu, Ioanna Bakaimi, Majd Hamaly, Alaaldin Alkilany, Indranath Chakraborty, Atif Masood, Maria F. Casula, Athanasia Kostopoulou, Eunkeu Oh, Kimihiro Susumu, Michael H. Stewart, Igor L. Medintz, Emmanuel Stratakis, Wolfgang J. Parak, and Antonios G. Kanaras. “The Role of Ligands in the Chemical Synthesis and Applications of Inorganic Nanoparticles.” In: *Chemical reviews* 119.8 (2019), pp. 4819–4880. DOI: 10.1021/acs.chemrev.8b00733 (cited on page 10).

[76] A. Eychmüller, A. Hässelbarth, L. Katsikas, and H. Weller. “Fluorescence mechanism of highly monodisperse Q-sized CdS colloids.” In: *Journal of Luminescence* 48-49 (1991), pp. 745–749. DOI: 10.1016/0022-2313(91)90232-K (cited on page 10).

[77] A. R. Kortan, R. Hull, R. L. Opila, M. G. Bawendi, M. L. Steigerwald, P. J. Carroll, and Louis E. Brus. “Nucleation and Growth of CdSe on ZnS Quantum Crystallite Seeds, and Vice Versa, in Inverse Micelle Media.” In: *Journal of the American Chemical Society* 112.4 (1990), pp. 1327–1332. DOI: 10.1021/ja00160a005 (cited on page 10).

[78] Margaret A. Hines and Philippe Guyot-Sionnest. “Synthesis and Characterization of Strongly Luminescing ZnS-Capped CdSe Nanocrystals.” In: *The journal of physical chemistry* 100.2 (1996), pp. 468–471. DOI: 10.1021/jp9530562 (cited on page 10).

[79] Young-Shin Park, Wan Ki Bae, Thomas Baker, Jaehoon Lim, and Victor I. Klimov. “Effect of Auger Recombination on Lasing in Heterostructured Quantum Dots with Engineered Core/Shell Interfaces.” In: *Nano letters* 15.11 (2015), pp. 7319–7328. DOI: 10.1021/acs.nanolett.5b02595 (cited on pages 11, 13, 15).

[80] Jaehoon Lim, Young-Shin Park, and Victor I. Klimov. “Optical gain in colloidal quantum dots achieved with direct-current electrical pumping.” In: *Nature materials* 17.1 (2018), pp. 42–49. DOI: 10.1038/nmat5011 (cited on pages 11, 59, 71, 76).

[81] Florencio García-Santamaría, Yongfen Chen, Javier Vela, Richard D. Schaller, Jennifer A. Hollingsworth, and Victor I. Klimov. “Suppressed auger recombination in giant nanocrystals boosts optical gain performance.” In: *Nano letters* 9.10 (2009), pp. 3482–3488. DOI: 10.1021/nl901681d (cited on pages 11, 16, 59, 71, 76).

[82] Nikolai Gaponik, Stephen G. Hickey, Dirk Dorfs, Andrey L. Rogach, and Alexander Eychmüller. “Progress in the light emission of colloidal semiconductor nanocrystals.” In: *Small (Weinheim an der Bergstrasse, Germany)* 6.13 (2010), pp. 1364–1378. DOI: 10.1002/smll.200902006 (cited on page 11).

[83] Alexander L. Efros and David J. Nesbitt. “Origin and control of blinking in quantum dots.” In: *Nature nanotechnology* 11.8 (2016), pp. 661–671. DOI: 10.1038/nnano.2016.140 (cited on page 11).

[84] Safa O. Kasap. *Optoelectronics and photonics: Principles and practices.* 2. ed, international ed. Always learning. Boston and Munich u.a.: Pearson, 2013 (cited on pages 11, 23).

[85] S. Rudin, T. L. Reinecke, and B. Segall. “Temperature-dependent exciton linewidths in semiconductors.” In: *Physical review. B, Condensed matter* 42.17 (1990), pp. 11218–11231. DOI: 10.1103/PhysRevB.42.11218 (cited on page 11).

[86] Nasser Peyghambarian, Stephan W. Koch, and Andre Mysyrowicz. *Introduction to semiconductor optics.* Prentice-Hall series in solid state physical electronics. Englewood Cliffs, NJ: Prentice-Hall, 1993 (cited on pages 12, 48).

[87] Sviatoslav Anatolʹevich Moskalenko. *Bose-Einstein condensation of excitons and biexcitons: And coherent nonlinear optics with excitons.* Cambridge: Cambridge University Press, 2000. DOI: 10.1017/CBO9780511721687 (cited on page 12).

[88] Mark Fox. *Quantum optics: An introduction.* Repr. Vol. 15. Oxford master series in physics Atomic, optical, and laser physics. Oxford: Oxford Univ. Press, 2011 (cited on pages 12, 14).

[89] Arash Rahimi-Iman. *Polariton Physics.* Vol. 229. Cham: Springer International Publishing, 2020. DOI: 10.1007/978-3-030-39333-5 (cited on page 12).

[90] Victor I. Klimov. “Optical Nonlinearities and Ultrafast Carrier Dynamics in Semiconductor Nanocrystals.” In: *The Journal of Physical Chemistry B* 104.26 (2000), pp. 6112–6123. DOI: 10.1021/jp9944132 (cited on pages 12, 14, 37, 49).

[91] Victor I. Klimov. “Spectral and dynamical properties of multiexcitons in semiconductor nanocrystals.” In: *Annual review of physical chemistry* 58 (2007), pp. 635–673. DOI: 10.1146/annurev.physchem.58.032806.104537 (cited on pages 12, 13, 35, 43).

[92] Andrey L. Rogach, Thomas A. Klar, John M. Lupton, Andries Meijerink, and Jochen Feldmann. “Energy transfer with semiconductor nanocrystals.” In: *Journal of Materials Chemistry* 19.9 (2009), pp. 1208–1221. DOI: 10.1039/B812884G (cited on pages 12, 43).

[93] Patanjali Kambhampati. “Unraveling the structure and dynamics of excitons in semiconductor quantum dots.” In: *Accounts of chemical research* 44.1 (2011), pp. 1–13. DOI: 10.1021/ar1000428 (cited on pages 12, 43).

[94] Efros, Rosen, Kuno, Nirmal, Norris, and Bawendi. “Band-edge exciton in quantum dots of semiconductors with a degenerate valence band: Dark and bright exciton states.” In: *Physical review. B, Condensed matter* 54.7 (1996), pp. 4843–4856. DOI: 10.1103/PhysRevB.54.4843 (cited on pages 12, 43).

[95] M. Ediger, G. Bester, B. D. Gerardot, A. Badolato, P. M. Petroff, K. Karrai, A. Zunger, and R. J. Warburton. “Fine structure of negatively and positively charged excitons in semiconductor quantum dots: electron-hole asymmetry.” In: *Physical Review Letters* 98.3 (2007), p. 036808. DOI: 10.1103/PhysRevLett.98.036808 (cited on page 12).

[96] B. Patton, W. Langbein, and U. Woggon. “Trion, biexciton, and exciton dynamics in single self-assembled CdSe quantum dots.” In: *Physical review. B, Condensed matter* 68.12 (2003). DOI: 10.1103/PhysRevB.68.125316 (cited on pages 12, 43).

[97] R. M. Stevenson, R. J. Young, P. See, D. G. Gevaux, K. Cooper, P. Atkinson, I. Farrer, D. A. Ritchie, and A. J. Shields. “Magnetic-field-induced reduction of the exciton polarization splitting in InAs quantum dots.” In: *Physical Review B* 73.3 (2006). DOI: 10.1103/PhysRevB.73.033306 (cited on page 12).

[98] R. D. Schaller and V. I. Klimov. “High efficiency carrier multiplication in PbSe nanocrystals: implications for solar energy conversion.” In: *Physical Review Letters* 92.18 (2004), p. 186601. DOI: 10.1103/PhysRevLett.92.186601 (cited on pages 12, 43).

[99] Richard D. Schaller, Vladimir M. Agranovich, and Victor I. Klimov. “High-efficiency carrier multiplication through direct photogeneration of multi-excitons via virtual single-exciton states.” In: *Nature Physics* 1.3 (2005), pp. 189–194. DOI: 10.1038/nphys151 (cited on page 12).

[100] Matthew C. Beard. “Multiple Exciton Generation in Semiconductor Quantum Dots.” In: *The journal of physical chemistry letters* 2.11 (2011), pp. 1282–1288 (cited on page 12).

[101] V. I. Klimov, D. W. McBranch, C. A. Leatherdale, and M. G. Bawendi. “Electron and hole relaxation pathways in semiconductor quantum dots.” In: *Physical review. B, Condensed matter* 60.19 (1999), pp. 13740–13749. DOI: 10.1103/PhysRevB.60.13740 (cited on page 12).

[102] A. J. Nozik. “Spectroscopy and hot electron relaxation dynamics in semiconductor quantum wells and quantum dots.” In: *Annual review of physical chemistry* 52 (2001), pp. 193–231. DOI: 10.1146/annurev.physchem.52.1.193 (cited on page 12).

[103] A. R. Beattie and P. T. Landsberg. “Auger effect in semiconductors.” In: *Proceedings of the Royal Society of London. Series A. Mathematical and Physical Sciences* 249.1256 (1959), pp. 16–29. DOI: 10.1098/rspa.1959.0003 (cited on page 12).

[104] Jagdeep Shah. *Ultrafast Spectroscopy of Semiconductors and Semiconductor Nanostructures.* Vol. 115. Berlin, Heidelberg: Springer Berlin Heidelberg, 1999. DOI: 10.1007/978-3-662-03770-6 (cited on pages 12, 35).

[105] Géraud Delport, Gabriel Chehade, Ferdinand Lédée, Hiba Diab, Cosme Milesi-Brault, Gaëlle Trippé-Allard, Jacky Even, Jean-Sébastien Lauret, Emmanuelle Deleporte, and Damien Garrot. “Exciton-Exciton Annihilation in Two-Dimensional Halide Perovskites at Room Temperature.” In: *The journal of physical chemistry letters* 10.17 (2019), pp. 5153–5159. DOI: 10.1021/acs.jpclett.9b01595 (cited on page 12).

[106] M. Achermann, J. A. Hollingsworth, and V. I. Klimov. “Multiexcitons confined within a subexcitonic volume: Spectroscopic and dynamical signatures of neutral and charged biexcitons in ultrasmall semiconductor nanocrystals.” In: *Physical review. B, Condensed matter* 68.24 (2003). DOI: 10.1103/PhysRevB.68.245302 (cited on page 13).

[107] István Robel, Ryan Gresback, Uwe Kortshagen, Richard D. Schaller, and Victor I. Klimov. "Universal size-dependent trend in auger recombination in direct-gap and indirect-gap semiconductor nanocrystals." In: *Physical Review Letters* 102.17 (2009), p. 177404. DOI: 10.1103/PhysRevLett.102.177404 (cited on page 13).

[108] Young-Shin Park, Wan Ki Bae, Jeffrey M. Pietryga, and Victor I. Klimov. "Auger recombination of biexcitons and negative and positive trions in individual quantum dots." In: *ACS nano* 8.7 (2014), pp. 7288–7296. DOI: 10.1021/nn5023473 (cited on page 13).

[109] Victor I. Klimov. "Multicarrier Interactions in Semiconductor Nanocrystals in Relation to the Phenomena of Auger Recombination and Carrier Multiplication." In: *Annual Review of Condensed Matter Physics* 5.1 (2014), pp. 285–316. DOI: 10.1146/annurev-conmatphys-031113-133900 (cited on pages 13, 16).

[110] Peter W. Milonni and J. H. Eberly. *Lasers physics.* Hoboken N.J.: John Wiley & Sons, 2010 (cited on pages 13, 23).

[111] William Thomas Silfvast. *Laser fundamentals.* 2nd ed. Cambridge and New York: Cambridge University Press, 2004 (cited on page 13).

[112] V. I. Klimov, A. A. Mikhailovsky, S. Xu, A. Malko, J. A. Hollingsworth, C. A. Leatherdale, H. Eisler, and M. G. Bawendi. "Optical gain and stimulated emission in nanocrystal quantum dots." In: *Science (New York, N.Y.)* 290.5490 (2000), pp. 314–317. DOI: 10.1126/science.290.5490.314 (cited on pages 14, 16, 22, 23, 39, 59, 64, 65).

[113] Kaifeng Wu, Young-Shin Park, Jaehoon Lim, and Victor I. Klimov. "Towards zero-threshold optical gain using charged semiconductor quantum dots." In: *Nature nanotechnology* 12.12 (2017), pp. 1140–1147. DOI: 10.1038/NNANO.2017.189 (cited on pages 15, 16, 22, 39, 59, 65, 71, 76).

[114] Gabriel Nagamine, Jaqueline O. Rocha, Luiz G. Bonato, Ana F. Nogueira, Zhanet Zaharieva, Andrew A. R. Watt, Carlos H. de Brito Cruz, and Lazaro A. Padilha. "Two-Photon Absorption and Two-Photon-Induced Gain in Perovskite Quantum Dots." In: *The journal of physical chemistry letters* 9.12 (2018), pp. 3478–3484. DOI: 10.1021/acs.jpclett.8b01127 (cited on pages 15, 22, 59, 61, 64–66, 69, 75).

[115] A. P. Alivisatos. "Semiconductor Clusters, Nanocrystals, and Quantum Dots." In: *Science (New York, N.Y.)* 271.5251 (1996), pp. 933–937. DOI: 10.1126/science.271.5251.933 (cited on page 15).

[116] Y. Arakawa and H. Sakaki. "Multidimensional quantum well laser and temperature dependence of its threshold current." In: *Applied Physics Letters* 40.11 (1982), pp. 939–941. DOI: 10.1063/1.92959 (cited on page 15).

[117] Klimov, Mikhailovsky, McBranch, Leatherdale, and Bawendi. "Quantization of multiparticle auger rates in semiconductor quantum dots." In: *Science (New York, N.Y.)* 287.5455 (2000), pp. 1011–1013. DOI: 10.1126/science.287.5455.1011 (cited on pages 16, 37, 43, 59, 69).

[118] Namyoung Ahn, Clément Livache, Valerio Pinchetti, Heeyoung Jung, Ho Jin, Donghyo Hahm, Young-Shin Park, and Victor I. Klimov. "Electrically driven amplified spontaneous emission from colloidal quantum dots." In: *Nature* 617.7959 (2023), pp. 79–85. DOI: 10.1038/s41586-023-05855-6 (cited on pages 16, 59).

[119] Y-S Park, A. V. Malko, J. Vela, Y. Chen, Y. Ghosh, F. García-Santamaría, J. A. Hollingsworth, V. I. Klimov, and H. Htoon. "Near-unity quantum yields of biexciton emission from CdSe/CdS nanocrystals measured using single-particle spectroscopy." In: *Physical Review Letters* 106.18 (2011), p. 187401. DOI: 10.1103/PhysRevLett.106.187401 (cited on page 16).

[120] Florencio García-Santamaría, Sergio Brovelli, Ranjani Viswanatha, Jennifer A. Hollingsworth, Han Htoon, Scott A. Crooker, and Victor I. Klimov. "Breakdown of volume scaling in Auger recombination in CdSe/CdS heteronanocrystals: the role of the core-shell interface." In: *Nano letters* 11.2 (2011), pp. 687–693. DOI: 10.1021/nl103801e (cited on page 16).

[121] George E. Cragg and Alexander L. Efros. "Suppression of auger processes in confined structures." In: *Nano letters* 10.1 (2010), pp. 313–317. DOI: 10.1021/nl903592h (cited on page 16).

[122] Juan I. Climente, Jose L. Movilla, and Josep Planelles. "Auger recombination suppression in nanocrystals with asymmetric electron-hole confinement." In: *Small (Weinheim an der Bergstrasse, Germany)* 8.5 (2012), pp. 754–759. DOI: 10.1002/smll.201101740 (cited on page 16).

[123] Wan Ki Bae, Lazaro A. Padilha, Young-Shin Park, Hunter McDaniel, Istvan Robel, Jeffrey M. Pietryga, and Victor I. Klimov. "Controlled alloying of the core-shell interface in CdSe/CdS quantum dots for suppression of Auger recombination." In: *ACS nano* 7.4 (2013), pp. 3411–3419. DOI: 10.1021/nn4002825 (cited on page 16).

[124] Congjun Wang, Brian L. Wehrenberg, Chui Y. Woo, and Philippe Guyot-Sionnest. "Light Emission and Amplification in Charged CdSe Quantum Dots." In: *The Journal of Physical Chemistry B* 108.26 (2004), pp. 9027–9031. DOI: 10.1021/jp0489830 (cited on pages 16, 59, 71, 76).

[125] Jaco J. Geuchies, Baldur Brynjarsson, Gianluca Grimaldi, Solrun Gudjonsdottir, Ward van der Stam, Wiel H. Evers, and Arjan J. Houtepen. "Quantitative Electrochemical Control over Optical Gain in Quantum-Dot Solids." In: *ACS nano* 15.1 (2021), pp. 377–386. DOI: 10.1021/acsnano.0c07365 (cited on page 16).

[126] Victor I. Klimov, Sergei A. Ivanov, Jagjit Nanda, Marc Achermann, Ilya Bezel, John A. McGuire, and Andrei Piryatinski. "Single-exciton optical gain in semiconductor nanocrystals." In: *Nature* 447.7143 (2007), pp. 441–446. DOI: 10.1038/nature05839 (cited on pages 16, 59, 65, 71, 76).

[127] Dan Oron, Miri Kazes, and Uri Banin. "Multiexcitons in type-II colloidal semiconductor quantum dots." In: *Physical Review B* 75.3 (2007). DOI: 10.1103/PhysRevB.75.035330 (cited on page 16).

[128] Yuan Liu, Yuxuan Li, Kaimin Gao, Jingyi Zhu, and Kaifeng Wu. "Sub-Single-Exciton Optical Gain in Lead Halide Perovskite Quantum Dots Revealed by Exciton Polarization Spectroscopy." In: *Journal of the American Chemical Society* 145.47 (2023), pp. 25864–25873. DOI: 10.1021/jacs.3c10281 (cited on pages 17, 50, 55, 65, 67, 70, 74).

[129] Haipeng Lu, Gerard M. Carroll, Nathan R. Neale, and Matthew C. Beard. "Infrared Quantum Dots: Progress, Challenges, and Opportunities." In: *ACS nano* 13.2 (2019), pp. 939–953. DOI: 10.1021/acsnano.8b09815 (cited on page 17).

[130] Haipeng Lu, Zhiyuan Huang, Marissa S. Martinez, Justin C. Johnson, Joseph M. Luther, and Matthew C. Beard. "Transforming energy using quantum dots." In: *Energy & Environmental Science* 13.5 (2020), pp. 1347–1376. DOI: 10.1039/C9EE03930A (cited on page 17).

[131] P. Martyniuk and A. Rogalski. "Quantum-dot infrared photodetectors: Status and outlook." In: *Progress in Quantum Electronics* 32.3-4 (2008), pp. 89–120. DOI: 10.1016/j.pquantelec.2008.07.001 (cited on page 17).

[132] Jianbo Gao, Son C. Nguyen, Noah D. Bronstein, and A. Paul Alivisatos. "Solution-Processed, High-Speed, and High-Quantum-Efficiency Quantum Dot Infrared Photodetectors." In: *ACS Photonics* 3.7 (2016), pp. 1217–1222. DOI: 10.1021/acsphotonics.6b00211 (cited on page 17).

[133] D. V. Regelman, U. Mizrahi, D. Gershoni, E. Ehrenfreund, W. V. Schoenfeld, and P. M. Petroff. "Semiconductor quantum dot: a quantum light source of multicolor photons with tunable statistics." In: *Physical Review Letters* 87.25 (2001), p. 257401. DOI: 10.1103/PhysRevLett.87.257401 (cited on page 17).

[134] Andrew J. Shields. "Semiconductor quantum light sources." In: *Nature Photonics* 1.4 (2007), pp. 215–223. DOI: 10.1038/nphoton.2007.46 (cited on pages 17, 48).

[135] Laura M. Herz. "Charge-Carrier Dynamics in Organic-Inorganic Metal Halide Perovskites." In: *Annual review of physical chemistry* 67 (2016), pp. 65–89. DOI: 10.1146/annurev-physchem-040215-112222 (cited on page 18).

[136] Joseph S. Manser, Jeffrey A. Christians, and Prashant V. Kamat. "Intriguing Optoelectronic Properties of Metal Halide Perovskites." In: *Chemical reviews* 116.21 (2016), pp. 12956–13008. DOI: 10.1021/acs.chemrev.6b00136 (cited on page 18).

[137] Jun Kang and Lin-Wang Wang. "High Defect Tolerance in Lead Halide Perovskite CsPbBr3." In: *The journal of physical chemistry letters* 8.2 (2017), pp. 489–493. DOI: 10.1021/acs.jpclett.6b02800 (cited on page 18).

[138] He Huang, Maryna I. Bodnarchuk, Stephen V. Kershaw, Maksym V. Kovalenko, and Andrey L. Rogach. "Lead Halide Perovskite Nanocrystals in the Research Spotlight: Stability and Defect Tolerance." In: *ACS energy letters* 2.9 (2017), pp. 2071–2083. DOI: 10.1021/acsenergylett.7b00547 (cited on pages 18, 20, 59).

[139] Mujtaba Hussain, Muhammad Rashid, Faisal Saeed, and A. S. Bhatti. “Spin–orbit coupling effect on energy level splitting and band structure inversion in CsPbBr3.” In: *Journal of Materials Science* 56.1 (2021), pp. 528–542. DOI: 10.1007/s10853-020-05298-8 (cited on page 20).

[140] Corsin Battaglia, Andres Cuevas, and Stefaan de Wolf. “High-efficiency crystalline silicon solar cells: status and perspectives.” In: *Energy & Environmental Science* 9.5 (2016), pp. 1552–1576. DOI: 10.1039/c5ee03380b (cited on page 20).

[141] Niraj N. Lal, Yasmina Dkhissi, Wei Li, Qicheng Hou, Yi–Bing Cheng, and Udo Bach. “Perovskite Tandem Solar Cells.” In: *Advanced Energy Materials* 7.18 (2017). DOI: 10.1002/aenm.201602761 (cited on page 20).

[142] Hui Li and Wei Zhang. “Perovskite Tandem Solar Cells: From Fundamentals to Commercial Deployment.” In: *Chemical reviews* 120.18 (2020), pp. 9835–9950. DOI: 10.1021/acs.chemrev.9b00780 (cited on page 20).

[143] Renxing Lin, Jian Xu, Mingyang Wei, Yurui Wang, Zhengyuan Qin, Zhou Liu, Jinlong Wu, Ke Xiao, Bin Chen, So Min Park, Gang Chen, Harindi R. Atapattu, Kenneth R. Graham, Jun Xu, Jia Zhu, Ludong Li, Chunfeng Zhang, Edward H. Sargent, and Hairen Tan. “All-perovskite tandem solar cells with improved grain surface passivation.” In: *Nature* 603.7899 (2022), pp. 73–78. DOI: 10.1038/s41586-021-04372-8 (cited on page 20).

[144] Verena A. Hintermayr, Lakshminarayana Polavarapu, Alexander S. Urban, and Jochen Feldmann. “Accelerated Carrier Relaxation through Reduced Coulomb Screening in Two-Dimensional Halide Perovskite Nanoplatelets.” In: *ACS nano* 12.10 (2018), pp. 10151–10158. DOI: 10.1021/acsnano.8b05029 (cited on page 20).

[145] Bernhard J. Bohn, Thomas Simon, Moritz Gramlich, Alexander F. Richter, Lakshminarayana Polavarapu, Alexander S. Urban, and Jochen Feldmann. “Dephasing and Quantum Beating of Excitons in Methylammonium Lead Iodide Perovskite Nanoplatelets.” In: *ACS Photonics* 5.2 (2018), pp. 648–654. DOI: 10.1021/acsphotonics.7b01292 (cited on page 20).

[146] Bernhard J. Bohn, Yu Tong, Moritz Gramlich, May Ling Lai, Markus Döblinger, Kun Wang, Robert L. Z. Hoye, Peter Müller-Buschbaum, Samuel D. Stranks, Alexander S. Urban, Lakshminarayana Polavarapu, and Jochen Feldmann. “Boosting Tunable Blue Luminescence of Halide Perovskite Nanoplatelets through Postsynthetic Surface Trap Repair.” In: *Nano letters* 18.8 (2018), pp. 5231–5238. DOI: 10.1021/acs.nanolett.8b02190 (cited on pages 20, 21).

[147] Moritz Gramlich, Bernhard J. Bohn, Yu Tong, Lakshminarayana Polavarapu, Jochen Feldmann, and Alexander S. Urban. “Thickness-Dependence of Exciton-Exciton Annihilation in Halide Perovskite Nanoplatelets.” In: *The journal of physical chemistry letters* 11.13 (2020), pp. 5361–5366. DOI: 10.1021/acs.jpclett.0c01291 (cited on pages 20, 37).

[148] Qiao Zhang and Yadong Yin. “All-Inorganic Metal Halide Perovskite Nanocrystals: Opportunities and Challenges.” In: *ACS central science* 4.6 (2018), pp. 668–679. DOI: 10.1021/acscentsci.8b00201 (cited on page 20).

[149] Nadesh Fiuza-Maneiro, Kun Sun, Iago López-Fernández, Sergio Gómez-Graña, Peter Müller-Buschbaum, and Lakshminarayana Polavarapu. “Ligand Chemistry of Inorganic Lead Halide Perovskite Nanocrystals.” In: *ACS energy letters* 8.2 (2023), pp. 1152–1191. DOI: 10.1021/acsenergylett.2c02363 (cited on page 20).

[150] Gabriele Rainò, Nuri Yazdani, Simon C. Boehme, Manuel Kober-Czerny, Chenglian Zhu, Franziska Krieg, Marta D. Rossell, Rolf Erni, Vanessa Wood, Ivan Infante, and Maksym V. Kovalenko. “Ultra-narrow room-temperature emission from single CsPbBr3 perovskite quantum dots.” In: *Nature Communications* 13.1 (2022), p. 2587. DOI: 10.1038/s41467-022-30016-0 (cited on pages 20, 59).

[151] Navendu Mondal, Apurba De, and Anunay Samanta. “Achieving Near-Unity Photoluminescence Efficiency for Blue-Violet-Emitting Perovskite Nanocrystals.” In: *ACS energy letters* 4.1 (2019), pp. 32–39. DOI: 10.1021/acsenergylett.8b01909 (cited on page 21).

[152] A. I. Ekimov, I. A. Kudryavtsev, Al. L. Efros, T. V. Yazeva, F. Hache, M. C. Schanne-Klein, A. V. Rodina, D. Ricard, and C. Flytzanis. “Absorption and intensity-dependent photoluminescence measurements on CdSe quantum dots: assignment of the first electronic transitions.” In: *Journal of the Optical Society of America B* 10.1 (1993), p. 100. DOI: 10.1364/JOSAB.10.000100 (cited on pages 21, 43).

[153] D. J. Norris, A. Sacra, C. B. Murray, and M. G. Bawendi. “Measurement of the size dependent hole spectrum in CdSe quantum dots.” In: *Physical Review Letters* 72.16 (1994), pp. 2612–2615. doi: 10.1103/PhysRevLett.72.2612 (cited on pages 21, 43, 49).

[154] Gabriele Rainò, Georgian Nedelcu, Loredana Protesescu, Maryna I. Bodnarchuk, Maksym V. Kovalenko, Rainer F. Mahrt, and Thilo Stöferle. “Single Cesium Lead Halide Perovskite Nanocrystals at Low Temperature: Fast Single-Photon Emission, Reduced Blinking, and Exciton Fine Structure.” In: *ACS nano* 10.2 (2016), pp. 2485–2490. doi: 10.1021/acsnano.5b07328 (cited on pages 21, 43).

[155] Michael A. Becker, Roman Vaxenburg, Georgian Nedelcu, Peter C. Sercel, Andrew Shabaev, Michael J. Mehl, John G. Michopoulos, Samuel G. Lambrakos, Noam Bernstein, John L. Lyons, Thilo Stöferle, Rainer F. Mahrt, Maksym V. Kovalenko, David J. Norris, Gabriele Rainò, and Alexander L. Efros. “Bright triplet excitons in caesium lead halide perovskites.” In: *Nature* 553.7687 (2018), pp. 189–193. doi: 10.1038/nature25147 (cited on pages 21, 43).

[156] Michael A. Becker, Lorenzo Scarpelli, Georgian Nedelcu, Gabriele Rainò, Francesco Masia, Paola Borri, Thilo Stöferle, Maksym V. Kovalenko, Wolfgang Langbein, and Rainer F. Mahrt. “Long Exciton Dephasing Time and Coherent Phonon Coupling in CsPbBr2Cl Perovskite Nanocrystals.” In: *Nano letters* 18.12 (2018), pp. 7546–7551. doi: 10.1021/acs.nanolett.8b03027 (cited on pages 21, 43).

[157] Amrita Dey, Pravin Rathod, and Dinesh Kabra. “Role of Localized States in Photoluminescence Dynamics of High Optical Gain CsPbBr 3 Nanocrystals.” In: *Advanced Optical Materials* 6.11 (2018). doi: 10.1002/adom.201800109 (cited on pages 21, 43).

[158] Tushar Debnath, Debalaya Sarker, He Huang, Zhong-Kang Han, Amrita Dey, Lakshminarayana Polavarapu, Sergey V. Levchenko, and Jochen Feldmann. “Coherent vibrational dynamics reveals lattice anharmonicity in organic–inorganic halide perovskite nanocrystals.” In: *Nature Communications* 12.1 (2021). doi: 10.1038/s41467-021-22934-2 (cited on pages 21, 35, 43).

[159] Nikolay S. Makarov, Shaojun Guo, Oleksandr Isaienko, Wenyong Liu, István Robel, and Victor I. Klimov. “Spectral and Dynamical Properties of Single Excitons, Biexcitons, and Trions in Cesium-Lead-Halide Perovskite Quantum Dots.” In: *Nano letters* 16.4 (2016), pp. 2349–2362. doi: 10.1021/acs.nanolett.5b05077 (cited on pages 22, 54, 69).

[160] Sergii Yakunin, Loredana Protesescu, Franziska Krieg, Maryna I. Bodnarchuk, Georgian Nedelcu, Markus Humer, Gabriele de Luca, Manfred Fiebig, Wolfgang Heiss, and Maksym V. Kovalenko. “Low-threshold amplified spontaneous emission and lasing from colloidal nanocrystals of caesium lead halide perovskites.” In: *Nature Communications* 6 (2015), p. 8056. doi: 10.1038/ncomms9056 (cited on pages 22, 59, 61–64, 71, 75, 76).

[161] Yue Wang, Xiaoming Li, Jizhong Song, Lian Xiao, Haibo Zeng, and Handong Sun. “All-Inorganic Colloidal Perovskite Quantum Dots: A New Class of Lasing Materials with Favorable Characteristics.” In: *Advanced Materials* 27.44 (2015), pp. 7101–7108. doi: 10.1002/adma.201503573 (cited on pages 22, 59, 61, 64, 71, 75, 76).

[162] Cesare Soci, Giorgio Adamo, Daniele Cortecchia, Kaiyang Wang, Shumin Xiao, Qinghai Song, Anna Lena Schall-Giesecke, Piotr J. Cegielski, Max C. Lemme, Dario Gerace, Daniele Sanvitto, Jingyi Tian, Pavel A. Tonkaev, Sergey V. Makarov, Yuri S. Kivshar, Oscar A. Jimenez Gordillo, Andrea Melloni, Anatoly P. Pushkarev, Marianna D’Amato, Emmanuel Lhuillier, and Alberto Bramati. “(INVITED) Roadmap on perovskite nanophotonics.” In: *Optical Materials: X* 17 (2023), p. 100214. doi: 10.1016/j.omx.2022.100214 (cited on pages 22, 59).

[163] Wei Zhao, Zhengyuan Qin, Chunfeng Zhang, Guodong Wang, Xinyu Huang, Bin Li, Xingcan Dai, and Min Xiao. “Optical Gain from Biexcitons in CsPbBr3 Nanocrystals Revealed by Two-dimensional Electronic Spectroscopy.” In: *The journal of physical chemistry letters* 10.6 (2019), pp. 1251–1258. doi: 10.1021/acs.jpclett.9b00524 (cited on pages 22, 59, 61, 64, 75).

[164] Apurba De, Soumyadip Bhunia, Yichao Cai, Tal Binyamin, Lioz Etgar, and Sanford Ruhman. “Spectator Exciton Effects in Nanocrystals III: Unveiling the Stimulated Emission Cross Section in Quantum Confined CsPbBr3 Nanocrystals.” In: *Journal of the American Chemical Society* 146.29 (2024), pp. 20241–20250. doi: 10.1021/jacs.4c05412 (cited on pages 22, 59, 61, 64, 75).

[165] Juan Navarro-Arenas, Isaac Suárez, Vladimir S. Chirvony, Andrés F. Gualdrón-Reyes, Iván Mora-Seró, and Juan Martínez-Pastor. "Single-Exciton Amplified Spontaneous Emission in Thin Films of CsPbX3 (X = Br, I) Perovskite Nanocrystals." In: *The journal of physical chemistry letters* 10.20 (2019), pp. 6389–6398. DOI: 10.1021/acs.jpclett.9b02369 (cited on pages 22, 59, 61, 63, 64, 75).

[166] Stefania Milanese, Maria Luisa de Giorgi, Marco Anni, Maryna I. Bodnarchuk, and Luis Cerdán. "Rationalizing the Amplified Spontaneous Emission Mechanism in CsPbBr 3 Perovskite Nanocrystals Films by means of Optical Gain Measurements." In: *Advanced Optical Materials* 12.27 (2024). DOI: 10.1002/adom.202401078 (cited on pages 22, 59, 61–64, 75).

[167] Yi Wang, Min Zhi, Yu-Qiang Chang, Jian-Ping Zhang, and Yinthai Chan. "Stable, Ultralow Threshold Amplified Spontaneous Emission from CsPbBr3 Nanoparticles Exhibiting Trion Gain." In: *Nano letters* 18.8 (2018), pp. 4976–4984. DOI: 10.1021/acs.nanolett.8b01817 (cited on pages 22, 59, 61–64, 70, 75).

[168] K. L. Shaklee and R. F. Leheny. "DIRECT DETERMINATION OF OPTICAL GAIN IN SEMICONDUCTOR CRYSTALS." In: *Applied Physics Letters* 18.11 (1971), pp. 475–477. DOI: 10.1063/1.1653501 (cited on pages 22, 38, 41, 61, 62, 75).

[169] A. V. Malko, A. A. Mikhailovsky, M. A. Petruska, J. A. Hollingsworth, H. Htoon, M. G. Bawendi, and V. I. Klimov. "From amplified spontaneous emission to microring lasing using nanocrystal quantum dot solids." In: *Applied Physics Letters* 81.7 (2002), pp. 1303–1305. DOI: 10.1063/1.1497708 (cited on page 23).

[170] Quinten A. Akkerman. "Spheroidal Cesium Lead Chloride-Bromide Quantum Dots and a Fast Determination of Their Size and Halide Content." In: *Nano letters* 22.20 (2022), pp. 8168–8173. DOI: 10.1021/acs.nanolett.2c02601 (cited on page 27).

[171] Brent Fultz and James M. Howe. *Transmission Electron Microscopy and Diffractometry of Materials.* Berlin, Heidelberg: Springer Berlin Heidelberg, 2008. DOI: 10.1007/978-3-540-73886-2 (cited on page 27).

[172] Rayleigh. "XV. On the theory of optical images, with special reference to the microscope." In: *The London, Edinburgh, and Dublin Philosophical Magazine and Journal of Science* 42.255 (1896), pp. 167–195. DOI: 10.1080/14786449608620902 (cited on page 27).

[173] Nan Yao and Zhong Lin Wang. *Handbook of Microscopy for Nanotechnology.* Boston: Kluwer Academic Publishers, 2005. DOI: 10.1007/1-4020-8006-9 (cited on page 27).

[174] D. F. Swinehart. "The Beer-Lambert Law." In: *Journal of Chemical Education* 39.7 (1962), p. 333. DOI: 10.1021/ed039p333 (cited on page 28).

[175] Jonathan Mooney and Patanjali Kambhampati. "Get the Basics Right: Jacobian Conversion of Wavelength and Energy Scales for Quantitative Analysis of Emission Spectra." In: *The journal of physical chemistry letters* 4.19 (2013), pp. 3316–3318. DOI: 10.1021/jz401508t (cited on page 29).

[176] E. Marín and A. Calderón. "Conversion of Wavelength and Energy Scales and the Analysis of Optical Emission Spectra." In: *The journal of physical chemistry letters* 13.35 (2022), pp. 8376–8379. DOI: 10.1021/acs.jpclett.2c02621 (cited on page 29).

[177] Robert W. Boyd. *Nonlinear optics.* Fourth edition. London: Elsevier, AP Academic Press, 2020 (cited on pages 30–33).

[178] Donna Strickland and Gerard Mourou. "Compression of amplified chirped optical pulses." In: *Optics Communications* 55.6 (1985), pp. 447–449. DOI: 10.1016/0030-4018(85)90151-8 (cited on page 30).

[179] Jean-Claude Diels and Wolfgang Rudolph. *Ultrashort laser pulse phenomena: Fundamentals, techniques, and applications on a femtosecond time scale.* 2nd ed. Optics and photonics. Amsterdam and Boston: Elsevier / Academic Press, 2006 (cited on pages 30, 31).

[180] Bahaa E. A. Saleh and Malvin Carl Teich. *Fundamentals of Photonics.* 2nd edition. Wiley Series in Pure and Applied Optics. Chicester: John Wiley & Sons, 2013 (cited on page 32).

[181] C. Manzoni and G. Cerullo. "Design criteria for ultrafast optical parametric amplifiers." In: *Journal of Optics* 18.10 (2016), p. 103501. DOI: 10.1088/2040-8978/18/10/103501 (cited on page 33).

[182] Knox, Chemla, Miller, Stark, and Schmitt-Rink. "Femtosecond ac Stark effect in semiconductor quantum wells: Extreme low- and high-intensity limits." In: *Physical Review Letters* 62.10 (1989), pp. 1189–1192. DOI: 10.1103/PhysRevLett.62.1189 (cited on page 35).

[183] David Giovanni, Wee Kiang Chong, Yu Yang Fredrik Liu, Herlina Arianita Dewi, Tingting Yin, Yulia Lekina, Ze Xiang Shen, Nripan Mathews, Chee Kwan Gan, and Tze Chien Sum. “Coherent Spin and Quasiparticle Dynamics in Solution-Processed Layered 2D Lead Halide Perovskites.” In: *Advanced science (Weinheim, Baden-Wurttemberg, Germany)* 5.10 (2018), p. 1800664. DOI: 10.1002/advs.201800664 (cited on page 35).

[184] Sebastian Rieger, Tim Fürmann, Jacek K. Stolarczyk, and Jochen Feldmann. “Optically Induced Coherent Phonons in Bismuth Oxyiodide (BiOI) Nanoplatelets.” In: *Nano letters* 21.18 (2021), pp. 7887–7893. DOI: 10.1021/acs.nanolett.1c00530 (cited on page 35).

[185] Julian G. Mann, Fei He, Quinten A. Akkerman, Tushar Debnath, and Jochen Feldmann. “A Bound Exciton Resonance Modulated by Bulk and Localized Coherent Phonons in Double Perovskites.” In: *The journal of physical chemistry letters* 15.8 (2024), pp. 2169–2176. DOI: 10.1021/acs.jpclett.3c03443 (cited on page 35).

[186] Gabriel Nagamine, Tomas A. C. Ferreira, Diogo B. Almeida, Jonathan C. Lemus, Jun Hyuk Chang, Byeong Guk Jeong, Wan Ki Bae, and Lazaro A. Padilha. “Sample Concentration Affects Optical Gain Results in Colloidal Nanomaterials: Circumventing the Distortions by Below Band Gap Excitation.” In: *ACS Photonics* 9.1 (2022), pp. 156–162. DOI: 10.1021/acsphotonics.1c01293 (cited on page 37).

[187] Suzanne Bisschop, Pieter Geiregat, Tangi Aubert, and Zeger Hens. “The Impact of Core/Shell Sizes on the Optical Gain Characteristics of CdSe/CdS Quantum Dots.” In: *ACS nano* 12.9 (2018), pp. 9011–9021. DOI: 10.1021/acsnano.8b02493 (cited on page 37).

[188] Juan A. Castañeda, Gabriel Nagamine, Emre Yassitepe, Luiz G. Bonato, Oleksandr Voznyy, Sjoerd Hoogland, Ana F. Nogueira, Edward H. Sargent, Carlos H. Brito Cruz, and Lazaro A. Padilha. “Efficient Biexciton Interaction in Perovskite Quantum Dots Under Weak and Strong Confinement.” In: *ACS nano* 10.9 (2016), pp. 8603–8609. DOI: 10.1021/acsnano.6b03908 (cited on pages 38, 69).

[189] J. Aneesh, Abhishek Swarnkar, Vikash Kumar Ravi, Rituraj Sharma, Angshuman Nag, and K. V. Adarsh. “Ultrafast Exciton Dynamics in Colloidal CsPbBr 3 Perovskite Nanocrystals: Biexciton Effect and Auger Recombination.” In: *The Journal of Physical Chemistry C* 121.8 (2017), pp. 4734–4739. DOI: 10.1021/acs.jpcc.7b00762 (cited on page 38).

[190] Matthew N. Ashner, Katherine E. Shulenberger, Franziska Krieg, Eric R. Powers, Maksym V. Kovalenko, Moungi G. Bawendi, and William A. Tisdale. “Size-Dependent Biexciton Spectrum in CsPbBr 3 Perovskite Nanocrystals.” In: *ACS energy letters* 4.11 (2019), pp. 2639–2645. DOI: 10.1021/acsenergylett.9b02041 (cited on pages 38, 49).

[191] Jayanta Dana, Tal Binyamin, Lioz Etgar, and Sanford Ruhman. “Unusually Strong Biexciton Repulsion Detected in Quantum Confined CsPbBr3 Nanocrystals with Two and Three Pulse Femtosecond Spectroscopy.” In: *ACS nano* (2021). DOI: 10.1021/acsnano.1c02123 (cited on pages 38, 49).

[192] Samuel L. Sewall, Ryan R. Cooney, Kevin E. H. Anderson, Eva A. Dias, D. M. Sagar, and Patanjali Kambhampati. “State-resolved studies of biexcitons and surface trapping dynamics in semiconductor quantum dots.” In: *The Journal of chemical physics* 129.8 (2008), p. 084701. DOI: 10.1063/1.2971181 (cited on pages 43, 49, 51, 74).

[193] Anja Barfüßer, Sebastian Rieger, Amrita Dey, Ahmet Tosun, Quinten A. Akkerman, Tushar Debnath, and Jochen Feldmann. “Confined Excitons in Spherical-Like Halide Perovskite Quantum Dots.” In: *Nano letters* 22.22 (2022), pp. 8810–8817. DOI: 10.1021/acs.nanolett.2c02223 (cited on pages 43, 73).

[194] Zhiya Dang, Javad Shamsi, Francisco Palazon, Muhammad Imran, Quinten A. Akkerman, Sungwook Park, Giovanni Bertoni, Mirko Prato, Rosaria Brescia, and Liberato Manna. “In Situ Transmission Electron Microscopy Study of Electron Beam-Induced Transformations in Colloidal Cesium Lead Halide Perovskite Nanocrystals.” In: *ACS nano* 11.2 (2017), pp. 2124–2132. DOI: 10.1021/acsnano.6b08324 (cited on page 44).

[195] Justinas Butkus, Parth Vashishtha, Kai Chen, Joseph K. Gallaher, Shyamal K. K. Prasad, Dani Z. Metin, Geoffry Laufersky, Nicola Gaston, Jonathan E. Halpert, and Justin M. Hodgkiss. “The Evolution of Quantum Confinement in CsPbBr 3 Perovskite Nanocrystals.” In: *Chemistry of Materials* 29.8 (2017), pp. 3644–3652. DOI: 10.1021/acs.chemmater.7b00478 (cited on page 48).

[196] Wenbi Shcherbakov-Wu, Peter C. Sercel, Franziska Krieg, Maksym V. Kovalenko, and William A. Tisdale. “Temperature-Independent Dielectric Constant in CsPbBr3 Nanocrystals Revealed by Linear Absorption Spectroscopy.” In: *The journal of physical chemistry letters* 12.33 (2021), pp. 8088–8095. DOI: 10.1021/acs.jpclett.1c01822 (cited on page 49).

[197] Giovanni Mannino, Ioannis Deretzis, Emanuele Smecca, Antonino La Magna, Alessandra Alberti, Davide Ceratti, and David Cahen. “Temperature-Dependent Optical Band Gap in CsPbBr3, MAPbBr3, and FAPbBr3 Single Crystals.” In: *The journal of physical chemistry letters* 11.7 (2020), pp. 2490–2496. DOI: 10.1021/acs.jpclett.0c00295 (cited on page 49).

[198] Daniel Rossi, Hua Wang, Yitong Dong, Tian Qiao, Xiaofeng Qian, and Dong Hee Son. “Light-Induced Activation of Forbidden Exciton Transition in Strongly Confined Perovskite Quantum Dots.” In: *ACS nano* 12.12 (2018), pp. 12436–12443. DOI: 10.1021/acsnano.8b06649 (cited on page 49).

[199] Ajay K. Poonia, Megha Shrivastava, Wasim J. Mir, J. Aneesh, Angshuman Nag, and K. V. Adarsh. “Intervalley polaronic biexcitons in metal halide perovskite quantum dots.” In: *Physical Review B* 104.16 (2021). DOI: 10.1103/PhysRevB.104.L161407 (cited on pages 49, 50).

[200] Go Yumoto, Hirokazu Tahara, Tokuhisa Kawawaki, Masaki Saruyama, Ryota Sato, Toshiharu Teranishi, and Yoshihiko Kanemitsu. “Hot Biexciton Effect on Optical Gain in CsPbI3 Perovskite Nanocrystals.” In: *The journal of physical chemistry letters* 9.9 (2018), pp. 2222–2228. DOI: 10.1021/acs.jpclett.8b01029 (cited on page 49).

[201] Mikhail I. Dyakonov. *Spin Physics in Semiconductors*. Vol. 157. Cham: Springer International Publishing, 2017. DOI: 10.1007/978-3-319-65436-2 (cited on page 49).

[202] Xihan Chen, Haipeng Lu, Kang Wang, Yaxin Zhai, Vladimir Lunin, Peter C. Sercel, and Matthew C. Beard. “Tuning Spin-Polarized Lifetime in Two-Dimensional Metal-Halide Perovskite through Exciton Binding Energy.” In: *Journal of the American Chemical Society* 143.46 (2021), pp. 19438–19445. DOI: 10.1021/jacs.1c08514 (cited on pages 50, 55, 74).

[203] Samuel L. Sewall, Alberto Franceschetti, Ryan R. Cooney, Alex Zunger, and Patanjali Kambhampati. “Direct observation of the structure of band-edge biexcitons in colloidal semiconductor CdSe quantum dots.” In: *Physical Review B* 80.8 (2009). DOI: 10.1103/PhysRevB.80.081310 (cited on pages 51, 64, 74).

[204] Samuel L. Sewall, Ryan R. Cooney, Eva A. Dias, Pooja Tyagi, and Patanjali Kambhampati. “State-resolved observation in real time of the structural dynamics of multiexcitons in semiconductor nanocrystals.” In: *Physical Review B* 84.23 (2011). DOI: 10.1103/PhysRevB.84.235304 (cited on pages 51, 74).

[205] Cheng Zhang, Thanh Nhut Do, Xuanwei Ong, Yinthai Chan, and Howe-Siang Tan. “Understanding the features in the ultrafast transient absorption spectra of CdSe quantum dots.” In: *Chemical Physics* 481 (2016), pp. 157–164. DOI: 10.1016/j.chemphys.2016.08.027 (cited on pages 51, 55, 74).

[206] Eugene Hecht. *Optics*. 5 ed. Boston: Pearson Education Inc, 2017 (cited on page 54).

[207] Zhixing Gan, Weijian Chen, Lin Yuan, Guiyuan Cao, Chunhua Zhou, Shujuan Huang, Xiaoming Wen, and Baohua Jia. “External stokes shift of perovskite nanocrystals enlarged by photon recycling.” In: *Applied Physics Letters* 114.1 (2019). DOI: 10.1063/1.5081805 (cited on pages 54, 67).

[208] Michael C. Brennan, John E. Herr, Triet S. Nguyen-Beck, Jessica Zinna, Sergiu Draguta, Sergei Rouvimov, John Parkhill, and Masaru Kuno. “Origin of the Size-Dependent Stokes Shift in CsPbBr3 Perovskite Nanocrystals.” In: *Journal of the American Chemical Society* 139.35 (2017), pp. 12201–12208. DOI: 10.1021/jacs.7b05683 (cited on pages 54, 67).

[209] Yinsheng Guo, Omer Yaffe, Trevor D. Hull, Jonathan S. Owen, David R. Reichman, and Louis E. Brus. “Dynamic emission Stokes shift and liquid-like dielectric solvation of band edge carriers in lead-halide perovskites.” In: *Nature Communications* 10.1 (2019), p. 1175. DOI: 10.1038/s41467-019-09057-5 (cited on pages 54, 67).

[210] Zhuoming Zhang, Sushrut Ghonge, Yang Ding, Shubin Zhang, Mona Berciu, Richard D. Schaller, Boldizsár Jankó, and Masaru Kuno. “Resonant Multiple-Phonon Absorption Causes Efficient Anti-Stokes Photoluminescence in CsPbBr3 Nanocrystals.” In: *ACS nano* 18.8 (2024), pp. 6438–6444. DOI: 10.1021/acsnano.3c11908 (cited on pages 54, 60, 67).

[211] Simone Strohmair, Amrita Dey, Yu Tong, Lakshminarayana Polavarapu, Bernhard J. Bohn, and Jochen Feldmann. “Spin Polarization Dynamics of Free Charge Carriers in CsPbI3 Nanocrystals.” In: *Nano letters* 20.7 (2020), pp. 4724–4730. DOI: 10.1021/acs.nanolett.9b05325 (cited on page 56).

[212] Nima Taghipour, Mariona Dalmases, Guy L. Whitworth, Miguel Dosil, Andreas Othonos, Sotirios Christodoulou, Shanti Maria Liga, and Gerasimos Konstantatos. “Colloidal Quantum Dot Infrared Lasers Featuring Sub-Single-Exciton Threshold and Very High Gain.” In: *Advanced Materials* 35.1 (2023), e2207678. DOI: 10.1002/adma.202207678 (cited on pages 59, 63, 71, 76).

[213] Anja Barfüßer, Jochen Feldmann, and Quinten A. Akkerman. “Biexcitonic Optical Gain in CsPbBr 3 Quantum Dots.” In: *ACS Photonics* (2024). DOI: 10.1021/acsphotonics.4c01659 (cited on pages 60, 73).

[214] Yulu Li, Xiao Luo, Tao Ding, Xin Lu, and Kaifeng Wu. “Size– and Halide–Dependent Auger Recombination in Lead Halide Perovskite Nanocrystals.” In: *Angewandte Chemie* 132.34 (2020), pp. 14398–14401. DOI: 10.1002/ange.202004668 (cited on pages 60, 69, 71).

[215] Yu Tong, Eva Bladt, Meltem F. Aygüler, Aurora Manzi, Karolina Z. Milowska, Verena A. Hintermayr, Pablo Docampo, Sara Bals, Alexander S. Urban, Lakshminarayana Polavarapu, and Jochen Feldmann. “Highly Luminescent Cesium Lead Halide Perovskite Nanocrystals with Tunable Composition and Thickness by Ultrasonication.” In: *Angewandte Chemie (International ed. in English)* 55.44 (2016), pp. 13887–13892. DOI: 10.1002/anie.201605909 (cited on pages 62, 63).

[216] Franziska Krieg, Stefan T. Ochsenbein, Sergii Yakunin, Stephanie ten Brinck, Philipp Aellen, Adrian Süess, Baptiste Clerc, Dominic Guggisberg, Olga Nazarenko, Yevhen Shynkarenko, Sudhir Kumar, Chih-Jen Shih, Ivan Infante, and Maksym V. Kovalenko. “Colloidal CsPbX3 (X = Cl, Br, I) Nanocrystals 2.0: Zwitterionic Capping Ligands for Improved Durability and Stability.” In: *ACS energy letters* 3.3 (2018), pp. 641–646. DOI: 10.1021/acsenergylett.8b00035 (cited on pages 62, 63, 71).

[217] Muhammad Imran, Vincenzo Caligiuri, Mengjiao Wang, Luca Goldoni, Mirko Prato, Roman Krahne, Luca de Trizio, and Liberato Manna. “Benzoyl Halides as Alternative Precursors for the Colloidal Synthesis of Lead-Based Halide Perovskite Nanocrystals.” In: *Journal of the American Chemical Society* 140.7 (2018), pp. 2656–2664. DOI: 10.1021/jacs.7b13477 (cited on pages 62, 63).

[218] Burak Guzelturk, Matthew Pelton, Murat Olutas, and Hilmi Volkan Demir. “Giant Modal Gain Coefficients in Colloidal II-VI Nanoplatelets.” In: *Nano letters* 19.1 (2019), pp. 277–282. DOI: 10.1021/acs.nanolett.8b03891 (cited on page 63).

[219] Saif M. H. Qaid, Hamid M. Ghaithan, Khulod K. AlHarbi, Bandar Ali Al-Asbahi, and Abdullah S. Aldwayyan. “Enhancement of Light Amplification of CsPbBr3 Perovskite Quantum Dot Films via Surface Encapsulation by PMMA Polymer.” In: *Polymers* 13.15 (2021), p. 2574. DOI: 10.3390/polym13152574 (cited on pages 63, 71).

[220] Changsoon Cho, Alexander Palatnik, Markas Sudzius, Raphael Grodofzig, Frederik Nehm, and Karl Leo. “Controlling and Optimizing Amplified Spontaneous Emission in Perovskites.” In: *ACS applied materials & interfaces* 12.31 (2020), pp. 35242–35249. DOI: 10.1021/acsami.0c08870 (cited on page 63).

[221] Michael C. Brennan, Jessica Zinna, and Masaru Kuno. “Existence of a Size-Dependent Stokes Shift in CsPbBr 3 Perovskite Nanocrystals.” In: *ACS energy letters* 2.7 (2017), pp. 1487–1488. DOI: 10.1021/acsenergylett.7b00383 (cited on page 67).

[222] Pieter Geiregat, Onur Erdem, Margarita Samoli, Kai Chen, Justin M. Hodgkiss, and Zeger Hens. “The Impact of Partial Carrier Confinement on Stimulated Emission in Strongly Confined Perovskite Nanocrystals.” In: *ACS nano* 18.27 (2024), pp. 17794–17805. DOI: 10.1021/acsnano.4c03441 (cited on page 67).

[223] Ilka Vinçon, Anja Barfüßer, Jochen Feldmann, and Quinten A. Akkerman. “Quantum Dot Metal Salt Interactions Unraveled by the Sphere of Action Model.” In: *Journal of the American Chemical Society* 145.26 (2023), pp. 14395–14403. DOI: 10.1021/jacs.3c03582 (cited on pages 69, 74).

[224] Naoki Yarita, Hirokazu Tahara, Toshiyuki Ihara, Tokuhisa Kawawaki, Ryota Sato, Masaki Saruyama, Toshiharu Teranishi, and Yoshihiko Kanemitsu. “Dynamics of Charged Excitons and Biexcitons in CsPbBr3 Perovskite Nanocrystals Revealed by Femtosecond Transient-Absorption and Single-Dot Luminescence Spectroscopy.” In: *The journal of physical chemistry letters* 8.7 (2017), pp. 1413–1418. DOI: 10.1021/acs.jpclett.7b00326 (cited on page 70).

[225] Yoshihiko Kanemitsu. “Trion dynamics in lead halide perovskite nanocrystals.” In: *The Journal of chemical physics* 151.17 (2019), p. 170902. DOI: 10.1063/1.5125628 (cited on page 70).

[226] Kenichi Cho, Takao Sato, Takumi Yamada, Ryota Sato, Masaki Saruyama, Toshiharu Teranishi, Hidekatsu Suzuura, and Yoshihiko Kanemitsu. “Size Dependence of Trion and Biexciton Binding Energies in Lead Halide Perovskite Nanocrystals.” In: *ACS nano* 18.7 (2024), pp. 5723–5729. DOI: 10.1021/acsnano.3c11842 (cited on page 70).

[227] Chenglian Zhu, Tan Nguyen, Simon C. Boehme, Anastasiia Moskalenko, Dmitry N. Dirin, Maryna I. Bodnarchuk, Claudine Katan, Jacky Even, Gabriele Rainò, and Maksym V. Kovalenko. “Many-Body Correlations and Exciton Complexes in CsPbBr3 Quantum Dots.” In: *Advanced Materials* 35.9 (2023), e2208354. DOI: 10.1002/adma.202208354 (cited on page 70).

[228] Maria Luisa de Giorgi, Franziska Krieg, Maksym V. Kovalenko, and Marco Anni. “Amplified Spontaneous Emission Threshold Reduction and Operational Stability Improvement in CsPbBr3 Nanocrystals Films by Hydrophobic Functionalization of the Substrate.” In: *Scientific reports* 9.1 (2019), p. 17964. DOI: 10.1038/s41598-019-54412-7 (cited on page 71).

[229] Zhiping Hu, Zhengzheng Liu, Yao Bian, Shiqi Li, Xiaosheng Tang, Juan Du, Zhigang Zang, Miao Zhou, Wei Hu, Yuxi Tian, and Yuxin Leng. “Enhanced Two–Photon–Pumped Emission from In Situ Synthesized Nonblinking CsPbBr 3 /SiO 2 Nanocrystals with Excellent Stability.” In: *Advanced Optical Materials* 6.3 (2018). DOI: 10.1002/adom.201700997 (cited on page 71).

[230] Yulu Li, Tao Ding, Xiao Luo, Zongwei Chen, Xue Liu, Xin Lu, and Kaifeng Wu. “Biexciton Auger recombination in mono-dispersed, quantum-confined CsPbBr3 perovskite nanocrystals obeys universal volume-scaling.” In: *Nano Research* 12.3 (2019), pp. 619–623. DOI: 10.1007/s12274-018-2266-7 (cited on page 71).

[231] Evan H. Oriel, Dmitry N. Dirin, Kseniia Shcherbak, Maryna I. Bodnarchuk, Maksym V. Kovalenko, Lin X. Chen, and Richard D. Schaller. “Intraband Cooling and Auger Recombination in Weakly to Strongly Quantum-Confined CsPbBr3 Perovskite Nanocrystals.” In: *The journal of physical chemistry letters* 15.23 (2024), pp. 6062–6068. DOI: 10.1021/acs.jpclett.4c00941 (cited on page 71).

[232] Pieter Geiregat, Jorick Maes, Kai Chen, Emile Drijvers, Jonathan de Roo, Justin M. Hodgkiss, and Zeger Hens. “Using Bulk-like Nanocrystals To Probe Intrinsic Optical Gain Characteristics of Inorganic Lead Halide Perovskites.” In: *ACS nano* 12.10 (2018), pp. 10178–10188. DOI: 10.1021/acsnano.8b05092 (cited on page 71).

[233] Chun Hao Lin, Qingji Zeng, Evan Lafalce, Shengtao Yu, Marcus J. Smith, Young Jun Yoon, Yajing Chang, Yang Jiang, Zhiqun Lin, Zeev Valy Vardeny, and Vladimir V. Tsukruk. “Large–Area Lasing and Multicolor Perovskite Quantum Dot Patterns.” In: *Advanced Optical Materials* 6.16 (2018). DOI: 10.1002/adom.201800474 (cited on pages 71, 76).

[234] Siqi Li, Dangyuan Lei, Wei Ren, Xuyun Guo, Shengfan Wu, Ye Zhu, Andrey L. Rogach, Manish Chhowalla, and Alex K-Y Jen. “Water-resistant perovskite nanodots enable robust two-photon lasing in aqueous environment.” In: *Nature Communications* 11.1 (2020), p. 1192. DOI: 10.1038/s41467-020-15016-2 (cited on pages 71, 76).

[235] Yue Wang, Xiaoming Li, Venkatram Nalla, Haibo Zeng, and Handong Sun. “Solution–Processed Low Threshold Vertical Cavity Surface Emitting Lasers from All–Inorganic Perovskite Nanocrystals.” In: *Advanced Functional Materials* 27.13 (2017). DOI: 10.1002/adfm.201605088 (cited on pages 71, 76).

[236] Chun-Ying Huang, Chen Zou, Chenyi Mao, Kathryn L. Corp, Yung-Chi Yao, Ya-Ju Lee, Cody W. Schlenker, Alex K. Y. Jen, and Lih Y. Lin. “CsPbBr 3 Perovskite Quantum Dot Vertical Cavity Lasers with Low Threshold and High Stability.” In: *ACS Photonics* 4.9 (2017), pp. 2281–2289. DOI: 10.1021/acsphotonics.7b00520 (cited on pages 71, 76).

[237] Hongbo Zhang, Wen Wen, Bowen Du, Lei Zhou, Yu Chen, Shun Feng, Chenji Zou, Lishu Wu, Hong Jin Fan, Weibo Gao, Handong Sun, Jingzhi Shang, and Ting Yu. “Stable continuous-wave lasing from discrete cesium lead bromide quantum dots embedded in a microcavity.” In: *Nanoscale horizons* 8.10 (2023), pp. 1403–1410. DOI: 10.1039/D3NH00139C (cited on pages 71, 76).

[238] Patrick von Schwerin, Markus Döblinger, Tushar Debnath, Jochen Feldmann, and Quinten A. Akkerman. “Size-Tunable Manganese-Doped Spheroidal CsPbCl3 Quantum Dots.” In: *The journal of physical chemistry letters* 15.14 (2024), pp. 3728–3732. DOI: 10.1021/acs.jpclett.4c00049 (cited on page 74).

[239] Mariam Kurashvili, Jordi Llusar, Lena S. Stickel, Tim Würthner, David Ederle, Ivan Infante, Jochen Feldmann, and Quinten A. Akkerman. “Efficient Energy Transfer from Quantum Dots to Closely-Bound Dye Molecules without Spectral Overlap.” In: *Angewandte Chemie International Edition* (2024), e202420658. DOI: 10.1002/anie.202420658 (cited on page 74).

[240] Joo Sung Kim, Jung-Min Heo, Gyeong-Su Park, Seung-Je Woo, Changsoon Cho, Hyung Joong Yun, Dong-Hyeok Kim, Jinwoo Park, Seung-Chul Lee, Sang-Hwan Park, Eojin Yoon, Neil C. Greenham, and Tae-Woo Lee. “Ultra-bright, efficient and stable perovskite light-emitting diodes.” In: *Nature* 611.7937 (2022), pp. 688–694. DOI: 10.1038/s41586-022-05304-w (cited on page 74).

[241] He Dong, Chenxin Ran, Weiyin Gao, Mingjie Li, Yingdong Xia, and Wei Huang. “Metal Halide Perovskite for next-generation optoelectronics: progresses and prospects.” In: *eLight* 3.1 (2023). DOI: 10.1186/s43593-022-00033-z (cited on page 74).

[242] Qingsong Shan, Yuhui Dong, Hengyang Xiang, Danni Yan, Tianjun Hu, Beichen Yuan, Hong Zhu, Yifei Wang, and Haibo Zeng. “Perovskite Quantum Dots for the Next–Generation Displays: Progress and Prospect.” In: *Advanced Functional Materials* 34.36 (2024). DOI: 10.1002/adfm.202401284 (cited on page 74).

[243] Hongjin Li, Yifeng Feng, Meiyi Zhu, Yun Gao, Chao Fan, Qiaopeng Cui, Qiuting Cai, Ke Yang, Haiping He, Xingliang Dai, Jingyun Huang, and Zhizhen Ye. “Nanosurface-reconstructed perovskite for highly efficient and stable active-matrix light-emitting diode display.” In: *Nature nanotechnology* 19.5 (2024), pp. 638–645. DOI: 10.1038/s41565-024-01652-y (cited on page 74).

[244] Shuai Yuan, Linjie Dai, Yuqi Sun, Florian Auras, Yu-Hang Zhou, Rui-Zhi An, Yun Liu, Chenfeng Ding, Cathal Cassidy, Xun Tang, Shou-Cheng Dong, Hyung-Been Kang, Kai Chen, Xiaomin Liu, Zhi-Feng Ye, Yixin Zhao, Chihaya Adachi, Liang-Sheng Liao, Neil C. Greenham, Yabing Qi, Samuel D. Stranks, Lin-Song Cui, and Richard H. Friend. “Efficient blue electroluminescence from reduced-dimensional perovskites.” In: *Nature Photonics* 18.5 (2024), pp. 425–431. DOI: 10.1038/s41566-024-01382-6 (cited on page 74).

Appendix

Chemicals

Lead(II) bromide ($PbBr_2$, 99.999 %), cesium carbonate (Cs_2CO_3, 99.9 %), trioctylphosphine oxide (TOPO, 99 %), hexane (≥99 %), n-octane (min. 99 %), diisooctylphosphinic acid (DOPA, 90 %), toluene (99.5 %), ethanol (99.8 %), aceton (≥99.5 %), didodecyldimethylammonium bromide (DDAB, 98 %), acetonitrile (≥99.9 %), and chloroform ($CHCl_3$, 99.5 %) were purchased from *Merck*. Lecithin (>97 % from soy) was purchased from *Carl Roth*. All chemicals were used without further purification.

Stock Solutions

Stock solutions were prepared as reported in Reference 54.

- The $PbBr_2$ stock solution (0.04 M) was prepared by dissolving 1 mmol of $PbBr_2$ and 5 mmol of TOPO in 5 ml of octane at 120 °C in a 40 ml vial. When all the $PbBr_2$ was dissolved, the vial was cooled to room temperature and 20 ml of hexane was added.
- The Cs-DOPA stock solution (0.02 M) was prepared by transferring 100 mg of Cs_2CO_3 together with 1 ml of DOPA and 2 ml of octane at 120 °C into a 40 ml vial. When all the Cs_2CO_3 was dissolved, the stock solution was cooled to room temperature and 27 ml hexane was added.
- The lecithin stock solution (~0.13 M) was prepared by dissolving 0.5 g of lecithin in 10 ml of hexane.
- The TOPO stock solution (0.2 M) was prepared by dissolving 4 mmol of TOPO in 20 ml of hexane.
- The DDAB stock solution (0.1 M) was prepared by dissolving 1 mmol of DDAB in 10 ml of $CHCl_3$.

Synthesis

The synthesis is based on the room temperature synthesis method reported in Reference 54.

- Synthesis of the $CsPbBr_3$ QDs with lecithin as ligands and a diameter of ~6.8 nm:
  5 ml of hexane, 500 µl of $PbBr_2$, and 250 µl of TOPO stock solution were transferred into an 8 ml vial. Under vigorous stirring, 250 µl of Cs-DOPA stock solution was injected. The reaction was left stirring for ~5 min, after which 250 µl of lecithin solution was added. After 1 min, a four-fold excess of aceton was added, and the QDs were centrifuged at 6000 rpm for 2 min. The supernatant was discarded and the QDs redispersed in 1 ml of toluene and precipitated with 1 ml of ethanol. Finally, the QDs were centrifuged at 6000 rpm for 2 min, the supernatant discarded, and the QDs redispersed in hexane.

- Synthesis of the $CsPbBr_3$ QDs with DDAB as ligands and a diameter of ~6 nm: 2 ml of hexane and 1 ml of $PbBr_2$ stock solution were transferred into an 20 ml vial. Under vigorous stirring, 500 µl of Cs-DOPA stock solution was injected. The reaction was left stirring for ~5 min, after which 2 ml of $CHCl_3$ was added followed by 500 µl of DDAB solution. After 1 min, 5 ml acetonitrile was added and the QDs were centrifuged at 6000 rpm for 2 min. The supernatant was discarded and the QDs redispersed in 1 ml of octane.

Gaussian Fitting of Absorption Spectra

Figure A.1 shows the absorption spectrum of a $CsPbBr_3$ QD ensemble studied in Chapter 4. Fitting of Gaussian peaks reproduces the absorption spectrum almost perfectly. The Gaussian fit to the first absorption resonance X1 is marked as $OD_{\text{X1}}(E)$.

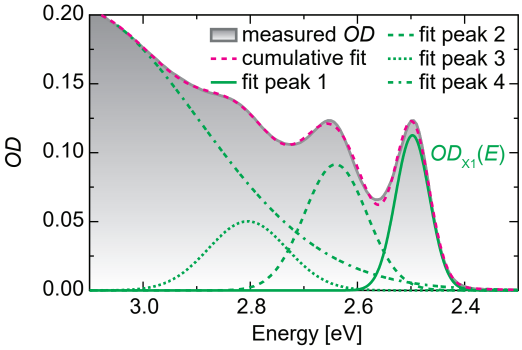

Figure A.1: Absorption Spectrum Gaussian Fitting. Fitting four Gaussian peaks to the steady-state absorption spectrum of $CsPbBr_3$ QDs with an diameter of ~6.8 nm. $OD_{\text{X1}}(E)$ as the absorption associated with X1 is indicated.

Figure A.2 shows the absorption spectrum of a $CsPbBr_3$ QD ensemble studied in Chapter 5. Fitting of Gaussian peaks reproduces the absorption spectrum almost perfectly. From the Gaussian fit to the first absorption resonance X1 the FWHM of ~81 meV is extracted.

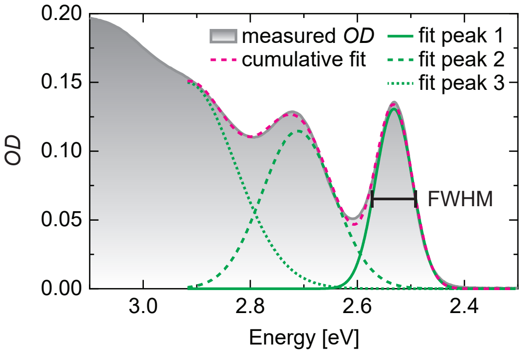

Figure A.2: Extracting FWHM via Gaussian Fitting. Fitting three Gaussian peaks to the steady-state absorption spectrum of $CsPbBr_3$ QDs with an diameter of ~6 nm. The extracted FWHM of ~81 meV of the absorption associated with X1 is indicated.

List of Figures

2.1 Quantum Confinement Regimes 6
2.2 Weak Confinement Model 8
2.3 Strong Confinement Model 8
2.4 Multi-Particle States 10
2.5 Core/Shell Quantum Dots 11
2.6 Auger Recombination and Exciton-Exciton Annihilation 12
2.7 Optical Gain in Different Systems 14
2.8 Type-II Core/Shell Quantum Dot 17
2.9 Perovskite Unit Cell and Crystal Structure 18
2.10 Electronic Band Formation 19
2.11 Inverted Band Structure of Perovskites 19
2.12 Principle of Amplified Spontaneous Emission 23

3.1 Amplifier System 30
3.2 Nonlinear Processes 31
3.3 Transient Absorption Spectroscopy Principle 34
3.4 Transient Absorption Setup 35
3.5 Average Quantum Dot Excitation 38
3.6 Amplified Spontaneous Emission Setup 39
3.7 Analysis of Laser Spot Profile 40
3.8 Variable Stripe Length Method 41

4.1 HAADF-STEM Images 44
4.2 Steady-State Optical Properties of $CsPbBr_3$ NCs 45
4.3 Weak and Strong Confinement Models 46
4.4 Transient Absorption Measurements 48
4.5 Polarization-Selective X1X1 Biexciton Formation 50
4.6 Biexciton Binding Energy Determination 51
4.7 Modeling of Excited State Absorption and Transient Absorption Spectra . . 52
4.8 Contribution of Polarization and Stimulated Emission to the Modeling . . . 55
4.9 Comprehensive Interpretation of Transient Absorption Spectrum 56
4.10 Transient Absorption Dynamics 57
4.11 Size and Composition Dependent Absorption and Transient Absorption Spectra 58

5.1 Steady-State Spectra 60
5.2 Amplified Spontaneous Emission Measurement 61
5.3 Amplified Spontaneous Emission Threshold Determination 62
5.4 Net Optical Gain Coefficient Determination 63
5.5 Optical Gain in the Excited State 64
5.6 Optical Gain Threshold Determination 65
5.7 Biexciton Binding Energy Promoting Optical Gain 66
5.8 Spectral Position of Optical Gain and Stokes Shift 67
5.9 Optical Gain Dynamics 68
5.10 Biexciton Dynamics 68
5.11 Comparison of Gain Duration and Biexciton Lifetime 70

A.1 Absorption Spectrum Gaussian Fitting XX
A.2 Extracting FWHM via Gaussian Fitting XX

List of Tables

4.1 Material Specific Parameters for $CsPbBr_3$ 47
5.1 Exponential Fitting Time Constants 69

List of Abbreviations

ASE amplified spontaneous emission

BBO barium borate

CB conduction band

CCD charge-coupled device

CPA chirped-pulse amplification

DDAB didodecyldimethylammonium bromide

DFG difference-frequency generation

DOPA diisooctylphosphonic acid

FF front-face

FWHM full width at half maximum

HAADF high-angle annular dark-field

HAADF-STEM high-angle annular dark-field scanning transmission electron microscopy

he heavy electron

hh heavy hole

le light electron

LED light emitting diode

lh light hole

LHP lead halide perovskite

NC nanocrystal

ND neutral density

NPL nanoplatelet

OPA optical parametric amplifier

PL photoluminescence

PLQY photoluminescence quantum yield

QD quantum dot

RA right-angle

SFG sum-frequency generation

SHG second-harmonic generation

STEM scanning transmission electron microscopy

TA transient absorption

TOPO trioctylphosphineoxide

UV ultraviolet

VB valence band

VSL variable stripe length

Acknowledgments

First of all, I would like to thank Prof. Jochen Feldmann for supervising me during my PhD in his group. I am especially grateful for the constructive scientific discussions and for sharing your knowledge about physics. Your guidance has taught me to always come back to fundamental physics and to convey concepts clearly and concisely. I greatly appreciate the opportunities I had to present my work at several international conferences and to meet many scientists during seminars and talks, which has been an invaluable experience.

Next, I want to thank Quinten Akkerman for your guidance in the past years. Thank you for always being available for discussions and whenever I needed your input and advice. Bringing Luna around has always made me happy! In addition, thank you for providing such high-quality and interesting samples that have kept me busy in the last few years.

Besides the scientific part, there is always a lot of administrative and organizational work to do. Thank you, Gerlinde Adam, for all your help in administrative matters and for always putting a smile on my face! I also want to thank Theobald Lohmüller for organizing all the teaching; I had a lot of fun giving tutorials. Thank you also to Talee Barghouti and Stefan Niedermaier for your technical support in the chemistry and optical labs.

To everyone who has shared an office with me, Philipp Bootz, Ilka Vinçon, Jinhua Zhang, Stefanie Pritzl, Huayang Zhang, and Kushagra Gahlot, thank you for the great atmosphere. It was always a great joy to be in the office with you!

Furthermore, I want to thank all my colleagues in the last years for the great scientific and non-scientific discussions, the entertaining lunch and coffee breaks, and all the laughs we shared. I especially want to thank Mariam Kurashvili, Fei He, Dominik Kammerer, Paul Vosshage, Lena Stickel, Matthias Kestler, Julian Mann, Sushant Ghimire, David Ederle, Sebastian Rieger, Nicola Bohn, Jiawen Fang, Ahmet Tosun, Amrita Dey, and Tushar Debnath. The mutual support and encouragement we shared during this time meant a lot to me.

Finally, thank you to my family and everyone who supported me during my PhD in any way. My deepest gratitude goes to Andreas Aigner for your constant support and motivation. Thank you for going through this PhD journey together!